Title

Aerodynamic, Moving-Mesh Modeling of Parachute Pendulum Motion: Development and Validation of a CFD Methodology

Author

Halstrom, Logan

Publication Date

2021

Aerodynamic, Moving-Mesh Modeling of Parachute Pendulum Motion: Development and Validation of a CFD Methodology

By

LOGAN D. HALSTROM

DISSERTATION

Submitted in partial satisfaction of the requirements for the degree of

DOCTOR OF PHILOSOPHY

in

Mechanical and Aerospace Engineering

in the

OFFICE OF GRADUATE STUDIES

of the

UNIVERSITY OF CALIFORNIA

DAVIS

Approved:

Stephen K. Robinson, Chair

Jean-Pierre Delplanque

Mohamed M. Hafez

Committee in Charge

2021

CONTENTS

List of Figures

List of Tables

Abstract

Aerodynamic, Moving-Mesh Modeling of Parachute Pendulum Motion: Development and Validation of a CFD Methodology

Parachutes are an essential design component of every crewed space vehicle currently in development. Some high-drag parachute designs have the potential to be inherently unstable and undergo pendulum motion in flight, subjecting the crew and cargo to additional hazards during landing. A fundamental understanding of the coupled dynamics and aerodynamics of parachutes is essential in order to design these descent systems safely. Traditionally, parachute design is accomplished through extensive flight and wind tunnel testing, but Computational Fluid Dynamics (CFD) modeling is an advancing tool that has the ability to provide additional insight into this analysis process. State-of-the-art computational techniques like Fluid-structure Interaction (FSI) provide the highest fidelity approximations of parachute flows but do not yet have the same level of confidence in the industry as rigid-body, Reynolds-averaged Navier-Stokes (RANS) CFD. This work applies the reliability and accuracy of structured, overset mesh CFD techniques to the parachute design process by simplifying the simulated parachute as a rigid, nonporous canopy. Validation of the acceptability of these simplifications is achieved through experimental comparison.

The CFD solver OVERFLOW's built-in Geometry Manipulation Protocol (GMP) tool couples the discrete solution of the Navier-Stokes equations with explicit solution of 6-degree-of-freedom (DoF) dynamics equations, enabling relative motion of overset grids driven by integrated aerodynamic loads. This research details a method for utilizing this capability to simulate dynamic pendulum motion of a parachute, driven by the aerodynamics of the massively-separated, bluff-body wake. Validation of the functionality of GMP in modeling constrained, aerodynamically-driven, pendulum motion was established by simulating a 1-DoF, circular cylinder pendulum and comparing the resulting motion predictions to a analogous numerical model derived by assuming a constant drag coefficient (C_d) for the cylinder. A simple parachute-analog geometry was also simulated in two and three dimensions to demonstrate the model's ability to predict multiple modes of motion driven by unsteady aerodynamics. Accuracies for the parachute pendulum CFD model were established by simulating a high-fidelity, rigid-shell model of the Orion Multi-Purpose Crew Vehicle (MPCV) main parachute, prescribed to move according to a fit equation of the motion observed in a 35 %-scale wind tunnel test of the same geometry. Similar magnitude and trends of the unsteady aerodynamic loads were confirmed and CFD model uncertainties were established by comparing relative differences. Finally, a parametric study of the effects of geometric porosity on dynamic stability was performed for the two-dimensional, simple parachute-analog geometry to demonstrate the ability of the model to predict dynamic stability characteristics of new designs.

ACKNOWLEDGMENTS

This work was made possible by building from the strong foundation of previous research in this field of study and also by the professional and personal support of my colleagues, friends, and family. Thank you to Professor Robinson for guiding and informing both this research and my own career development as a graduate student and an aerospace engineer. Thank you to my Committee members, Professors Delplanque and Hafez, for refining and enhancing the focus and scope of this thesis. Thank you to John Karasinski and Alex Beckerman for your persistence in supporting and advancing this research throughout its many, minute iterations. Thank you to the members of the Human/Vehicle/Robotic Integration and Performance lab for your support, encouragement, and comradery throughout my graduate experience. Thank you to my leadership and colleagues at NASA's Johnson Space Center and Ames Research Center for inspiring this research, supplying the resources required to learn about, develop, and run the CFD simulations that comprise this work, and willingly and readily sharing a collective expertise and creating an environment of excellence that has allowed me to improve and excel as an aerospace engineer.

Thank you to the NASA Advanced Supercomputing Division and JSC Flight Science Lab for providing the computational resources required to complete this work. Thank you to the Capsule Parachute Assembly System, National Full-scale Aerodynamics Complex, and other testing teams for creating and publishing extensive, high-quality experimental data sets for the Orion parachute system. Thank you to the Joseph L. Steger Fellowship for financial support of my graduate education. Thank you to the UC Davis Campus Departments for providing financial support to myself and my family after our losses in the 2018 Camp Fire that devastated the Town of Paradise and surrounding areas in Butte County. Your support helped alleviate the pain of loss and stress of decision-making in the immediate aftermath of this traumatic event.

And, from the bottom of my heart, thank you to my family. Thank you to my Mother, Carol Halstrom, and Brother, Grant Halstrom, for your unconditional love and dedication across this long journey. Thank you to my Father, Lee Halstrom, who always encouraged me, and, I know, would be very proud. Finally, thank you to my fiance, Elena Kolarov, for being my daily inspiration, for your unquestioning understanding of this undertaking, and for your unwavering love.

Chapter 1

Introduction

1.1 Motivation

The parachute, a fabric canopy filled with air and acting as a decelerator, is an ancient concept, with versions dating back to Leonardo da Vinci's famous sketch in his 1485 Codex Atlanticus (Fig. 1.1a) [1] and even further to Chinese legends describing high falls slowed by bamboo hats more than 4000 years ago [2]. Correspondingly, there has been an extensive amount of study concerning parachutes for a variety of applications throughout history. Though simple in design, the advantages of a deployable, fabric decelerator remain unmatched in many aerospace applications with minimal payload margins due to its high drag-to-mass ratio and small storage volume. Parachutes demonstrated their worth in the challenging task of returning humans safely from space in 1961, first when Yuri Gararin parachuted to Earth after ejecting from his Vostok vehicle [3] and then, a month later, when Alan Shepard lofted down into the Pacific Ocean inside of his Freedom 7 Mercury capsule under parachutes. These initial designs were improved to support larger payloads like the Apollo [4] (Fig. 1.2a) and Soyuz atmospheric Entry, Descent, and Landing (EDL) or "reentry" capsules, and similar systems are currently under development for new EDL vehicles, including NASA's Orion Multi-Purpose Crew Vehicle (MPCV) (Fig. 1.1b) and commercial designs by SpaceX, Boeing [5] (Fig. 1.2b), and Blue Origin, among others. Other systems, like the Space Shuttle and Sierra Nevada's Dream Chaser, utilize lifting-body aerodynamics in lieu of a main parachute for primary subsonic deceleration (but still depend on a smaller parachute for braking on the runway). However, the delicate, slender wings of these vehicles tend to increase the number of potential failure-modes during the aerodynamic heating process [6], making capsules with parachutes a more reliable approach for human exploration missions. In the less-dense atmosphere of Mars, parachutes do not achieve the same low terminal velocities as on Earth or Venus, but have still been used extensively in robotic missions for primary supersonic deceleration, after which, final deceleration is achieved through propulsive descent or cushioned impact. For future, crewed missions to Mars, increased payload requirements may exclude parachutes from the EDL design entirely in favor of fully-propulsive landings [7], but Earth's denser atmosphere and deep gravity well ensure that significant technological advancement, testing, and time are required before such a system could be certified to the same level of reliability as parachutes for human landings on our home planet.

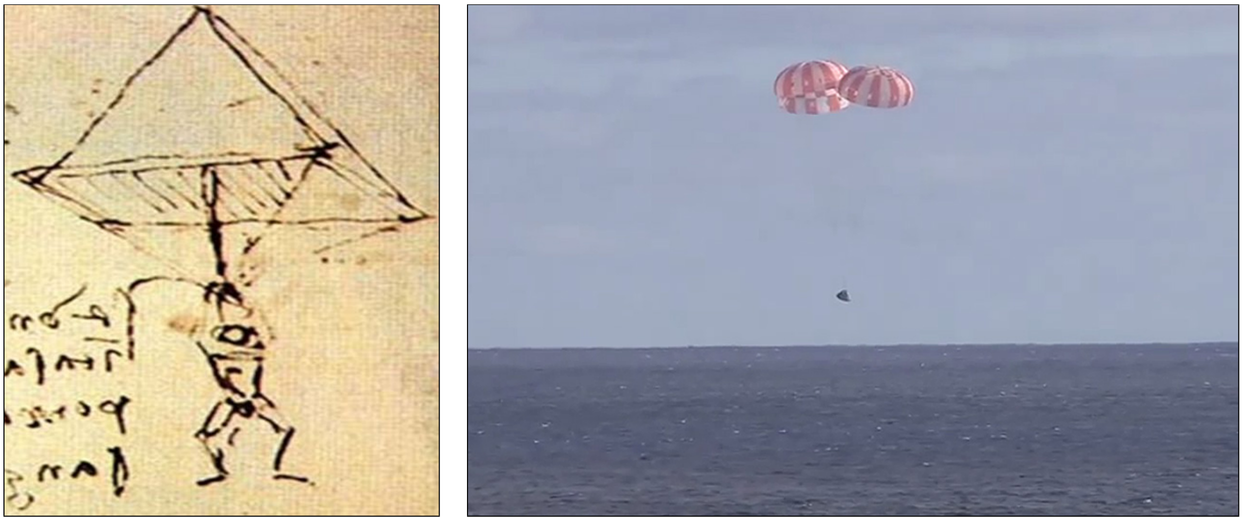

(a) Parachute sketch by da Vinci (circa 1485) [1]

(b) The EFT-1 (Exploration Flight Test) Orion MPCV spacecraft descending under parachutes after returning from orbit (2014) [8]

Figure 1.1: Ancient and modern parachute concepts

The Orion MPCV reentry capsule, developed for the National Aeronautics and Space Administration (NASA) by Lockheed Martin, utilizes a staged series of eleven parachutes, fabricated by Airborne Systems, for subsonic deceleration during atmospheric EDL, which provides a minimal terminal-velocity descent during touchdown [9]. The final stage is a cluster of three main parachutes that are designed to achieve a safe descent velocity, even during the low-likelihood event of a failure of one of the three. However rare, examples of this failure-mode have occurred in flight for similar vehicles, most notably during the return of the Apollo 15 mission, when an uncommanded propellant release deflated a single main parachute after deployment by partially severing its mooring [10], and, more recently, in the uncrewed pad abort test of the Boeing CST-100 capsule, where a loose pin prevented a drogue parachute from deploying a main. [11]. In both situations, the vehicle (as well as the crew, in the case of Apollo) returned safely to Earth, descending under only two of the intended three parachutes, as seen in Fig. 1.2.

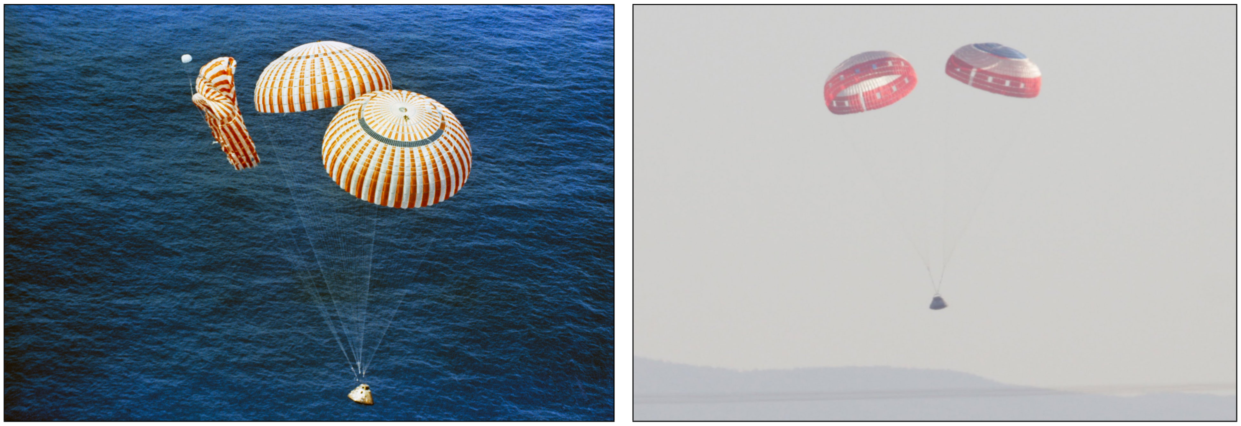
(a) Apollo 15 main parachute deflation due to accidental propellant release (1971) [10]

(b) Boeing CST-100 main parachute deployment failure during uncrewed pad abort test (2019) [11]

Figure 1.2: Flight examples of the single-parachute failure-mode for 3-canopy main parachute descent systems

Though nominally safe in terms of design loading on landing, Orion Capsule Parachute Assembly System (CPAS) flight testing of a 2-main-parachute cluster, which was representative of this single-parachute failure-mode, demonstrated that this configuration is potentially unstable and can exhibit pendulum-like, swinging motion of the parachutes about the attachment point on the Parachute Test Vehicle (PTV) in the direction normal to the plane created by the two parachutes and PTV [12]. Parachute cluster pendulum motion can introduce a number of safety hazards during landing, including increased rate of descent, a non-zero horizontal velocity component, and an off-design orientation of the capsule relative to the impact surface [13]. The root cause of parachute pendulum motion is alternating vortex shedding from the high-pressure cushion of air trapped in the parachute cavity [4, 14, 15]. Proximity of these shed ring vortices to the outer sides of the parachute induces lower pressures in those regions that tend to displace the parachute from its equilibrium at low angle of attack (α) and drive it back towards the centerline at high α. Pendulum motion was also observed in historical testing of the Apollo capsule's main parachutes, but was attenuated in the final design by reducing the strength of these shed vortices with the inclusion of a flow-through gap in the canopy geometry, which reduced the overall pressure inside of the parachute cavity [16].

The mitigation of pendulum motion in parachutes requires a fundamental understanding of this ring vortex shedding phenomenon and the relation of geometric and unsteady aerodynamic characteristics to its instigation. Traditionally, this insight is obtained through flight testing, where parachutes are tethered to payloads and dropped from cargo aircraft and occasionally through wind tunnel tests (WTTs), with sub-scale parachute models. Both testing methods are essential for demonstrating flight-worthiness but are also extremely costly, requiring many trials, the production of test articles, and financing for the personnel, aircraft, and facilities. Relatively recent advances in computer technology have allowed the field of Computational Fluid Dynamics (CFD) to mature, helping to ease the industry's dependence on traditional testing methods. CFD simulations can be run before any experimental testing has been conducted and can be used to inform the design of a drop test or wind tunnel test (WTT), reducing the total number of trials required and the overall cost of the testing process [15]. Additionally, a CFD model validated by comparison to experimental results can be utilized to extensively increment and improve an aerodynamic database at a more feasible cost than traditional testing methods and is uniquely useful for modeling exotic environments that are difficult or impossible to create on Earth, such as those experienced by supersonic decelerators during Mars EDL [17].

Together, flight testing, wind tunnel testing, and CFD form a so-called "three-legged stool" of aerodynamic design, each supporting the other. A design is ultimately qualified based on the completeness of understanding of its dynamical behavior throughout its flight envelope. Quantification of uncertainties pertaining to predicted flight behavior sets the limits for a vehicle's performance and mission. Determination of uncertainties is ultimately achieved via statistical analysis of dynamics models that depend upon aerodynamic loads databases created for the flight vehicle using the three-legged-stool approach. Traditionally, wind tunnel testing provides the bulk of the data, due to the lower cost and improved instrumentation compared to flight testing, while flight serves as the ultimate proof-of-concept for the design. In the modern process, CFD is capable of expanding the density of coverage provided by wind tunnel testing by orders of magnitude, but must be anchored and calibrated by flight and wind tunnel tests due to relatively large uncertainties of up to $\approx 10\,\%$ at some flow conditions.

For the case of parachute design, however, the stool is in need of a stronger CFD leg. Significant strides have been made in numerical modeling techniques of flows over parachutes, as is later discussed in detail in Section 1.2.3, but, prior to this work, the industry lacked a CFD parachute dynamics model that was sufficiently tested and validated to an extent acceptable for general use in parachute design; specifically, a validated model that simulates both the complex, unsteady, turbulent aerodynamics of the flow around a parachute with a known and quantifiable accuracy as well as the compounding dynamic effects of body motion interaction with aerodynamics. The focus of this work is the development and validation of a methodology for such a tool, and the product of this research is a description of that methodology.

1.2 Background

EDL of the Orion MPCV vehicle into the Earth's atmosphere is one of the most critical phases of its extensive flight envelope, which spans launch, orbit, and cislunar or interplanetary travel. Deceleration of the spacecraft begins with retropropulsion, decaying Orion's orbital trajectory into a parabola intersecting Earth. Once the capsule reaches the entry interface with the Earth's atmosphere, the bulk of its deceleration from orbital velocity begins and is accomplished by vehicle aerodynamic braking, inducing extreme heating that is buffered from the vehicle structure by the ablative heatshield. Aerodynamic braking reduces the capsule's speed relative to the atmosphere by $98.4\,\%$ down to a terminal velocity of $475 {}^{ft}\!/_{s}$, after which the vehicle is decelerated to its final descent velocity through a sequence of interconnected parachute stages, depicted in Fig. 1.3. First, the Forward Bay Cover Parachutes (FBCPs) are deployed explosively out of a mortar system and pull off the protective Forward Bay Cover (FBC) to reveal the remaining parachute stages. Then, drogue parachutes are fired, followed by pilot parachutes, which extract the main parachutes. Each stage reduces the vehicle velocity in a step-wise fashion to minimize the loading impulses on the parachutes, suspension risers, and crew. Both the drogue and main parachute clusters undergo several reefing stages, as well (indicated in Fig. 1.3 as "1st Stage", etc.), where circumferential reefing lines contain the inflation to smaller diameters for set intervals until timed cutters sever the lines, again, to minimize impulse. At last, the parachute-cluster-and-capsule system reaches its final descent rate of no more than $33 {}^{ft}\!/_{s}$ [18] (an additional $93\,\%$ reduction from capsule terminal velocity), at which it impacts the surface of the Pacific Ocean, completing its return to Earth.

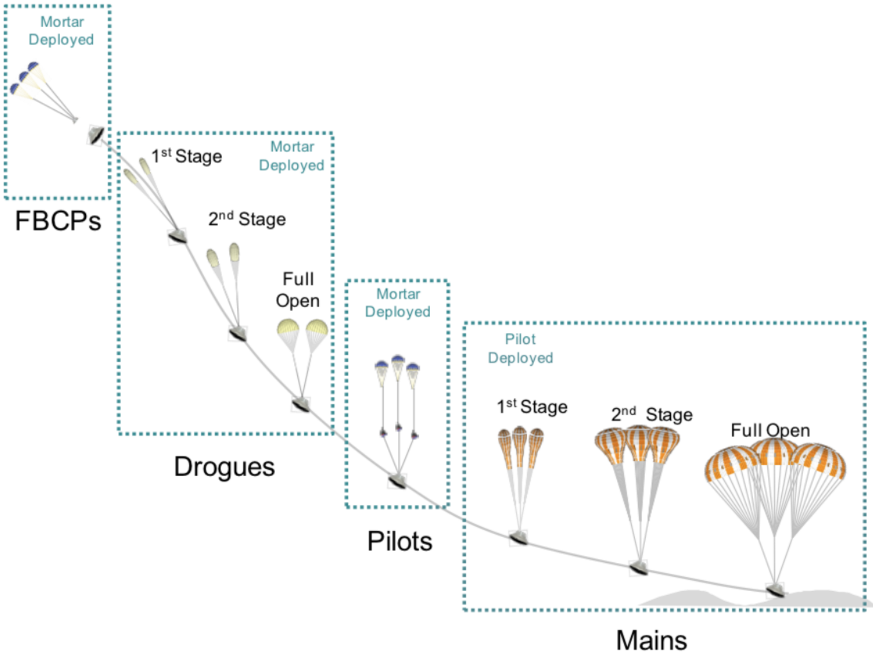

Figure 1.3: Orion Capsule Parachute Assembly System cluster and reefing stages for nominal descent [13]

1.2.1 Orion MPCV Main Parachute Geometry

The specific Orion parachute geometry considered in this research is termed the Engineering Design Unit (EDU), which refers to the canopy geometry employed in CPAS drop testing [12] and the National Full-scale Aerodynamics Complex (NFAC) wind tunnel test of the sub-scale parachute [13]. The EDU is a “ringsail” geometry [19] and can be visualized in Fig. 1.5. The parachute canopy is quarter-spherical in shape and has an inflated diameter of $D = 116\,\mathrm{ft}$. Fabric is omitted at the apex of the canopy to create an open, circular “vent”, allowing high-pressure air trapped in the canopy to escape and reducing the loading on the parachute and the risers and suspension lines connecting it to the payload. This feature is one example of “geometric porosity”, a directly-controllable design parameter that can be adjusted to achieve changes in the drag and stability performance of a parachute. Depictions of the parachute geometry terminology in this section can be found in Fig. 1.4a.

For most parachute geometries, the canopy is divided angularly around its circumference into equally-spaced sections (called “gores”), which are separated by vertical runners (tension lines called “radials,” in this application) that travel radially down from the vent apex at the aft of the

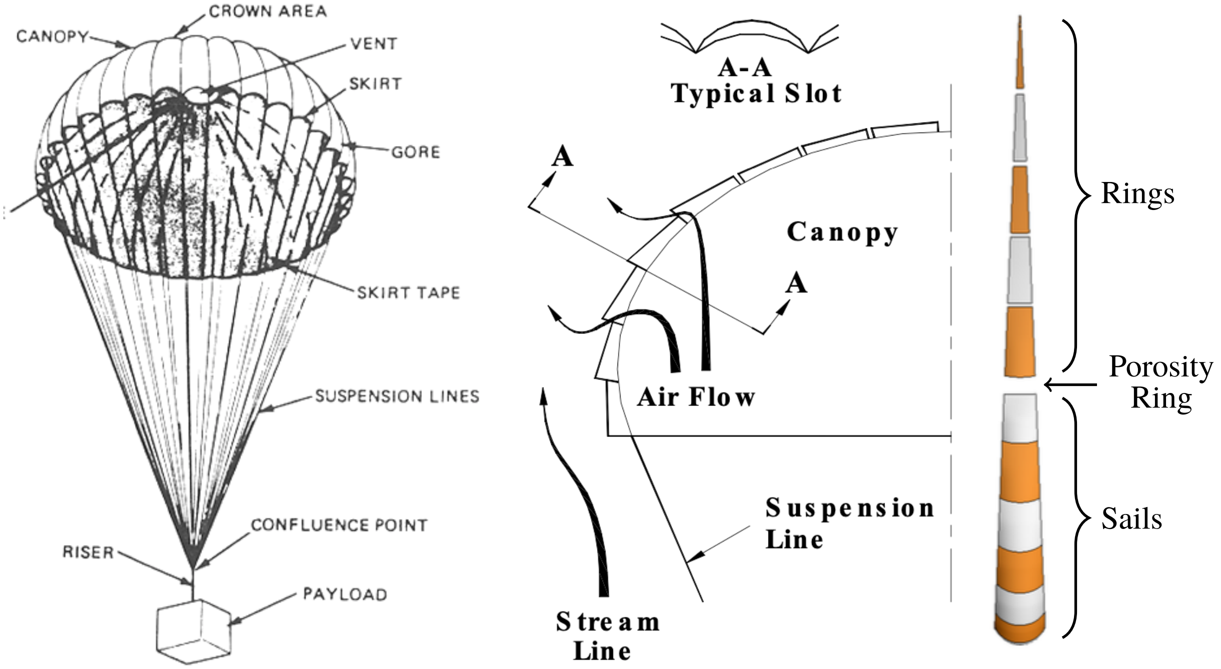

(a) Parachute geometry terminology for a simple cargo parachute geometry, where radial suspension lines running from the vent to the skirt divide the canopy into equal angular segments called gores [20]

(b) Cross-section of a ringsail parachute gore demonstrating inflation of each lower section's "fullness" into sails and the resulting changes to the canopy flow pattern [21]

(c) Top view of a single EDU parachute gore, with zero-fullness rings above the porosity ring and inflated sails below [18]

Figure 1.4: Parachute geometry features and terminology

canopy to the edge of the forward opening (called the "skirt"). A gore section is labeled as part of a complete canopy geometry in Fig. 1.4a, and a single gore of the EDU parachute is depicted in Fig. 1.4c. On a ringsail parachute, the canopy is also divided axially by circumferential runners strung perpendicularly to the radials into annular segments (called "rings") that can be separated by a finite gap to increase the geometric porosity. These two divisions create a grid-like layout of the canopy, where a single gore, continuous in Fig. 1.4a for a simple parachute geometry, is divided into sections or "panels" in the cross-sectional view of a ringsail parachute gore in Fig. 1.4b.

Gore panels on the lower portion of the ringsail parachute are designed with "fullness", or additional fabric slack on the windward side, that allows the panels to inflate into a "sail" and extend outside the arc of the nominally quarter-spherical shape of the canopy. Sails increase the drag and deceleration of the parachute by deflecting the freestream flow of descent and do so in a distributed manner, which is beneficial to the opening, structural, and stability characteristics of the parachute [21]. The extension of the sails and their deflection of the flow streamlines are depicted in Fig. 1.4b. Typically, the first few rings adjacent to the apex of the parachute are built with no fullness and conform to the quarter-spherical shape of the canopy (the three right-most sections in Fig. 1.4b), while the lower rings, which are more streamwise-oriented, are built with sails (the remaining sections to the left in Fig. 1.4b). On the ringsail, the zero-fullness upper annular segments are referred to as “rings” and the lower annular segments built with fullness are called “sails”, hence the name “ringsail.”

The Orion MPCV main parachute is specifically constructed of thirteen total annular segments: four rings separated by small gaps at the apex near the central vent and nine sails windward of the rings. A large $1.9\,\%$ gap is built between the first and second sails (ordered from aft to fore) to create additional geometric porosity.

1.2.2 Prior Orion Parachute Testing and Modeling

The Orion Capsule Parachute Assembly System was developed through an extensive drop testing campaign, during which testing of the single-main-failure two-parachute cluster demonstrated a tendency towards pendulum-like motion on multiple occasions [12]. This dangerous attribute motivated a detailed investigation by the National Aeronautics and Space Administration (NASA) and its associated partners to identify the nature of parachute instability and design changes that would improve stability without adversely affecting parachute drag performance. Analysis techniques included a simple, empirical pendulum dynamics model [12], static, rigid-body CFD analysis [18], a sub-scale/$35\,\%$ wind tunnel test, with parametric variations in parachute geometry [13], and subsequent drop tests, informed by the previous experiments, instrumented with Inertial Measurement Units (IMUs) and pressure sensors on the vehicle for the purposes of trajectory reconstruction.

In preparation for the $35\,\%$-WTT, a number of fixed-α CFD simulations of a rigid, nonpermeable, nonmoving parachute geometry were conducted [18]. A rigid body model was chosen for its known numerical accuracy and already-established role in developing aerodynamic database increments. A Fluid-structure Interaction (FSI), multi-disciplinary technique was not an option in this situation both due to time and cost constraints and due to a lack of a readily-available and strongly validated tool for this purpose. It is also important to note that the combination of the parachute reference length and freestream velocity at sea level yields a full-turbulent, flight Reynolds number of $Re = 2.36e7$, which is significantly large and potentially out of scope for many research CFD formulations and further motivated the use of conventional, Reynolds-averaged Navier-Stokes (RANS), rigid-body CFD. Parametric studies involving varied amounts of geometric porosity demonstrated that sail fullness could improve static stability with a notably smaller drag reduction than an equivalent porosity increase using a geometric porosity ring (gap). It was also shown that the root cause of pendulum motion is the singular phenomenon of the vortex ring emanating from the parachute skirt and not an interaction effect of the two-parachute cluster [16, 18], so a single parachute was simulated for simplicity.

Findings from the stationary CFD study were used to inform the design of the $35\,\%$-scale WTT in the NFAC $80'$x$120'$ test section [13]. This ground test of the EDU parachute obtained time-dependent tether loading and dynamic vent position photogrammetric data along stationary, swinging, and free-flight trajectories for multiple geometry configurations of the Orion main parachute. The results of this test were utilized to downselect the most stable candidates for further investigation in a drop testing campaign two weeks following the WTT. The rapid turn-around between ground and flight testing in this case was greatly facilitated by the additional insight provided by CFD before conventional testing began and highlights the importance of CFD as an equal player in the modern aerodynamic design process. The data from the WTT also serves as the validation set for the dynamic CFD model developed by the current research. Further flight testing of the downselected parachute configurations resulted in some evidence that geometric porosity alterations, as well as a Permanent Reefing Line (PRL) on skirt of main parachute to reduce inflation size, showed the potential ability to improve stability, but insufficient data was available to provide strong confidence. Thus, the baseline EDU parachute configuration was selected for the final design of Orion's descent system based on the decision that the low-likelihood of a main parachute failure did not justify the loss in nominal drag performance [15].

Though the main parachute design for Orion MPCV is complete, there still remains a great need for deeper understanding of the fundamental basis of parachute static and dynamic instability, both for the descent systems of reentry vehicles currently under development and for future parachute designs. The dynamic CFD model produced for this work provides these unique capabilities and insights into the dynamics of parachutes. It is a validated, functional tool that is ready to be used immediately by aerospace companies for comparative parachute design.

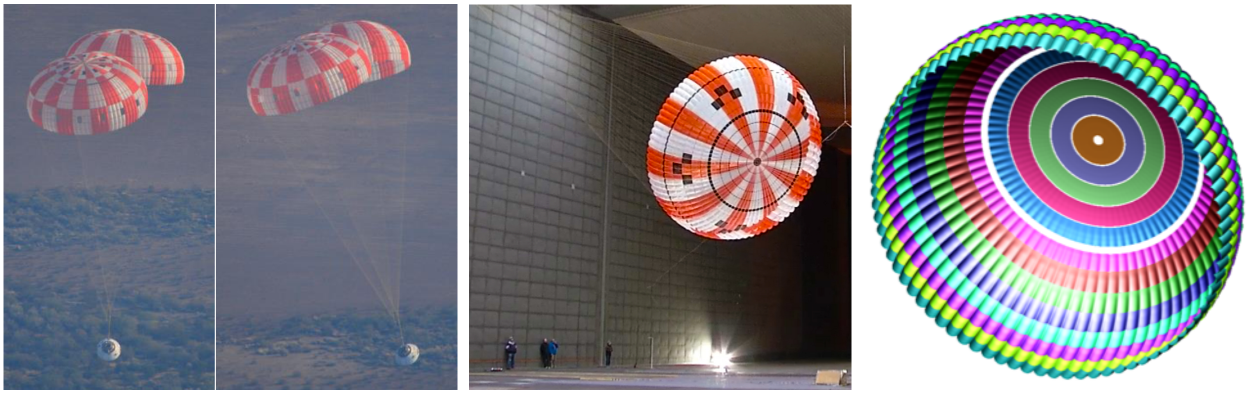

(a) Pendulum motion during PTV drop test [12] **(b)** NFAC wind tunnel test [13] **(c)** CFD surface grid

Figure 1.5: The three-legged stool design approach for the Orion EDU parachute including drop testing using a Parachute Test Vehicle (PTV) with two, full-scale EDUs, wind tunnel testing of a $35\,\%$-EDU in the NFAC $80'$x$120'$ test section, and a simplified computational surface model for CFD simulation

1.2.3 Current Techniques for Parachute Dynamics Modeling

This section provides a focused review on the current state-of-the-art in parachute modeling and motivates and justifies the specific modeling techniques chosen for this work. To date, there is an extensive history of modeling and simulating parachute dynamics for the purposes of analysis and design. Before the advent of fluid dynamics simulations by numerical solution of the Navier-Stokes equations (CFD), analytic models were developed to approximate the dynamics and aerodynamics of parachutes. Notable examples include a 5-DoF model for swinging dynamics with fixed roll angle (ϕ) by White and Wolf (1968) [22, 23] and a numeric, continuity-based, force-balance model of parachute canopy inflation by White (1974) [24]. Even in the age of CFD, analytic dynamics models are relied upon to create parachute stability databases, refine flight envelopes initially determined from ground and flight testing, and as validation data for more complex computational models based on CFD. Recent examples include a full 6-DoF dynamics model of a parachute tethered to a capsule by Ginn et al. (2014) [25] used for small-disturbance analysis and a sophisticated, nonlinear, two-parachute pendulum dynamics model based on the Output-Error method by Pei (2019) [26], which utilizes flight data from Orion MPCV parachute drop testing to further inform the realism of the model's dynamic response. Though relevant and essential in the full design cycle of a parachute descent system, analytic models are purely dynamics approximations, or empirical models based on flight data, and do not recover the complex, secondary influences on dynamic stability caused by the unsteady aerodynamics of the parachute wake and geometry features, which motivates the need for a reliable CFD analysis tool to investigate these additional effects.

CFD simulations of parachute flows can be divided into two primary methodologies:

1. Single-discipline CFD — Numeric solution of the equations of fluid dynamics for a rigid (non-deforming) parachute geometry

2. Multi-discipline Fluid-structure Interaction (FSI) — Coupling of the CFD solution with additional equations for parachute fabric structural dynamics and/or porosity

Parachutes are entirely composed of flexible fabric and bindings, which allow significant, time-dependent geometry changes during flight, including inflation and "breathing", a periodic expansion and contraction of the parachute skirt area. These structural changes can have a significant influence on the unsteady aerodynamics of the flow over a parachute, so it is obvious that a coupled FSI solver will provide a more realistic approximation of the overall dynamics of a parachute than a pure CFD solver. However, FSI is a significantly more complicated process that still in the development phase, so it is generally less validated than traditional CFD, has less well-defined uncertainties, and is less readily available in reliable, commercial CFD tool distributions. The following discussion will compare these two techniques, focusing on their utility for modeling the dynamics of fully-inflated, subsonic, parachute pendulum motion and the relative accuracy of their predictions, as established by comparison with experimental results.

Fluid-structure Interaction Methods for Parachute Modeling

FSI simulations have shown a promising ability to model parachute dynamics since as early as 1993, when Stein et al. [27] performed a simulation of an inflating Army C-9 parachute (a simple, cup-shaped, gored canopy with no geometric porosity), where the transient drag force was quantitatively comparable to experimental measurements, though significant improvement and testing was deemed necessary before "general use by the parachute community" [28]. Inflation shape modeling has been a primary focus of FSI parachute modeling development and has improved significantly over the years. Pruett et al. (2009) [29] used photogrammetry and water volume displacement to observe the inflating shapes of various hollow, flexible geometries and a model parachute canopy and demonstrated good comparison of time-dependent variance of the global form factors like opening radius and canopy volume to the structural solvers TENSION and the widely-used LS-DYNA. Fan and Xia (2014) [30] simulated the C-9 parachute at subsonic conditions with a novel FSI implementation and showed reasonable qualitative comparison of the inflation shape to observed parachute openings, and Shi et al. (2015) [31] performed FSI simulations at a higher Reynolds number (Re) and obtained an improved comparison of the unsteady drag during opening to flight data than Stein et al., though further refinement is required to match peak drag magnitude (factor of 2 difference).

Though inflation is a critical process in the operational cycle of a parachute and much insight into this process can be gained from FSI methods, its effects are generally transient and are less relevant to the specific issue of pendulum motion of parachutes, which typically occurs after the parachutes are fully inflated. During this phase of flight, deformations of the canopy shape can still occur, primarily in the form of a "breathing" expansion/contraction oscillation of the parachute opening, and can significantly influence the dynamics of a parachute's descent. FSI is also capable of modeling this behavior, one fundamental example of which was accomplished by Kim (2012) [32] using the Front Tracking Method, where breathing was shown to proportionally influence the rate of descent, as expected from flight observations. This work was expanded by Gao et al. (2017) [33] to include the additional realistic quality of fabric porosity, which reduced the overall drag of the parachute and minimized the breathing observed in an equivalent nonporous model. Similar simulations of the Orion MPCV parachute geometry considered in this dissertation have also been performed by Takizawa et al. (2011) [34, 35] using the Deforming Spatial Domain method, and an example solution is shown in Fig. 1.6b. These FSI simulations compared reasonably with the breathing frequency observed during drop testing as well as the descent rate and glide angle, suggesting good matching of the drag of the system. Pendulum motion was also observed in this study and achieved a swing frequency within $20\,\%$ of that observed in flight.

Considerable effort has also been made for the FSI modeling of supersonic Disk-Gap-Band (DGB) parachutes for the purposes of Mars EDL. Testing of these designs at realistic flight conditions on Earth is essentially impossible, which motivates the need for accurate FSI simulation, but, unfortunately, also corresponds to a lack of available flight data for simulation validation. A benchmark example by Karagiozis et al. (2011) [36] used Ghost fluid method with Large Eddy Simulation (LES) at $Re = 6e5$ and showed qualitatively good inflation comparisons, with $10\text{-}20\,\%$ error in loads compared to experiment. Visualization of the instantaneous, quasi-steady parachute shape in these simulations is available in Fig. 1.6a. A more recent implementation by Boustani et al.

(2019) [37] using Immersed Boundary Method (IBM) showed good comparison to literature for the deformation of a flat plate and showed qualitatively reasonable inflation dynamics for a supersonic Mars parachute at $Re = 1e5$. Huang et al. (2020) [38] offer a loads validation example for supersonic parachute FSI in their $Re = 4e6$ LES IBM simulation of the Curiosity Rover's parachute during EDL, where transient inflation drag force showed similar peak magnitude, unlike Shi et al.. Still, these formulations are less relevant to the Orion parachute pendulum application as supersonic, lower-Re flight conditions do not yield the same unstable aerodynamics observed at subsonic Mach number.

In short, FSI solvers can produce promising results that show complex, realistic parachute dynamic behaviors, but most comparisons of parachute FSI to experiment are either only qualitative in nature, constrained to specific laminar Re flight conditions, or exhibit significant accuracy error on the order of $20\,\%$. FSI is the technology of the future for parachute modeling, but is currently not mature enough for general engineering purposes in parachute design, where known uncertainties are essential for creating operational flight database increments.

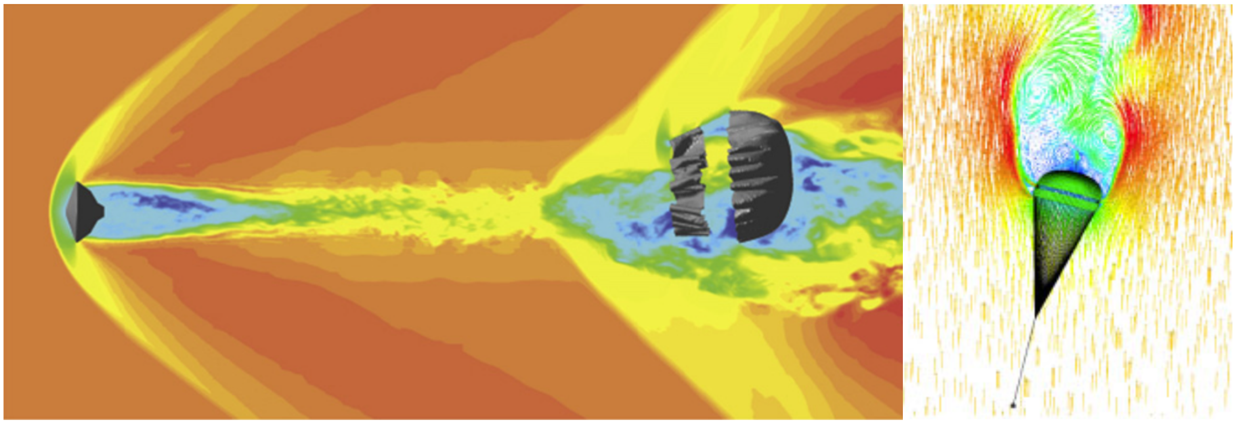

(a) Supersonic Mars parachute a capsule wake [36]

(b) Subsonic Orion MPCV parachute [34]

Figure 1.6: Fluid-structure Interaction (FSI) simulation solutions for parachutes of various designs

Rigid-Body CFD Methods for Parachute Modeling

As an alternative to FSI, traditional, rigid-body CFD is a mature technology widely accepted for many aerospace industry applications and offers a number of advantages:

- Well-validated, widely-distributed commercial codes with known uncertainties

- High-order accuracy solvers for high-Re flows

- Advanced turbulence modeling options

Though the omission of a structural dynamics solver requires that the simulated parachute's geometry be artificially rigid, this can be considered a reasonable approximation for situations where a parachute is fully-inflated and does not exhibit "breathing", which is (for many parachute designs) a transient effect that occurs immediately post-inflation [33], after which a parachute's geometry can be considered time-independent. Indeed, McQuilling et al. (2011) [39] demonstrated good accuracy of the unsteady surface pressure fluctuations in a subsonic $Re = 3.65e5$ RANS simulation compared to a nonmoving, rigid parachute in a water tunnel test, as shown in the similar trend and magnitudes of the averaged canopy pressure distributions compared in Fig. 1.7a. Rigid-body CFD of parachutes has also been adapted to incorporate fabric porosity modeling, as in the simulation by Dinzl et al. (2013) [40] of an Orion drogue parachute (different from the main parachute considered in this work) in the wake of the Orion MPCV capsule at $M = 0.26, Re = 2.7e5$ using Detached Eddy Simulation (DES) turbulence modeling, where drag coefficient was shown to match within $5\,\%$ for α up to $30°$. High accuracy has also been demonstrated for supersonic parachute simulations by Kitamura et al. (2020) [41] for a supersonic DGB parachute at $Re = 6.6e5$ using DES, where geometry-specific flow features like the separation of the vortex leaving the porosity gap ("Pattern 1" in Fig. 1.7b) compared well to oil flow experiments and unsteady pressure fluctuations in the parachute skirt cavity were nearly identical to measured frequencies.

An additional advantage of traditional CFD methods over FSI is the reduced computational cost, allowing modeling of more complicated geometries, both of the parachute canopy itself, and of external flowfield interactions like the wake of the attached EDL spacecraft or an aircraft wake in the case of a cargo parachute simulated by Bergeron et al. (2021) [42, 43, 44]. This work, based on the earlier efforts by Serrano et al. (2003) [45], shows the complex interactions between the bluff-body wake of a stationary, air-drop cargo attached to a cluster of fixed, fully-inflated, high-fidelity, ring-slot parachutes engulfed in the downwash behind the wing of a C-17 aircraft (see Fig. 1.8a). Though further validation data is necessary to evaluate the uncertainties associated with the accuracy of these complex simulations, they highlight the degree of aerodynamic complexity that CFD can provide over traditional analysis techniques like the previously-discussed parachute dynamics

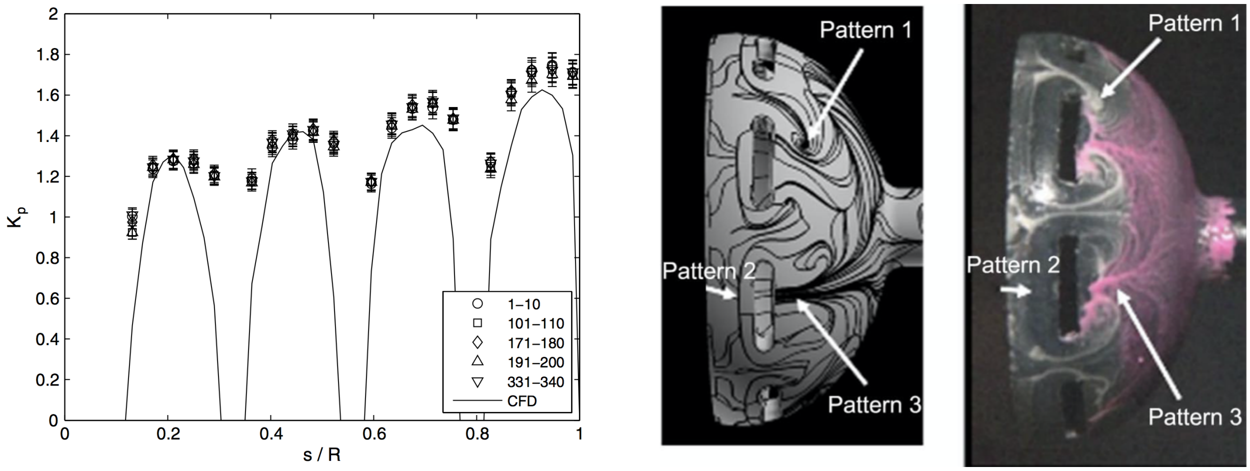

(a) Subsonic surface pressure coefficient (C_P) [39]

(b) Supersonic oil flow patterns (CFD: left, Experiment: right) [41]

Figure 1.7: Comparisons of static, rigid parachute CFD simulations to experimental results

models. Another example of a high-fidelity, stationary, rigid parachute geometry CFD simulation is the work performed by Greathouse and Schwing (2015) [18] for the full-scale Orion MPCV main parachute that is the basis of the work for this dissertation. This CFD study demonstrated the usage of static CFD as a design tool for the purpose of identifying more statically stable geometries to be employed in a following WTT and also the ability to approximate fabric porosity with additional geometric porosity for the purposes of matching induced aerodynamic loads.

Though the accuracy of modeled unsteady loads is important for understanding the dynamics of a parachute, modeling the dynamics of pendulum motion is equally essential if true dynamic stability characteristics are expected to be recovered. Moving-mesh CFD represents a multi-disciplinary technique that allows for the motion of rigid-geometry grids relative to the freestream flow, either by sliding of overlapping, interpolated grids [46] or by cell deformation of the computation domain. Motion of free bodies driven by integrated aerodynamic loads is a long-standing capability of commercial CFD solvers that has been utilized for simulating store separation from aircraft [47] and as source data for probabilistic analysis of debris impact to the Space Shuttle [48], among other uses. However, pendulum dynamics require that the drag body must be anchored to a stationary attachment point, either fixed in space and representative of a WTT or attached to a payload of sufficient mass to encourage a steady descent. Pioneering efforts in simulating this kind of motion were made by Arai et al., first for highly simplified, supersonic, rigid parachute allowed to swing in

1-DoF (shown in Fig. 1.8b) [50], then later, for a simple, rigid, subsonic, laminar ($Re = 2600$), cup-like hemisphere capable of a 3-DoF, translational descent without rotation [49]. These simulations were purely demonstrative in nature, due to their unrealistic flow conditions and simple motion, but they serve as a framework for moving-mesh techniques that can be adapted to greater levels of realism and accuracy. Addressing a related deficiency of rigid-body CFD, Vasile (2017) [51] demonstrated an option for incrementally approaching full FSI by adding a prescribed, oscillating cup-like canopy to emulate breathing at $Re = 3e4$ using DES. Though the structural approximation was not responsive to the aerodynamic loads experienced in the simulation, the periodic change in the size of the cup opening served to modulate the drag in a manner representative of other breathing simulations and tests referenced in this review.

Finally, a significant improvement in the motion fidelity of parachute pendulum CFD simulation can be found in the work by Guruswamy (2017) [52], which coupled the OVERFLOW CFD solver to external structural and dynamics models using a C++ wrapper. The parachute geometry was a simple cup with a vent and shape deformations were computed at each time step according to aerodynamic loads and simplified equations for thin shells subject to external pressure. The parachute

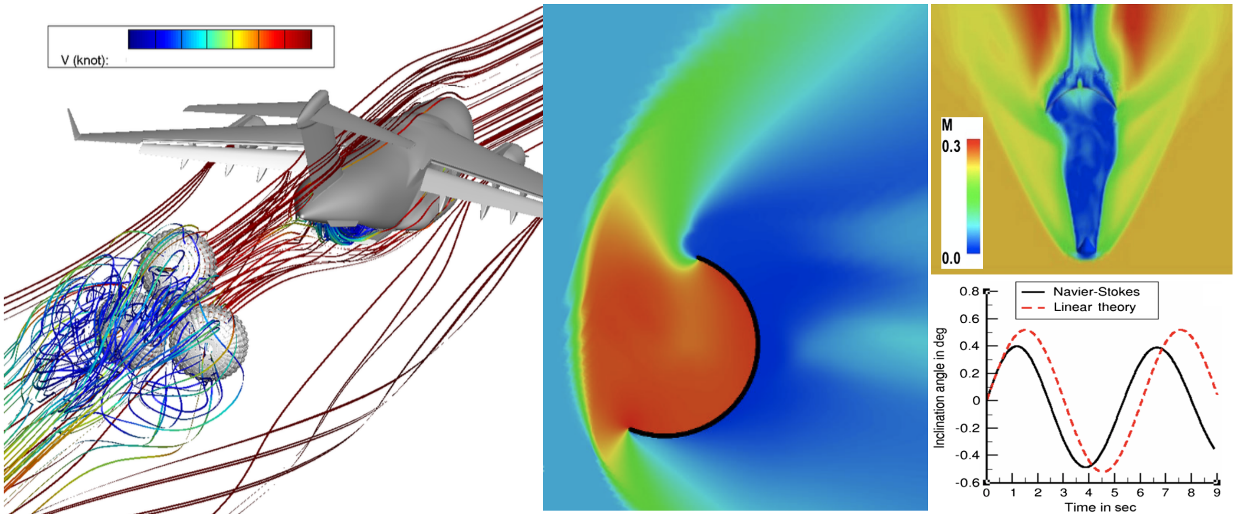

(a) Nonmoving, high-fidelity parachute cluster simulated in the wake of a C-17 aircraft [42]

(b) 1-DoF swinging, supersonic parachute-like body [50]

(c) 3-DoF, small-angle, planar swinging of a capsule-parachute system compared to linear theory [52]

Figure 1.8: Stationary- and moving-body CFD simulations of various-fidelity, rigid, parachute geometries

was attached to a capsule-like geometry to create a pendulum system and was allowed to move in 3-DoF (two translational, one rotational). RANS turbulence modeling was used for $Re = 2e6$ subsonic freestream flow, as pictured in Fig. 1.8c (a rudimentary grid spacing may have been used based on the uncharacteristic features for subsonic flow in the image). The resulting swinging motion was only for relatively small angles ($0.4°$) compared to flight-observed pendulum behavior, but compared reasonably in amplitude and frequency (excluding a phase shift) to the author's analytic, linear theory formulation (Fig. 1.8c). Though the geometry and motion characteristics of this simulation are too simplified to provide direct insight into the Orion MPCV main parachute design, this formulation demonstrates that high-order accuracy, non-FSI CFD solvers like OVERFLOW can utilize coupled moving-mesh capabilities to model a parachute-like pendulum system. This is the closest example in the literature to the desired, validated, engineering design model for parachute dynamic stability that serves as the motivation for this dissertation.

Turbulence Modeling Techniques for Parachutes

Turbulence modeling is an important subtopic of parachute simulation techniques, as the blunt shape of the parachute cavity facing the incoming flow generates a massively-separated, bluff-body wake that is dominated by turbulent effects such as oscillatory vortex shedding. The number of chaotic turbulent interactions are multiplied for complex parachute geometries like the Orion MPCV EDU, where small geometry features like gaps and sails create high speed jets and vortices, which further influence the unsteady dynamic response of the parachute to aerodynamic loads. In order to accurately recover the dynamic stability characteristics of a subsonic parachute undergoing pendulum motion, it is necessary to realistically model the time-accurate nature of the unsteady wake, which requires sophisticated turbulence modeling techniques that are often not available in research codes like some the examples of FSI and coupled-motion, rigid-body CFD parachute simulations in the previous section.

The greatest fidelity form of turbulence simulation is Direct Numerical Simulation (DNS) or the discrete solution of the complete Navier-Stokes equations, the formulation of which is summarized in Eqn. 1.1 with the incompressible form of the continuity and momentum equations.

$$\begin{aligned} &\nabla \boldsymbol{V} = 0 \\ &\rho \frac{D\boldsymbol{V}}{Dt} = \rho \boldsymbol{g} - \nabla P + \mu \nabla^2 \boldsymbol{V} \end{aligned} \tag{1.1}$$

No modeling is required for this form of simulation, as turbulence is solved directly, so any inaccuracies in the results will depend only on the discretization of the domain and the continuum, Newtonian fluid constraints. However, the requirement that all scales of turbulence within the domain be resolved requires fine computational meshes and results in infeasibly large grid systems for realistic flows, limiting modern implementations of DNS for bluff-body wake simulations on current-technology distributed computing systems to Re well below that of a full-scale parachute [53, 54].

Fortunately, the Navier-Stokes equations can be reduced to a form that is realizable for complex geometries and flow by today's computing standards by expressing the equations as mean and fluctuating components via the process of Reynolds decomposition. This results in the Reynolds-averaged Navier-Stokes (RANS) equations of which the incompressible momentum equation is provided as an example in Eqn 1.2.

$$\rho \frac{D\overline{\boldsymbol{V}}}{Dt} = \rho \boldsymbol{g} - \nabla \overline{P} + \mu \nabla^2 \overline{\boldsymbol{V}} - \rho \frac{\partial}{\partial \boldsymbol{x}_j} \left(\overline{\boldsymbol{u}_i' \boldsymbol{u}_j'} \right) \tag{1.2}$$

where $\overline{(\,)}$ represents a mean quantity (time-averaged) and $(\,)'$ represents a perturbation quantity.

Unfortunately, this formulation results in an additional "Reynolds stress" term $\rho\overline{\boldsymbol{u}_i'\boldsymbol{u}_j'}$, causing the unknowns to outnumber the equations by one and creating the infamous turbulence "closure" predicament. Solution for the additional RANS unknown must be accomplished though estimation of the $\rho\overline{\boldsymbol{u}_i'\boldsymbol{u}_j'}$-term by statistical modeling. Over the years, a long line of RANS turbulence models have been produced to notable success, but some inherent inaccuracy is introduced by the nature of modeling. A slight variation of RANS is Unsteady Reynolds-averaged Navier-Stokes (URANS), which is a time-accurate method that requires all grid cells to be fixed to the same global time step, allowing URANS to capture unsteady behavior of the mean flow. This form of modeling has been shown to accurately model the bulk features of the unsteady, turbulent wake behind bluff-bodies like circular cylinders (See Fig. 1.9a [55]), which is essential for the simulation accuracy required by this work. Accordingly, references to "RANS" after this section for parachute modeling processes will always imply a URANS treatment.

In recent years, the advantages of DNS in resolving fine turbulent behavior have been brought into use in simulations of complex flows by the superimposing strategy of LES, where turbulent structures that are large enough to be resolved on the chosen computational grid are solved with DNS, and smaller turbulent scales are solved with a turbulence model, referred to as a Subgrid-

Scale model (SGS). This methodology predicts much higher-fidelity turbulence spectra and unsteady behavior but has more computational demand than traditional RANS. This method was adapted by Spalart (2009) [56] to operate with RANS as the SGS, effectively combing the two methods into a hybrid-RANS/LES method termed Detached Eddy Simulation (DES) [56]. Both LES and DES show merit over URANS in the solution of bluff-body wakes, but DES is generally accepted as the more mature and feasibly implemented of the two, showing good comparison to experiment in simulations of flow over spheres [57, 58] (Fig. 1.9b), reentry capsules [59], and bluff vehicles [60]. URANS has proven to be effective in specific applications of bluff-body wake modeling, especially for cases where boundary layer transition and separation locations are predicted accurately [61, 62] as is the case with the sharp-edged parachute skirt, but it is essential to the current research to investigate the effect of higher-fidelity turbulence modeling strategies. Section 4.3.5 of this dissertation addresses this open research question.

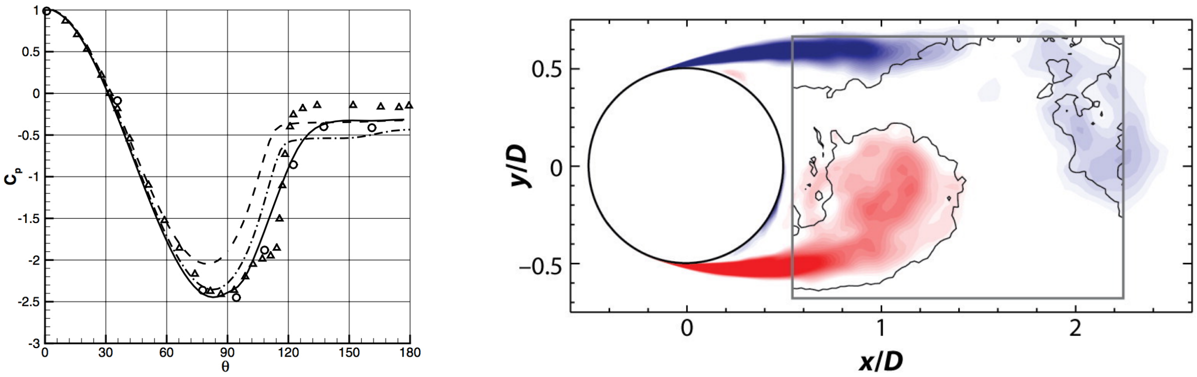

(a) Mean surface pressure distribution over a cylinder computed with various turbulence models: (—) LES, (- -) RANS, (-.-) URANS at $Re_D = 1.0e6$ compared to experiments at (○) $Re_D = 1.2e6$ and (△) $Re_D = 6.7e5$ [55]

(b) Colored vorticity contours from DES simulation of flow over a sphere compared to experiment (outlined) [58]

Figure 1.9: Demonstrations of turbulence modeling accuracy in resolving complex features of bluff-body wake flow

1.3 Research Aims

The primary objective of this research was to develop a model that produces general engineering design results for parachute dynamic stability from unsteady aerodynamic loads modeling. Sufficient confidence has been gained in the model's accuracy such that it may be of immediate use in the current development of parachute systems. The model was also designed to operate on an economically viable budget and schedule.

Model development was achieved incrementally and depended upon a series of assumptions and simplifications that are discussed and justified in Section 4.2.1 and most significantly include a rigid tether and parachute geometry composed of nonporous fabric. This objective was achieved according to following research aims:

Aim I Develop and validate a CFD model of an aerodynamically-driven pendulum

- Leverage aerodynamically-driven motion with off-body constraints in the OVERFLOW CFD tool
- Validate model accuracy by comparison of motion to a numeric analog model based on drag coefficient
- Demonstrate model ability to predict motion caused by complex aerodynamics using a simple parachute-analog geometry
- Assess the accuracy of the unsteady aerodynamics predicted by prescribed motion simulation compared to an equivalent aerodynamically-driven simulation

Aim II Develop and validate a CFD model of parachute pendulum motion

- Prescribe a high-fidelity, rigid-geometry CFD model of the Orion parachute to a motion track observed in the sub-scale WTT of the same geometry
- Assess the validity of assumptions and simplifications made in the CFD model through parametric study
- Validate accuracy of the model by comparison to WTT dynamic loads

Aim III Demonstrate effectiveness and utility of the parachute design model by performing a parametric study of the effects of geometric porosity on dynamic stability

A number of research questions arose in conjunction with the establishment of these Aims and the review of the literature in the previous section, and it was an additional goal of this work to utilize the CFD pendulum model to provide answers to these questions, summarized below:

1. Can rigid-body CFD with nonporous surfaces accurately model parachute pendulum aerodynamics?
    (a) Is self-similarity maintained when scaling from wind tunnel test conditions to flight?
    (b) Can the dynamic load trends of a parachute WTT be recovered in CFD simulation without modeling wind tunnel wall effects?
    (c) Is URANS turbulence modeling sufficient for recovering the bulk unsteady nature of moving, bluff-body wakes?
2. Is the root cause of parachute dynamic instability the same shed ring vortex that causes static instability?
3. Does CFD of moving bodies prescribed to a known motion track resolve aerodynamic responses as accurately as aerodynamically-driven motion?
4. Can the simple parachute-analog model be used as an accurate surrogate of true parachute aerodynamic response?

A summary of the insight this research provides towards understanding and answering these questions can be found in Section 6.2.

1.4 Summary

Numerous spacecraft are currently in development that will depend parachutes to safely return humans to Earth. It has been demonstrated that certain parachute designs are unstable and exhibit pendulum motion during descent, inducing potentially life-threatening hazards. Deeper understanding of the fundamental sources of this instability is required to improve future parachute designs. Significant understanding can be gained from traditional experimental methods like flight and wind tunnel testing, but CFD simulation of parachutes has the potential to provide additional insight into the unsteady aerodynamics and complex flows that drive parachute motion and dynamics.

This chapter motivated the need for a validated engineering tool with known numerical accuracy that is capable of simulating unsteady parachute aerodynamics and dynamic response. The research effort detailed in this work fills this open niche in parachute modeling by leveraging moving-mesh, rigid-body CFD and obtaining validation by comparison to empirical dynamic loads. This tool will aid in the design of safer parachutes by providing insight into the root cause of pendulum motion. Though FSI research models provide hyper-realistic modeling of parachute geometry deformation, they do not yet have well-defined uncertainties due to a lack of extensive comparison to experimental data and general use of simpler, lower-order-accuracy numerics. In contrast, RANS turbulence modeling and rigid-body, overset CFD are industry standards and have established practices for incrementing aerodynamic databases with defined uncertainties.

The following chapters will detail the development and validation of this model, beginning with the description of relevant modeling and analysis tools utilized and created in support of the research (Chapter 2), followed by the development of an aerodynamically-driven pendulum in the OVERFLOW CFD tool (Chapter 3) and the prescribed motion simulation of pendulum motion of the Orion MPCV main parachute, which is compared to the sub-scale WTT (Chapter 4). The model is then utilized for a stability design demonstration (Chapter 5), after which the relevant findings of this work are summarized, research questions are answered, and potential future work is proposed (Chapter 6).

Chapter 2

Pendulum Modeling and Analysis Tools

2.1 Introduction

Aerodynamically-driven pendulum (or “aeropendulum”) models, with unsteady fluid dynamics computed using CFD solution of the Navier-Stokes equations, were developed in this work using the OVERFLOW CFD tool and leveraging its built-in moving-mesh capabilities. Part of this research was to ensure the realism of pendulum motion predictions of this OVERFLOW model, so an analogous numeric model was also developed to serve as validation data. This model was based on the numeric solution of the Ordinary Differential Equation (ODE) governing a 1-DoF, drag-driven, aerodynamic body, where drag was assumed to be proportional to a constant drag coefficient (C_d).

This chapter will detail the design of the numeric aeropendulum model and the supporting pendulum dynamics derivations. An overview of the capabilities of the OVERFLOW CFD tool and the framework for simulating aeropendulum motion will also be given. Finally, this chapter will showcase a Python-based, dynamics post-processing software tool called `overdyn`, which was created as part of this work to analyze the aeropendulum results produced by OVERFLOW.

2.2 Drag-Based, Numeric, Pendulum Motion Model

A numeric, ODE model of the pendulum motion a two-dimensional cylinder driven by its aerodynamic drag was developed for the purposes of calibrating and validating constrained pendulum motion using OVERFLOW CFD tool. This section details the design of this model and provides derivations of relevant dynamic and aerodynamic relations for understanding, modeling, and analyzing aerodynamically-driven pendulum motion utilized throughout this work.

2.2.1 Aerodynamically-Driven Pendulum Dynamics

The ODE model of the circular cylinder aeropendulum is designed by making certain simplifications and assumptions, including:

1. The drag body, or pendulum "bob," is fixed to a rigid, pinned tether, allowing 1-DoF rotation in the direction of pitch/swing angle (θ)
2. The pendulum bob experiences a constant drag coefficient (C_d)
3. The pendulum bob geometry is symmetric, so the net aerodynamic force ($\boldsymbol{F}_{aero}$) acts in the direction of effective velocity (V_{eff})
4. This bluff-body flow is pressure-dominated, and viscous stresses can be assumed secondary
5. No gravity force is present, for simplicity ($\boldsymbol{g} = 0$)

The free-body diagram of this system is presented in Fig. 2.1.

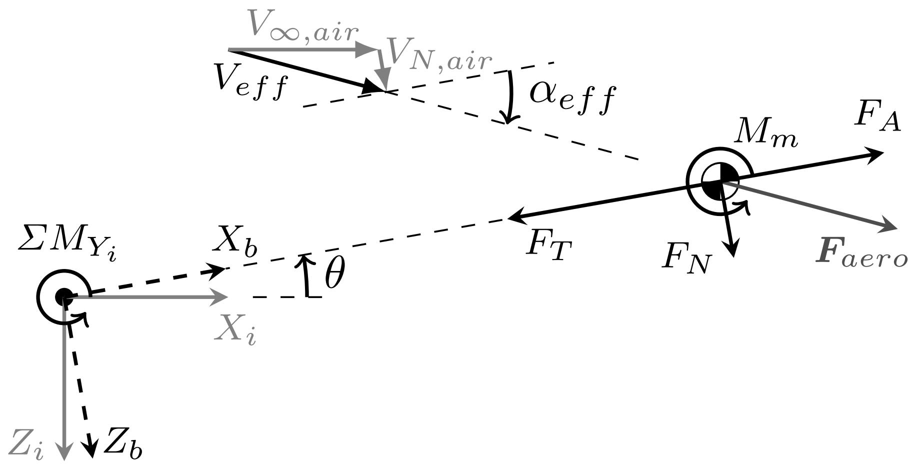

Figure 2.1: Free-body diagram for an aerodynamically-driven pendulum swinging counter-clockwise with a positive pitching rate $\dot{\theta}$, where the pendulum bob is located to the right and is rigidly tethered by its center of mass to the inertial origin to the left (all velocities shown are of the relative air)

As there are no gravity effects present in the system, the only remaining forces acting on the pendulum bob are those of the tether F_T and $\boldsymbol{F}_{aero}$, the sum of the aerodynamic viscous and pressure shear stresses induced by the freestream flow and relative swinging motion of the pendulum. For the purposes of stability analysis and pendulum motion modeling, it is convenient to decompose

$\boldsymbol{F}_{aero}$ into its body reference frame components: axial force (F_A) and normal force (F_N). Using this terminology, the equations of motion governing the swing of the 1-DoF aeropendulum can be expressed with the single relation in Eqn. 2.1:

$$\Sigma M_{Y_i} = I\ddot{\theta} = F_N \cdot R + M_m \tag{2.1}$$

where the pendulum is driven by the total pendulum moment (ΣM_{Y_i}) acting about the tether location, which is proportional to the angular acceleration ($\ddot{\theta}$) of the pendulum by the moment of inertia $I = mR^2$, where R is the swing radius of the pendulum. For the pressure-dominated, bluff-body flow over a circular cylinder, the aerodynamic pitching moment (M_m) can be assumed to be entirely due to viscous shear and, thus, secondary in magnitude compared to the pressure normal stress driving pendulum motion in the body-frame normal direction (Z_b). Thus, the driving force of the pendulum reduces to:

$$I\ddot{\theta} = F_N \cdot R \tag{2.2}$$

This relationship serves as the basis for the nonlinear, state-space model of θ, where F_N can be computed analytically according to the following process.

Due to the constraints of pendulum motion, the V_{eff} of the aerodynamic body can be computed analytically as the vector sum of freestream velocity (V_∞) and the tangential swing velocity (V_N) of the pendulum, which is proportional to the pendulum angular velocity ($\dot{\theta}$) as

$$\begin{gathered} V_{N,air} = -\dot{\theta}R \\ V_{eff} = \sqrt{(V_{N,air} + V_{\infty,air}\sin\theta)^{\,2} + (V_{\infty,air}\cos\theta)^{\,2}} \end{gathered} \tag{2.3}$$

where $_{air}$ denotes the reference frame of the relative air. Using a constant value of C_d, taken from experimental results [63], the definition of C_d provides an estimator for the aerodynamic forces acting on the pendulum as a function of its motion.

$$|\boldsymbol{F}_{aero}| = \frac{1}{2}\rho {V_{eff}}^2 C_d \tag{2.4}$$

The constant C_d assumption is reasonable for relative pendulum velocities of the same order of magnitude as V_∞ and assuming that an average accounting of the C_d magnitude and direction is representative of the net effect of a symmetrically oscillating, unsteady wake. Finally, $\boldsymbol{F}_{aero}$ can be decomposed into its body-frame components based on effective angle of attack (α_{eff}),

$$\alpha_{eff} = \tan^{-1}\frac{V_N}{V_\infty} \tag{2.5}$$

to compute the total force in the body normal direction (ΣF_{Z_b})

$$F_N = \Sigma F_{Z_b} = |\boldsymbol{F}_{aero}| \cdot \sin(\alpha_{eff}) \tag{2.6}$$

This system differs from that of a gravitational pendulum in that the direction of the effective velocity and total drag is not always parallel with the freestream flow, creating a tangential drag component that opposes the swinging motion, producing a damping effect.

2.2.2 Aerodynamically-Driven Pendulum State-Space Model

Equation 2.2 in the previous section serves as the governing equation of motion for the 1-DoF aeropendulum. By selecting the state variables:

$$\begin{aligned} x_0 &= \theta(t) \\ x_1 &= \dot{\theta}(t) \end{aligned} \tag{2.7}$$

and substituting the result for F_N in Eqn. 2.2 into the governing equation Eqn. 2.1, we can obtain the nonlinear, state-space representation for the simple, 1-DoF, aerodynamic pendulum as in Eqn. 2.8.

$$\begin{bmatrix} \dot{x}_0 \\ \\ \dot{x}_1 \end{bmatrix} = \begin{bmatrix} x_1 \\ \\ \frac{\rho C_d}{2m} \frac{\frac{R^2}{V_\infty} x_1^3 + 2R x_1^2 \sin x_0 + V_\infty x_1}{\sqrt{\left(\frac{R}{V_\infty} x_1\right)^2 + 1}} \end{bmatrix} \tag{2.8}$$

This complex system of ODEs is discretized and solved numerically using Euler methods in a Predictor-Corrector fashion (forward for x_1, backward for x_0), as formulated in Eqn. 2.9.

$$\begin{aligned} x_1 &= x_{1,old} + \dot{x}_{1,old} \Delta t \\ x_0 &= x_{0,old} + \dot{x}_1 \Delta t \end{aligned} \tag{2.9}$$

For small time steps, this methodology produces a sufficiently stable solution for the realistic estimation of the aerodynamically-damped, oscillatory motion of a cylindrical aeropendulum. In practice, the drag coefficient of the moving pendulum was greater than that of the stationary experimental result ($C_d = 0.7$), so the numeric model required calibration to the CFD solution by assuming a fixed value for drag coefficient equal to the average obtained from the moving CFD simulation ($C_d = 0.7625$). Functionality of this model as a validation source for CFD pendulum motion can be found in Section 3.4.2.

2.3 Pendulum Motion in the OVERFLOW CFD Tool

2.3.1 OVERFLOW CFD Solver Overview

For the parachute pendulum simulations, a CFD solution for unsteady aerodynamics coupled with an accurate motion estimator is readily implemented the OVERFLOW CFD tool. OVERFLOW is a three-dimensional, time-accurate, implicit, finite-differencing Navier-Stokes solver that utilizes structured, overset grid systems for domain discretization [64, 65, 66]. Complex surface geometries are modeled with overlapping volume meshes and domain connectivity algorithms determine efficient interpolation stencils between separate grids. The overset method allows for the discretization of complex systems, with many components or complex surface geometry features, and the curvilinear nature of the meshes allows the express implementation of multiple, high-order accuracy schemes. Newton sub-iteration allows time-accurate convergence of the implicit solution by fixing a global time step while performing additional solution iterations at each grid point using a local time step. OVERFLOW also offers a suite of specialized turbulence models, including an Unsteady Reynolds-averaged Navier-Stokes (URANS) implementation of the two-equation Shear Stress Transport (SST) model and a Delayed Detached Eddy Simulation (DES) model that will be employed by this work.

2.3.2 OVERFLOW Grid Motion Overview

A distinct advantage of the overset methodology (for this application) is that the interpolated, overlapping nature of the grid system provides a native framework for handling changes in the relative positions of grids. This nature is leveraged in OVERFLOW's built-in Geometry Manipulation Protocol (GMP) tool [46], which is an Extensible Markup Language (XML) interface that allows the specification of rigid-body motions (relative grid movement) in real-time during the CFD solution according to two primary methods. The first allows prescribed motion according to an arbitrary, time-dependent function. The second, called "Aero6DOF", allows free movement of a rigid body under the influence of integrated aerodynamic loads and user-specified, external forces and moments. This is achieved by computing the aerodynamic forces on the body at every time step and then estimating the resulting dynamic response according to Newtonian dynamics with a 6-DoF, finite Euler scheme. A pseudocode describing this implementation of the CFD-motion coupling for Aero6DOF-mode is available below in Fig. 2.2.

Figure 2.2 OVERFLOW Geometry Manipulation Protocol Aero6DOF-mode Pseudocode

```
for each component do
    Integrate inertial-frame aerodynamic forces/moments
    Transfer inertial-frame moments to Center of Mass (COM) location
    Add gravity to forces
end for
for all Parent/Child hierarchy levels from top to bottom do
    for each component in current hierarchy level do
        Inherit dynamics from Parent component
        Transfer forces and moments to body frame
        if user-specified externally-applied loads then
            Add applied loads
        end if
        if user-specified motion constraint then
            Null forces/moments in constrained DoFs
        end if
        for multiple Euler-method dynamics predictor-corrector stages do
            Estimate COM velocity $\boldsymbol{V}$ from Newton's 2nd Law ($\boldsymbol{F} = m\boldsymbol{a}$)
            Estimate COM angular rates $\boldsymbol{\omega}$ from Euler parameters
            if user-specified motion constraint then
                Null rates ($\boldsymbol{V}, \boldsymbol{\omega}$) in constrained DoFs
            end if
            Compute discrete movement of COM over time step ($\boldsymbol{V} \times \Delta t$)
            Update Euler parameters based on new COM, $\boldsymbol{V}$, $\boldsymbol{\omega}$ estimates
        end for
    end for
end for
```

GMP is also capable of constraining a free-body's motion in any specified degree-of-freedom. Motion constraints are achieved by first computing the aerodynamic forces and moments in the body reference frame and then nulling any linear/angular velocity and force/moment that corresponds to a constrained degree-of-freedom. As originally implemented, motion constraints could only be applied about the moving body's COM (e.g. an aircraft store or falling debris), but in OVERFLOW 2.2p (released in 2019) and later versions, Aero6DOF-mode was enhanced with expanded motion constraint capabilities, allowing for the motion in any of the six-degrees-of-freedom to be nulled relative to any given location in the inertial reference frame. This framework is sufficient for describing a rigid pendulum's constant-radius orbit about a tether point, where the acceleration along the tether direction is zero (nulled) and the parallel orientation of the body axial direction with the tether direction is maintained by nulling any rotation about the body's centroid. In OVERFLOW GMP, the above constraint is achieved for a two-dimensional simulation by constraining translation in all three directions and rotation about the two non-symmetry-plane axes (X and Z in Fig. 2.1), leaving the body free to move only by rotating within the two-dimensional plane, centered about the location of the pendulum's tether.

A question of interest in this work was what accuracy of realism is recovered when using prescribed motion to simulate an observed motion track, compared with an equivalent simulation with aerodynamically-driven motion. The exactness of prescribed motion makes it a more efficient process, both in the start-up cost of implementing a model and in the amount of simulation time required to complete a motion track, as Aero6DOF is often influenced by unpredictable, secondary effects. Section 3.4.3 performs a direct comparison of these two methods to demonstrate the utility and accuracy of prescribed motion when emulating a known trajectory.

2.4 Pendulum Motion Analysis Tools

Several post-processing tools were developed in order to analyze the output from OVERFLOW Aero6DOF-mode moving-body CFD simulations. At each time step, OVERFLOW CFD tool performs surface integrations of pressure and viscous shear stresses on user-specified surfaces and outputs this data as nondimensional force and moment coefficients in the system's inertial reference frame. For moving-mesh simulations, GMP additionally logs the COM position and rates and Euler state parameters of specified moving-bodies. However, for applications like dynamic stability analysis of moving geometries, it is essential that aerodynamic loads and trajectory parameters be expressed in the body reference frame. Additionally, corrections must be made to the nondimensional forces and moments to account for relative aerodynamics not observed by the simulation (e.g. local dynamic pressure variations due to relative motion) to ensure self-similarity of the reported results.

To overcome this deficiency, a Python-based, dynamics post-processing and visualization software suite called `overdyn` was developed as part of this work. This tool parses and processes the raw output of an OVERFLOW CFD run and returns a time history for a moving, aerodynamic body, with stability-relevant data including: corrected aerodynamic coefficients in stability-relevant coordinate frames, the V_{eff} and effective aerodynamic rates and attitudes including rate of angle of attack ($\dot{\alpha}$) and total angle of attack (α_T),

$$\alpha_T = \cos^{-1}\frac{V_{X_b}}{V_{eff}} \tag{2.10}$$

which consolidates angle of attack (α) to a single plane for any given side-slip angle (β), and the stability-axis orientation angles roll angle (ϕ), θ, and yaw angle (ψ). The general procedure for calculating these parameters is outlined in Fig. 2.3.

Options for parachute industry-specific conventions are also available in `overdyn` for improved consistency in comparisons to parachute wind tunnel and flight experiments. These include an option to report forces and moments in the parachute reference frame ($|_P$), which is rotated 180° about the y-axis/θ-axis relative to that defined for the aerodynamic pendulum in Fig. 2.1 and is discussed further in Section 4.2.2. Additionally, the forces and moments in the missile reference frame are computed by rotating about the aerodynamic clocking angle (ϕ_c), which is calculated as:

$$\phi_c = \text{arctan2}\left(-V_{Y_b}, V_{Z_b}\right) \tag{2.11}$$

where the velocities are components in the body reference frame. This transformation allows the direct comparison of missile-frame normal force coefficient ($C_{N,m}$) between axisymmetric geometries, regardless of state during precessing or rolling motion.

In addition to post-processing raw data from OVERFLOW moving-body simulations, `overdyn` also contains a number of features to improve the efficiency and consistency of the CFD analysis process. A plotting library and command-line utility `postfomoco` provides an interactive vehicle

Figure 2.3 Overdyn 6-DoF Aerodynamics Processor Pseudocode

```
Input: CFD I/O files: a.fomoco, a.sixdof, over.namelist, mixsur.fmp, Config.xml
Output: Time history of body aerodynamics, motion, and loads
Parse raw OVERFLOW aerodynamic loads and motion output
    Parse freestream conditions and reference parameters from OVERFLOW input files
    Read inertial-frame force/moment coefficients (from a.fomoco)
    Compute total coefficients from the sum of pressure+viscous components
    Read COM position, velocity, angular velocity, and Euler parameters (from a.sixdof)
Data Initialization
    Synchronize sample rate of loads and motion
    Initialize unit consistency tracking
Correct coefficients for updated reference parameters and/or symmetry boundary conditions
Calculate nondimensional simulation time and physical time
Compute relative aerodynamics
    Compute total relative wind velocity of moving body (sum of freestream and COM velocity)
    Compute $V_{eff}$ in body reference frame
    Compute relative wind angles $\alpha$, $\alpha_T$, $\beta$
    Compute aerodynamic rates: $\dot{\alpha_T}$
if parachute reference frame ($|_P$) then
    Rotate $180°$ about $+Y$
end if
Compute attitude angles $\phi$, $\theta$, $\psi$ based on Euler parameters
Compute local dynamic pressure ($\overline{q}$) based on $V_{eff}$ and $\alpha$
if local $\overline{q} \neq \overline{q}_\infty$ then
    Correct aerodynamic coefficients
end if
for each Reference Frame $\in$ [body, lift/drag, missile based on $\phi_c$] do
    Rotate inertial forces/moments to Reference Frame
end for
```

for `overdyn`, which can post-process a CFD cases in-place and return plots of the loads convergence and residual history and can report average values and tolerance bars for the purposes of aerodynamic database construction. `overdyn` also utilizes and provides a class-based, lightweight unit-tracker `units.py`, which is standalone for use in other applications, if desired. `units` provides fail-safe unit conversions by prescribing units to individual parameters, providing to-and-from unit conversions, and is capable of batch-converting the entire data set between standard unit systems. `overdyn` is capable of large text file handling, which is accomplished by incrementally saving the processed force/moment data to disk. This is a requirement for moving-body runs that require an extremely large number of time steps. Finally, `overdyn` is documented automatically using Sphinx autodocs, which provide an HTML-based reference for every class and function within the module to facilitate new users in learning the code's capabilities and functionalities. Examples of the code documentation are shown in Fig. 2.4.

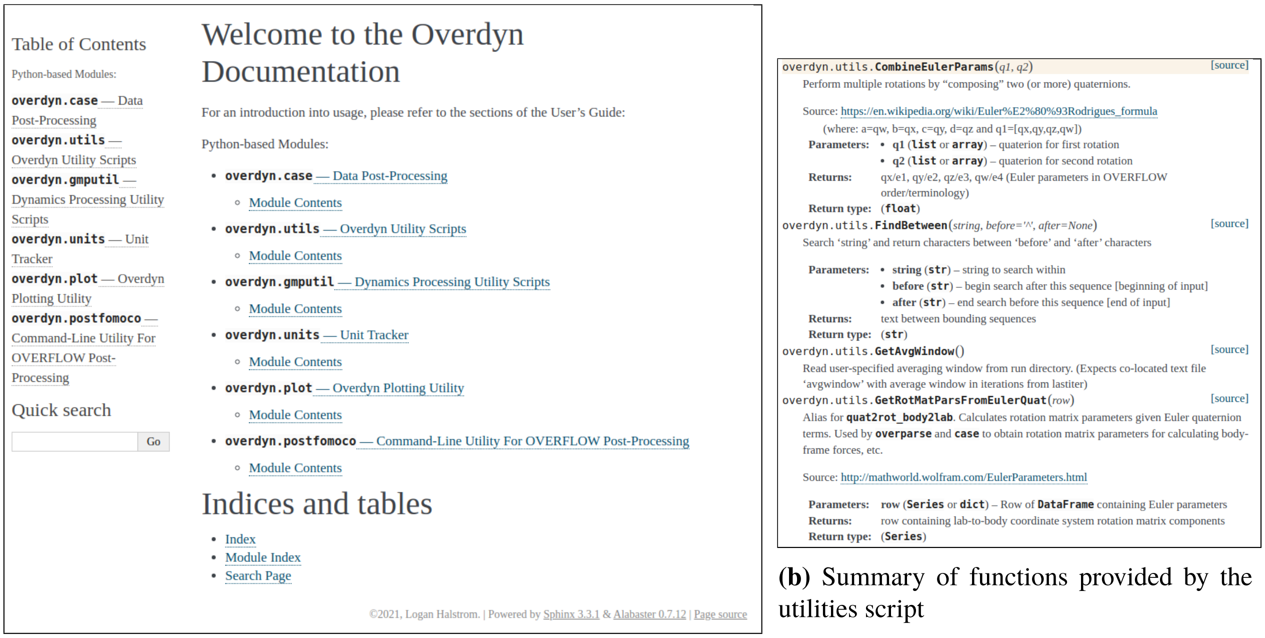

Table of Contents

Python-based Modules:

overdyn.case — Data Post-Processing
overdyn.utils — Overdyn Utility Scripts
overdyn.gmputil — Dynamics Processing Utility Scripts
overdyn.units — Unit Tracker
overdyn.plot — Overdyn Plotting Utility
overdyn.postfomoco — Command-Line Utility For OVERFLOW Post-Processing

Quick search

Go

Welcome to the Overdyn Documentation

For an introduction into usage, please refer to the sections of the User's Guide:

Python-based Modules:

- **overdyn.case** — Data Post-Processing
  - Module Contents
- **overdyn.utils** — Overdyn Utility Scripts
  - Module Contents
- **overdyn.gmputil** — Dynamics Processing Utility Scripts
  - Module Contents
- **overdyn.units** — Unit Tracker
  - Module Contents
- **overdyn.plot** — Overdyn Plotting Utility
  - Module Contents
- **overdyn.postfomoco** — Command-Line Utility For OVERFLOW Post-Processing
  - Module Contents

Indices and tables

- Index
- Module Index
- Search Page

©2021, Logan Halstrom. | Powered by Sphinx 3.3.1 & Alabaster 0.7.12 | Page source

(a) Documentation table of contents

`overdyn.utils.`**`CombineEulerParams`**(*q1, q2*) [source]

Perform multiple rotations by "composing" two (or more) quaternions.

Source: https://en.wikipedia.org/wiki/Euler%E2%80%93Rodrigues_formula

(where: a=qw, b=qx, c=qy, d=qz and q1=[qx,qy,qz,qw])

Parameters:
- **q1** (**`list`** or **`array`**) – quaterion for first rotation
- **q2** (**`list`** or **`array`**) – quaterion for second rotation

Returns: qx/e1, qy/e2, qz/e3, qw/e4 (Euler parameters in OVERFLOW order/terminology)

Return type: (**`float`**)

`overdyn.utils.`**`FindBetween`**(*string, before='^', after=None*) [source]

Search 'string' and return characters between 'before' and 'after' characters

Parameters:
- **string** (**`str`**) – string to search within
- **before** (**`str`**) – begin search after this sequence [beginning of input]
- **after** (**`str`**) – end search before this sequence [end of input]

Returns: text between bounding sequences

Return type: (**`str`**)

`overdyn.utils.`**`GetAvgWindow`**() [source]

Read user-specified averaging window from run directory. (Expects co-located text file 'avgwindow' with average window in iterations from lastiter)

`overdyn.utils.`**`GetRotMatParsFromEulerQuat`**(*row*) [source]

Alias for **`quat2rot_body2lab`**. Calculates rotation matrix parameters given Euler quaternion terms. Used by **`overparse`** and **`case`** to obtain rotation matrix parameters for calculating body-frame forces, etc.

Source: http://mathworld.wolfram.com/EulerParameters.html

Parameters: **row** (**`Series`** or **`dict`**) – Row of **`DataFrame`** containing Euler parameters

Returns: row containing lab-to-body coordinate system rotation matrix components

Return type: (**`Series`**)

(b) Summary of functions provided by the utilities script

Figure 2.4: Example documentation for the Python-based aerodynamic post-processing software suite `overdyn`

2.5 Summary

This chapter detailed the development of modeling techniques for aerodynamically-driven pendulums, including a numeric, ODE, state-space model for use as a pendulum motion validation data source and a CFD model for high-fidelity simulation of the unsteady aerodynamics of a parachute. Equations of motion for a 1-DoF aeropendulum were derived and represented in state-space form for the purposes of the numeric model. Also detailed were the capabilities of OVERFLOW GMP and the implementation of an aeropendulum using off-body constraints to represent a rigid tether. The performance of these two models will be compared in Section 3.4.1 of the following chapter. In addition, a dynamics post-processing software suite `overdyn` was developed to support the analysis of aeropendulum runs in OVERFLOW and comparisons to experimental results from parachute tests. This Python module provides raw aerodynamic data processing capabilities and can automatically produce visualizations for analysis of simulation convergence.

Chapter 3

Aerodynamic Pendulum CFD Model

3.1 Introduction

In this chapter, functionality of the Aero6DOF-mode pendulum constraint in OVERFLOW Geometry Manipulation Protocol (GMP) (introduced in Chapter 2) is demonstrated and tested using an aerodynamic pendulum model, hereby referred to as an "aeropendulum". The development and validation of this model was the focus of Research Aim I. Simple geometries were selected for this analysis in order to facilitate the prototyping process. These geometries consist of:

1. A two-dimensional cylinder (validation model)
2. A concave cup with a vent and porosity gap, or "scoop" (parachute-analog model)

and provide the dual advantages of:

1. Simple, intuitive flow physics that can be modeled analytically (cylinder only)
2. Simplified meshes, reducing computational resources demand and facilitating prototyping

Validation and calibration of the OVERFLOW aeropendulum model was achieved by simulating the cylinder as a 1-DoF pendulum (constrained to rotate within a single plane with a rigid tether). This CFD model was tuned by comparison to wind tunnel experiments, which allowed the selection of the optimal simulation settings for resolving physically accurate bluff-body flow. Validation of the accuracy of the coupled motion solver was then demonstrated by comparison to a numeric, state-space model based on drag coefficient estimates for bluff bodies. Further assurance about the functionality of the aeropendulum model was derived by simulating simple, asymmetric geometries with a pendulum constraint and observing the resulting motion qualitatively. These geometries included a flat plate weathervane, a cylinder with a tab, and a half-cylinder. The simple parachute-analog, or “scoop” was then utilized to explore the functionality of pendulum-constrained Aero6DOF-mode when applied to an asymmetric drag body with both two- and three-dimensional flow and motion. The effective use cases for both prescribed and Aero6DOF pendulum motion simulations were compared and contrasted. This prototype Aero6DOF simulation also served as the testbed for developing generalized aerodynamic data processing scripts that were not dependent on the prescribed motion equations to determine aerodynamic attitudes and rates. Portions of this chapter were originally published in the conference proceedings for the 2021 AIAA AVIATION Forum [68].

3.2 Model Development

3.2.1 Assumptions and Simplifications

The simplified aerodynamic pendulum CFD models developed for this work are based directly on the static, rigid parachute CFD analysis conducted by Greathouse and Schwing [18]. Rigid parachute CFD best practices established in this study are followed and expanded by the current research. The aeropendulum model is subject to the following assumptions and simplifications with justifications:

- The pendulum tether attaches to the body at its centroid (simple design)
- The tether is rigid, maintaining the body’s radial distance from the tether pivot point and preventing relative roll and yaw of the body about its centroid (the effect of these degrees-of-freedom are secondary to the swing of the pendulum)
- No gravity force is present (its influence is minimal compared to the magnitude of the aerodynamic drag)
- Unsteady Reynolds-averaged Navier-Stokes (URANS) turbulence modeling may omit some of the unsteady behaviors of the flow (the averaged result is representative of the primary driving factors of pendulum motion)

- The primary dynamic characteristics of a parachute can be approximated with a simplified geometry (dependent primarily on the hollow hemispherical shape)
- The geometrical and inertial properties of the flight-scale parachute can be proportionally reduced (comparisons will be made using similarity parameters)

A reference length based on diameter of $10.5in$ was selected for the aeropendulum for simplicity of prototyping and to match the size of the models used in wind tunnel experiments conducted by Roshko (1961) [63] in the California Institute of Technology Co-operative Wind Tunnel. Compatibility between the aerodynamics and motion of the simple aerodynamic pendulum and the full-fidelity Orion parachute simulations in Chapter 4 was maintained through the geometric and aerodynamic scaling. The ratio of the aeropendulum reference length (hemisphere diameter) $D_{ref,scoop}$ to that of the Orion parachute $D_{ref,chute}$ served as the geometry modification factor for the pendulum system.

$$\frac{D_{scoop}}{D_{chute}} = \frac{10.5in}{1392in} = 0.0075 \tag{3.1}$$

This factor was applied to determine the length of the aeropendulum tether in order to maintain comparable periodic motion.

Inertial properties of the aeropendulum were also derived by scaling those of the parachute by the reference length ratio. The mass of the parachute is calculated as the sum of the apparent mass of the trapped air within the parachute m_{air} and the actual mass of the fabric constructing the parachute m_{fabric}. The apparent mass of trapped air is computed by multiplying the density of air by the apparent volume of trapped air:

$$AV = \frac{1}{2} \cdot \frac{4}{3}\pi \left(0.7\frac{D}{2}\right)^3 \tag{3.2}$$

The mass of the parachute structure is calculated from its known weight $W \approx 300lb$, and for the purposes of inertial scaling of the aeropendulum, an area density of the parachute fabric can be determined by dividing mass by the surface area of the parachute (hemisphere)

$$SA = \frac{1}{2} \cdot 4\pi \left(\frac{D}{2}\right)^2 \tag{3.3}$$

obtaining $\rho_{fabric} = 0.06929 {}^{kg}/{}_{m^2}$.

The resulting mass for the full scale parachute is

$$\begin{gathered} m_{chute} = m_{fabric} + m_{air} \\ m_{chute} = \rho_{fabric}\frac{1}{2} \cdot 4\pi \left(\frac{D^2}{2}\right) + \rho_{air}\frac{1}{2} \cdot \frac{4}{3}\pi \left(0.7\frac{D}{2}\right)^3 = 136kg + 4862kg = \boxed{5000kg} \end{gathered} \tag{3.4}$$

while the equivalent mass of the aeropendulum, scaled by its reference length is

$$m_{scoop} = SA\rho_{fabric} + AV\rho_{air,scoop} = 7.7g + 8g = \boxed{16g} \tag{3.5}$$

Because the mass scaling is not directly proportional to length scaling, the resulting motion of the extremely-light aeropendulum was very sensitive to the aerodynamics. This introduced high-frequency oscillations to the motion, which had a negative effect on simulation stability and required a small time step to accurately resolve changes due to rapid relative grid motion. Ultimately, the mass of the aeropendulum was increased by an order of magnitude ($m_{scoop} = 183g$) to improve simulation stability.

OVERFLOW operates with nondimensional parameters for all internal functions, so the design mass of the aeropendulum was converted into nondimensional units as follows. The dimensional moment of inertia was calculated for a pendulum as

$$I = mR^2 \tag{3.6}$$

where R was the length of the pendulum tether. Then, the mass and moment of inertia were nondimensionalized (denoted by *) as

$$\begin{aligned} m^* &= \frac{m}{\rho_\infty L^3} \\ I^* &= \frac{I}{\rho_\infty L^5} \end{aligned} \tag{3.7}$$

where L is gridunit ($^1/_{12}ft$). The resulting nondimensional moment of inertia for the scaled aeropendulum is

$$\begin{gathered} I = 0.4lb/32.174\frac{slug}{lb}\left(20.5in \cdot \frac{1ft}{12in}\right)^2 = 0.0366slug \cdot ft^2 \\ I^* = \frac{0.0366slug \cdot ft^2}{9.13 \times 10-3\frac{slug}{ft^3}\left(\frac{1}{12}ft\right)^5} \approx \boxed{1e6} \end{gathered} \tag{3.8}$$

The final scaling of the parameters for the aeropendulum model are summarized in Table 3.1.

Table 3.1: Scaling of aerodynamic and inertial simulation parameters between the aerodynamic pendulum and the parachute

Parameter	Chute	Scoop	Reasoning
L_{ref} (D)	$1392in$	$10.5in$	Match experiment, prototyping
L_{tether}	$1.95D$	$1.95D$	Pendulum motion similarity
Initial swing angle (θ_0)	$5°$	$5°$	Parachute swing angle in wind tunnel
Reynolds number (Re)	2.36×10^7	8.4×10^6	Match experiment, both fully turbulent
Mach number (M)	0.15	0.15	Scaled, incompressible M
Mass (m)	$5000kg$	$183g$	Direct scaling, then compensation

3.2.2 Grid Development

CFD simulations using OVERFLOW employ implicit, finite-differencing methods on structured, overset grids [64, 65, 66]. Overset grid systems for this work were developed using Chimera Grid Tools (CGT) [69, 70, 71] and its associated Graphic User Interface (GUI), Overgrid [70]. CGT Build Scripts were used to generate the near-body volume grids for the pendulum body and off-body, Cartesian box grids in a systematic and parameterized fashion. The resulting two-dimensional grid systems are depicted in Fig. 3.1, where the near-body pendulum geometry consists of one or more periodic grids defining the surface and providing fine wall spacing for boundary layer turbulence modeling and is nested in a succession of box grids that extend a total of 430 cylinder diameters in all directions to the far-field and provide fine, isotropic grid spacing close to the pendulum body to resolve the unsteady aerodynamic behavior of the wake.

Overset region communication, interpolation stencils, and cell blanking (visible as cell blanking and overlap in Fig. 3.1) was achieved for moving-mesh simulations of the cylinder using Domain Connectivity Function (DCF) [72, 73, 74]. DCF allows cell blanking and stencils to be recomputed at each time step when there is relative overset grid movement. For the simple cylinder geometry, DCF hole cutting was achieved by “X-raying” the pendulum geometry to provide a cutting surface. A finite cutting distance was specified from this surface within which overlapping box grid cells were not considered in the final aerodynamic solution. For the more complex geometry of the scoop, mixed-mode PEGASUS 5/DCF (implemented in OVERFLOW 2.2m in 2017 [75]) was utilized, where the automatic domain connectivity pre-processor PEGASUS 5 [76] was run prior to flow simulation to obtain optimized cell blanking and interpolation stencils for the near-body, as these grids are constrained such that there will be no change in their relative orientation to each other during Aero6DOF motion simulation. Adaptive domain connectivity between the near-body and the off-body box grids was achieved in-simulation using traditional DCF X-ray cutting of the wakebox (green) by the bodybox (brown), visibly apparent on the borders of Fig. 3.1d.

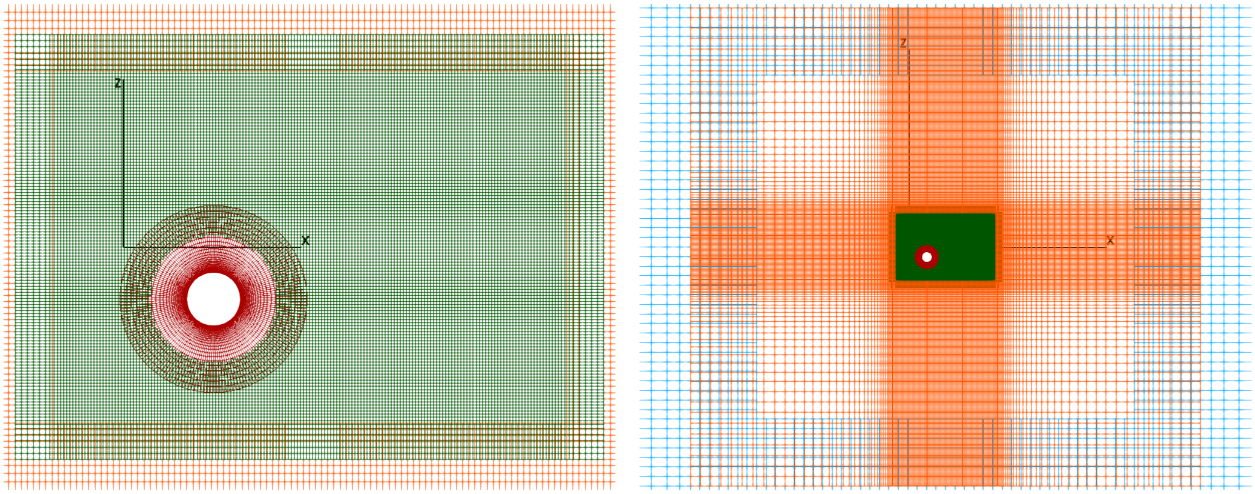

(a) Cylinder near-body grid (Red) and wakebox (Green)

(b) Overlapping, box grids extending (out of frame) to far-field

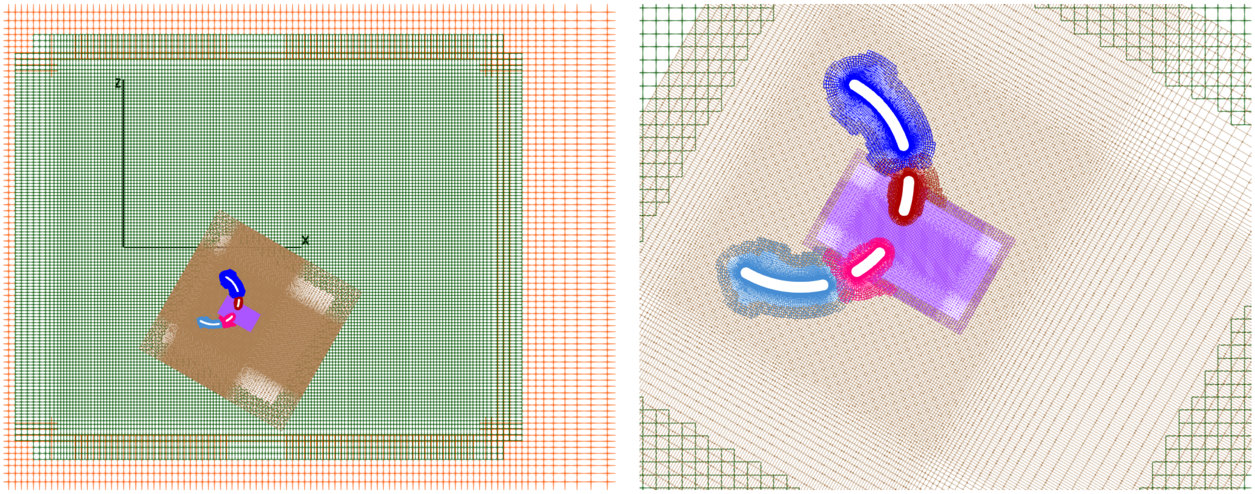

(c) "Scoop" with motion-tracking bodybox (Brown)

(d) Scoop with gap and vent filled by body and vent boxes

Figure 3.1: Two-dimensional cylinder and "scoop" pendulum grid systems, consisting of a moving pendulum geometry volume grid and static surrounding box grids, with the pendulum tethered to the origin and held at an initial swing angle of $\theta = 30°$

Geometries

The 2D cylinder surface and near-body mesh consisted of a single “O”-grid (Fig. 3.1a), while the scoop consisted of a finite-thickness, “C”-shaped cross-section separated into four unique body quadrant “O”-grids by a central vent and two symmetric side gaps (Fig. 3.1d). These cross-sectional interruptions are representative of a vent and geometric porosity ring gap on a revolved, three-dimensional, hollow hemisphere geometry and allow flow-through effects similar to a Disk-Gap-Band (DGB) parachute, such as that of Mars Science Laboratory [17]. Due to its concave shape, the scoop grid’s near-body volume mesh extension was restricted to the inner diameter of the geometry, as any further growth would cause opposing faces to intersect each other. This lack of near-body extension was compensated for with an overlapping “bodybox” (Brown in Fig. 3.1d) that traveled with the scoop and, thus, remained stationary relative to it. The bodybox was made to have equivalent grid resolution and extension to the larger cylinder near-body grid, which is visible in the comparison of Figs. 3.1a and 3.1c. A finer “ventbox” (Purple in Fig. 3.1d) was also required to resolve the turbulent jet emanating from the central vent in the scoop. The resulting two-dimensional grid systems consisted of approximately 1.87×10^5 vertices for the 2D cylinder and 3.22×10^5 for the 2D scoop, a two-fold increase due to the complexity of the scoop’s small features like the gaps as well as the additional overlap created by the vent and body boxes.

Additional complexity was required to generate the revolved, three-dimensional scoop grid, as the small size of the interior vent prevented the upper body grid from growing any larger than half of the vent width. Large grid extension from the surface like that of the 2D grids would cause the upper surface of the 3D grid to intersect itself on the interior of its toroidal shape, which is problematic for overset grid interpolation. This was compensated for by splitting the portion of the scoop geometry above the porosity gap into two pieces: an upper “vent” portion, with small near-body extension, and a lower “body” portion with large extension. This system is visualized in Fig. 3.2, where the “vent” portion of the upper body grid is Light Blue, the “body” portion of the upper body grid is Red, the lower body portion is Dark Blue, and the boxes are of the same color scheme as the 2D grid systems.

The resulting size of these various grid systems are summarized below in Table 3.2. The final 2D grid for the scoop was approximately twice as large as that of the 2D cylinder due to its relative geometric complexity and overlapping bodybox. A nonmoving CFD simulation with the 2D

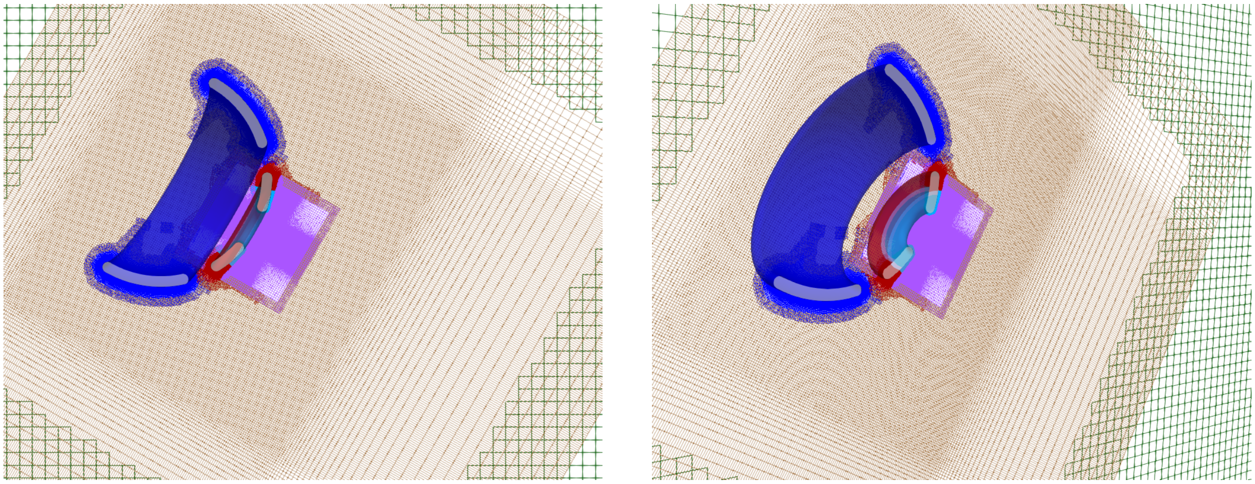

(a) $y = 0$ slice showing split upper body surface with minimal/large extension of its respective Light Blue/Red halves

(b) Isometric view showing gap and vent sizing and shape in three dimensions

Figure 3.2: Three-dimensional "scoop" simple parachute-analog grid system, with split upper body to prevent self-overlap of the torus grid

scoop grid could be completed on eight processors in a few hours, while moving-body runs took significantly longer, as many more iterations were required to collect multiple periods of oscillation of the pendulum. The 3D scoop grid system presented a significant increase in size of almost two orders of magnitude. These moving-body simulations required upwards of 200 000 iterations and more than 200 000 CPU hours, which took over one month of walltime on 480 cores to complete. Grid systems for the Orion parachute half-body were even larger than the 3D scoop (by a factor of 5) but consumed a similar amount of computational resources due to the simpler motion track and relaxed convergence settings for those prescribed motion runs.

Table 3.2: Grid system sizes and CPU hours to completion for various moving-body simulations

Mesh	Vertices	CPU Hours
2D cylinder	187k	0.5-1.5k
2D scoop	322k	1-2.5k
3D scoop	22.9M	150-250k
Orion parachute	100M	134k

Grid Size Sensitivity

Grid resolution and sizing was determined by a series of studies, detailed in this section, where sensitivity was assessed by observing changes to the averaged integrated aerodynamic loads in stationary geometry simulations and also changes in the Aero6DOF motion trajectory solutions, when appropriate. Studied mesh parameters included the wall spacing size, angular and radial resolution and extension size of the near-body grids, and resolution of the wake capturing box (incremental improvements of which are visible in the reduction in size from Fig. 3.1a to Fig. 3.1c).

First, the wall spacing (Δs_w) of the body grids was determined in order to accurately resolve the physics of the boundary layer. Initial Δs_w was determined from the freestream flow conditions and reference length according to the y^+ relation and criterion

$$\Delta s_w = \frac{y^+ \mu_w}{u_\tau \rho_w};\ y^+ \leq 1 \tag{3.9}$$

where the wall viscosity (μ_w) and wall density (ρ_w) are assumed to be equal to the freestream values for incompressible flow and the friction velocity (u_τ) accounts for the wall shear stress (τ_w) according to the relations

$$u_\tau = \sqrt{\frac{\tau_w}{\rho_w}};\ \tau_w = \frac{C_f \rho_w U_\infty^2}{2};\ C_f = \frac{0.026}{Re_x^{\frac{1}{7}}};\ Re_x = \frac{\rho U_\infty L}{\mu} \tag{3.10}$$

which allow the expression of Eqn. 3.9 in terms of reference parameters as

$$\begin{gathered} \Delta s_w = \frac{y^+ \mu_\infty}{\sqrt{\frac{0.026 \rho_\infty U_\infty^2}{2 \rho_\infty Re^{\frac{1}{7}}}} \rho_\infty} = \frac{y^+}{\sqrt{0.013} Re_x^{-\frac{1}{14}}} \frac{\mu_\infty}{U_\infty \rho_\infty} = \frac{y^+ L}{0.114018 Re_x^{-\frac{1}{14}} Re_x} \\ \boxed{\Delta s_w = \frac{y^+ L}{0.114018 Re_x^{\frac{13}{14}}}} \end{gathered} \tag{3.11}$$

Using the result of this calculation as the baseline wall spacing, additional simulations were run with varied wall spacing to determine any sensitivity to this parameter. Local y^+ was also measured in each simulation to ensure that the wall spacing criteria was met in actuality at all locations on the surface. It was found that a too-small wall spacing negatively affected convergence and produced non-oscillatory motion, so the largest y^+ that was appropriately suited to the solver time settings was chosen for all following simulations. This corresponded to $y^+ = 0.75$ or $\Delta s_w = 1.23 \times 10^{-3} in$ for the 2D cylinder and scoop and $y^+ = 0.1$ or $\Delta s_w = 1.64 \times 10^{-4} in$ for the 3D geometries.

Next, the appropriate cell resolution of the near-body grids was determined by successively decreasing the angular and radial spacing. Independence of unsteady flow effects occurred for a angular spacing of 2° and radial stretching ratio of 1.1. This was followed by a study of the extension of the near-body grids, which provide fine resolution for resolving turbulent features. It was found that extending near-body mesh made the final swing oscillations more symmetric, and an ideal extension from the surface of the $D = 10.5in$ cylinder was found to be $39.375in$ or approximately four times the reference length.

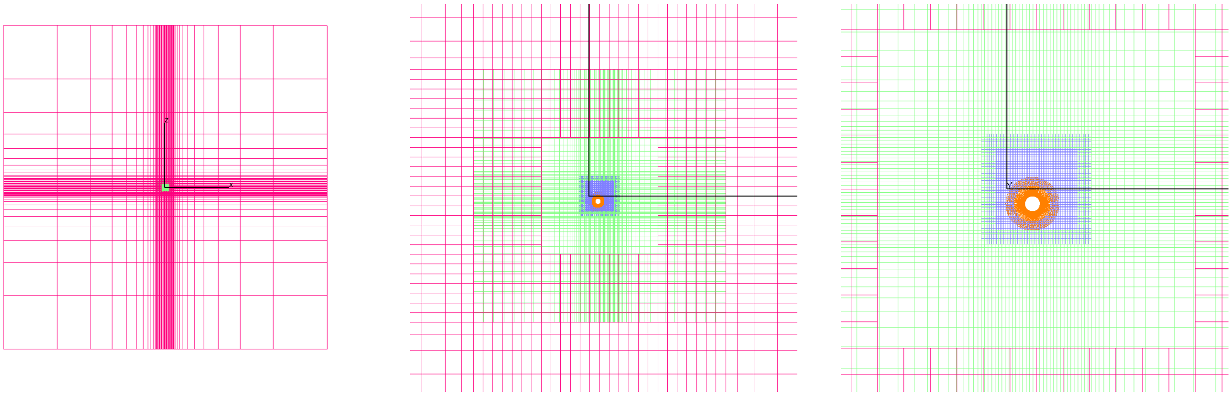

(a) Farbox (Pink) **(b)** Midbox (Green) **(c)** Wakebox (Purple): baseline

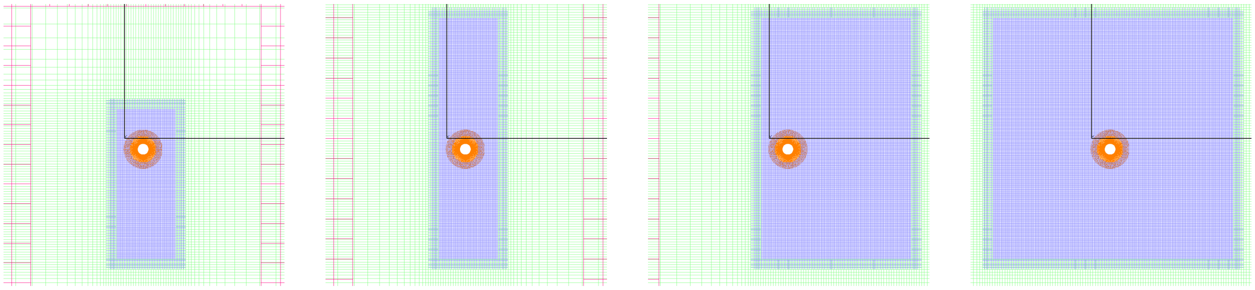

(d) Baseline extended in swing direction **(e)** Symmetric extension in swing direction **(f)** Additionally extended downstream **(g)** Additionally extended upstream

Figure 3.3: Sensitivity studies of the extension and resolution of the wake-capturing off-body, Cartesian box grid, where Z is vertical, and X is horizontal and positive to the right

Then, with sufficient sizing of the near-body grid achieved, the accuracy of bluff-body wake capturing was assessed by varying the size and resolution of the off-body wakebox. As depicted in Fig. 3.3, the wakebox was incrementally extended in all directions and then its resolution was increased. Initial size of the wakebox was a square, centered about the $\theta = 0°$ position of the pendulum, extending equally from that point in all four directions to a distance equal to the Z-extent of the initial pendulum swing plus 2.5 cylinder diameters of buffer overlap region so that the pendulum bob would be entirely encompassed by the wakebox throughout its trajectory. It was determined that extension of the wakebox in the Z-direction (perpendicular to the freestream) beyond the initial amount had little effect on the average C_X (drag) magnitude. Conversely, it was found that a total extension of the wakebox up to 4 cylinder diameters upstream and 9 diameters downstream significantly affected C_X but had diminishing effect above that size. Increased grid resolution of the wakebox had a significant effect on resolution of turbulent structures contributing to both base drag and side force, and consistency in the loads was achieved with a constant wakebox spacing of $0.67in$ ($0.064L_{ref}$).

Finally, the comparability of three alternative grid connectivity methodologies: extended near-body grid only, stunted near-body with overlapping bodybox, and mixed-mode PEGASUS 5/DCF instead of traditional DCF was demonstrated by simulating all three grid systems with the same solver settings and observing that the Aero6DOF motion track solution for a 2D cylinder is nearly identical for all methods.

The grid best practices resulting from the studies in this section are summarized in Table 3.3.

Table 3.3: Summary of best practices for aerodynamic pendulum overset grid construction

Body diameter	$L_{ref} = D = 10.5in$
Pendulum swing radius	$R = 20.5in$
Wall spacing (2D)	$y^+ = 0.75, \Delta s_w = 1.23 \times 10^{-3}in$
Wall spacing (3D)	$y^+ = 0.1, \Delta s_w = 1.64 \times 10^{-4}in$
Angular spacing	$\Delta s_\theta = 2°$
Radial stretching ratio	$sr = 1.1$
Radial extension of near-body (or bodybox)	$z_{reg} = 4D$
Wakebox X-width up, downstream	$4D, 9D$
Wakebox Z-height	$2 \times (2.5D + R\cos\theta_{max})$
Wakebox uniform spacing	$0.67in$

3.2.3 Solver Sensitivity Studies

A high-order, time-accurate solver was required for this work, as solutions for both bluff-body flows and moving-body simulations are generally unsteady and the nonlinear coupling of the flow solver with the grid motion solver requires high accuracy for stability and realism. Time was advanced implicitly using Symmetric Successive Over-Relaxation (SSOR), with multiple Newton sub-iterations at each time step to improve convergence [77], and the Riemann HLLC upwind inviscid flux scheme, which employs the 5th-order spatially-accurate WENO scheme [78].

CFD solutions were completed following a two-stage convergence procedure. First, the flow was initialized with the pendulum held stationary at the maximum swing angle (θ_{max}). Stationary-position, quasi-steady flow was successively converged with full-multigrid, steady-state convergence, then unsteady, time-accurate convergence, first at a large time step to more rapidly propagate spurious transients downstream, and then at the desired time step to accurately resolve the unsteady flow solution. Stable and accurate motion predictions were facilitated by employing small time steps with a significant number of Newton sub-iterations (20) to allow for maximum flow convergence at a given location before computation of coupled body motion. Once a steady or quasi-steady stationary solution was obtained, pendulum motion was initiated. Ensuing, aerodynamically-driven grid motion was allowed to run out to completion, which typically corresponded to a damped quasi-steady end state, a periodic stable limit cycle oscillation, or an unstable divergence. This convergence procedure and the best practices necessary for acceptable solver convergence were determined through a series of sensitivity studies that are described in the following sections.

Time Sensitivity

The physical time step (DTPHYS) was determined by successively decreasing the step size until the behavior of the Aero6DOF motion became independent of this change. DTPHYS was parametrically varied with the number of sub-iterations (NITNWT) and the CFL number range in order to achieve desirable residual convergence of at least 3 orders of magnitude. Time independence and residual convergence of a total of 7 orders of magnitude (with 3 orders of magnitude gain from sub-iteration) was achieved with DTPHYS=0.01, NITNWT$>$10, and CFL=1-5.

Solver Settings Sensitivity

Aero6DOF runs require very high-order accuracy to capture the nonlinear coupling of turbulent flow with constrained body motion and are, thus, very sensitive to solver settings that affect the order of accuracy. An extensive parametric study of various solver settings was performed in order select the combination that produced:

- Good convergence performance
- Simulation aerodynamic loads most similar to experimental cylinder drag
- An Aero6DOF motion solution insensitive to variations in solver parameters

As a result of this study, the following best-practice solver settings were chosen:

- ILHS=6: Time advanced implicitly with SSOR
- IRHS=5: Spatial domain solved with HLLC upwind scheme
- FSO=5: 6th-order-accurate spatial differencing of Euler terms with 6/2 dissipation
- FSOT=3: 3rd-order differencing of turbulence convection terms

Tubulence Model

All simulations for the simple, aerodynamic pendulum utilized URANS turbulence modeling, but the sensitivity to the model of choice was investigated by comparing simulations run with the one-equation Spalart-Allmaras (SA) [79] and the two-equation Shear Stress Transport (SST) [80] turbulence models. Little difference between models was found at high, full-turbulent Reynolds number, but significant difference in boundary layer transition modeling and base pressure was noticed at the transitional $Re = 1e6$. Though SA predicted a more correct base pressure at transitional Reynolds number (Re) and, thus, had a C_d slightly more similar to experimental values, SST was superior at predicting boundary layer transition and the resulting unsteady cylinder shoulder pressure distribution, as shown in Fig. 3.4a, which has a critical effect on the dynamic stability of a moving-body simulation. For this reason, it was determined that SST provided results that were more realistic and better suited for Aero6DOF-mode.

3.3 Model Calibration

The previous section established best practices for well-converged, aerodynamically-driven, moving-mesh simulations. This section describes the tuning of the aeropendulum model to specific test conditions for validation purposes. Physically accurate bluff-body flow modeling was confirmed by comparison of stationary cylinder OVERFLOW CFD results to wind tunnel experiments and other CFD solvers. Then, the functionality of OVERFLOW's Aero6DOF-mode was assessed through qualitative observation of simply constrained geometries in crossflow.

3.3.1 Unsteady Flow Solver Calibration

Averaged Aerodynamic Loads

Averaged surface pressure distribution and integrated aerodynamic loads of the OVERFLOW CFD simulation of a stationary cylinder were compared to empirical measurements by Roshko (1961) [63] at the fully-turbulent $Re = 8.4e6$ and to results by Achenbach (1968) [81] at transitional and laminar Re.

As shown Fig. 3.4a, the CFD simulation (at high Reynolds number) correctly predicts the averaged surface pressure coefficient distribution and, thus, the distributed surface aerodynamics, which is important for accurately modeling the dynamic stability of a pendulum. The figure shows that the CFD simulation recovers both the base and shoulder pressures accurately, indicating that the boundary layer is fully-turbulent, as expected, and that the boundary layer separation location is predicted accurately. Integration of the pressure distributions yields reasonably comparable average drag coefficients of $C_d = 0.709/0.722$ for the simulation and experiment, respectively (18 %-difference).

Figure 3.4b, which compares averaged drag coefficient as a function of freestream Re, also demonstrates accurate simulation of cylinder integrated aerodynamic loads compared to experiment for multiple Re in the fully-turbulent and transcritical range ($Re > 3.5e6$). The CFD simulation is less accurate at laminar and supercritical $Re \sim 1e6$, which demonstrates a common limitation of Reynolds-averaged Navier-Stokes (RANS) turbulence modeling. As observed in Section 3.2.3, the SA turbulence model may be better suited for simulations in this regime, but since the analogous parachute flow is at a very high Re, the current simulation settings and accuracy above $Re > 3.5e6$ was deemed sufficient for the cases in this work.

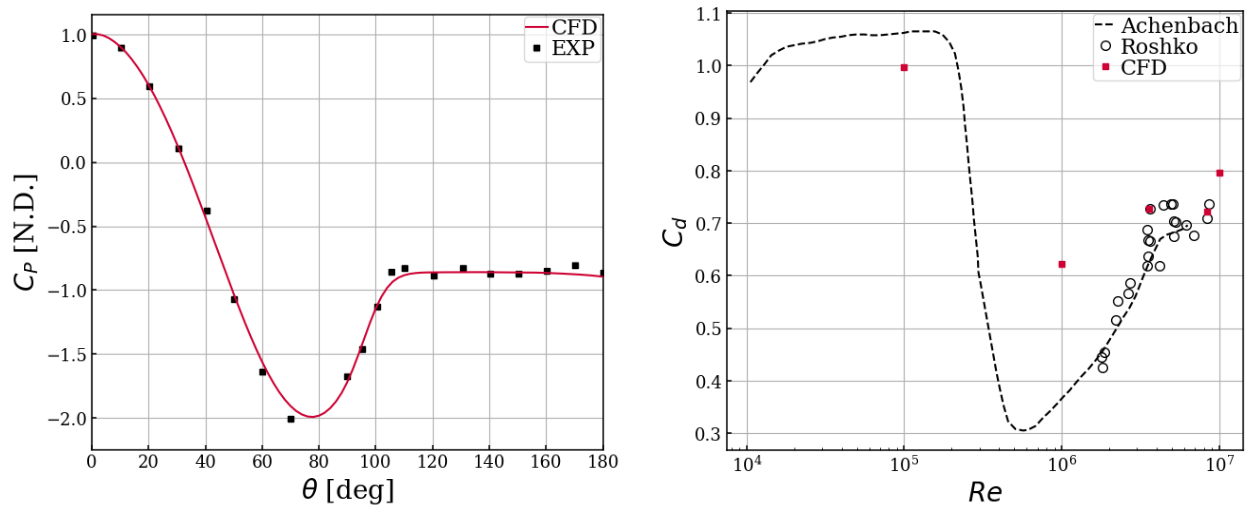

(a) Surface pressure coefficient (C_P) compared to experiment ($Re_D = 8.4e6$)

(b) Drag coefficient as function of freestream Re

Figure 3.4: OVERFLOW URANS CFD solutions for a stationary cylinder showing reasonable comparison to wind tunnel results at high Reynolds number [63, 81]

Unsteady Wake

In addition to accurately modeling the averaged aerodynamics, the performance of OVERFLOW URANS at capturing unsteady, bluff-body effects also compared well to the examples from the literature. Unsteadiness of the vortex shedding in the wake was quantified using the Strouhal number (St),

$$St = \frac{fL}{U}, \tag{3.12}$$

and showed good comparison to Roshko's experimental results ($St = 0.26/0.27$ for simulation/experiment and $3.4\,\%$-difference).

OVERFLOW's resolution of fine turbulent features in the wake also compares well qualitatively to other URANS simulations in the literature. Figure 3.5 shows a comparison of the wake vorticity between the OVERFLOW SST solution and another CFD simulation using a k-ϵ turbulence model [55], where the magnitude of vorticity in the wake and number of contours in each vortex are comparable, and the separated shear layers on either side of the cylinder are of similar lengths and thicknesses. The spacing of the wake vortices is also similar, though the OVERFLOW solution exhibits a slightly lower frequency than that of the other simulation.

The comparisons in these sections demonstrate that the OVERFLOW URANS CFD simulation is acceptably accurate and realistic for the purposes of modeling aerodynamically-driven motion of a constrained bluff-body.

(a) OVERFLOW URANS SST

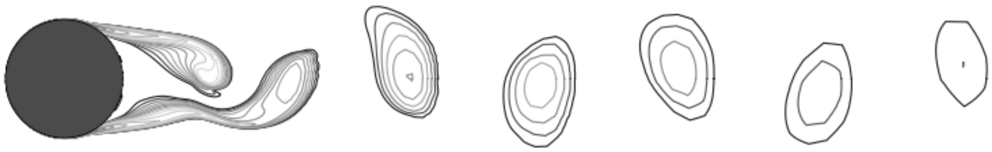

(b) FLUENT URANS k-ϵ [55]

Figure 3.5: Instantaneous wake vorticity for a static, 2D cylinder ($Re_D = 1e6$) with vorticity contours: $\omega D/U_\infty = $ 1-575, 25 levels

3.3.2 Aero6DOF-Mode Constrained Motion Calibration

As a first-order check on the functionality and sensitivity of Aero6DOF motion in OVERFLOW, a variety of aerodynamic bodies other than the cylinder and scoop were also simulated as tethered pendulums. The notional dynamic behavior of these asymmetric geometries was observed to confirm intuitive motion behavior and build confidence in the coupled fluid dynamics and motion solution. This exercise also helped in the tuning of the inertial properties required for stable pendulum motion at the flow conditions of the cylinder/scoop experiments.

Flat Plate

The first geometry tested was the most simple representation of a pendulum: a flat plate pinned at the leading edge. The actual geometry was designed with finite thickness and rounded leading and trailing edges to facilitate the grid generation task and improve the flow solution. Motion constraints were set to pin the plate about the center of the radius of curvature of the leading edge, and the plate was given a “medium” nondimensional moment of inertia (1×10^5) with a center of mass located at the trailing edge.

Simulations were run starting with the geometry stationary at a non-zero angle of attack (α), shown in Fig. 3.6a. After stationary solution convergence was achieved, the pendulum was released.

As expected, the plate behaved similarly to a weathervane and immediately reoriented itself with the direction of the freestream flow (Fig. 3.6b). The end-state motion was quasi-steady, with a minor oscillation about the leading edge, and the resulting flow was the typical mixing of the two shear layers shed by the flat plate at $\alpha = 0°$.

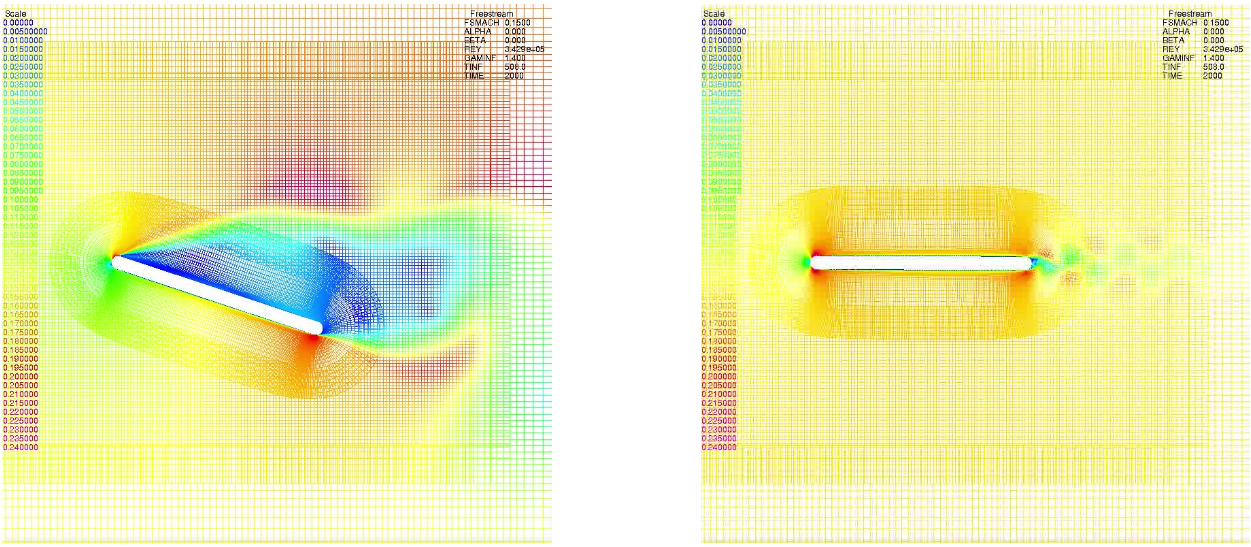

(a) Starting angle

(b) Quasi-steady trim angle

Figure 3.6: Instantaneous Mach number contours surrounding a flat plate, pinned at the leading edge, exhibiting weathervane motion ($Re = 1e6$)

Cylinder with Tab

Another initial functionality test involved a simple, centroid-pinned constraint. The geometry was a cylinder made asymmetric with a triangular tab, which conforms to the same Outer Mold Line (OML) as the Human/Vehicle/Robotic Integration and Performance (HRVIP) lab logo. The tab was assumed to be mass-less and did not adjust the center of mass of the body from the center of the circle. The motivation was to demonstrate motion damping with an asymmetric geometry.

When released, the cylinder trimmed such that tab would be inside of the separated wake and not impinged by the high-momentum shear layer from the cylinder's separated boundary layer. For this specific geometry and starting orientation, this motion was minimal, as the tab was already mostly inside the separated wake. Once contained within the wake, and with no specified mass to drive a centerline trim, the tab remained in the position shown in Fig. 3.7a and was buffeted slightly back and forth by the separated shear layer. This test confirmed intuitive dynamic responses to unsteady flow stimuli.

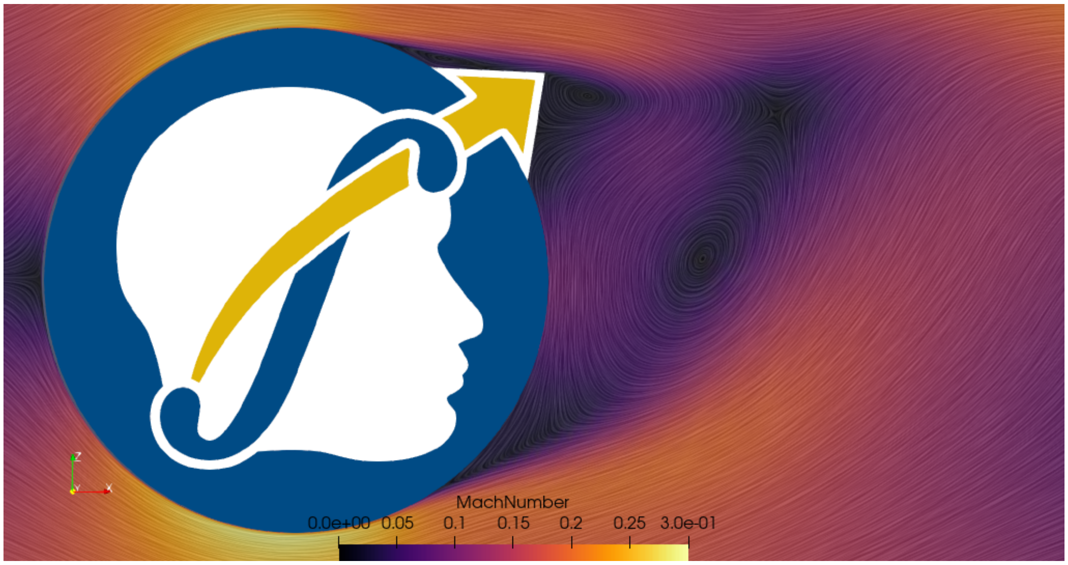

(a) Instantaneous streamlines surrounding the pinned, dynamic HRVIP logo

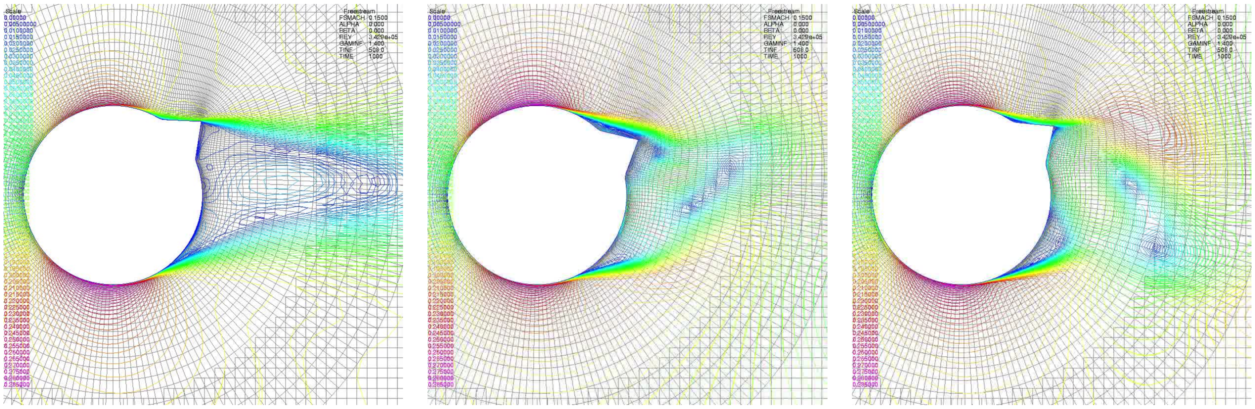

(b) At starting angle **(c)** Tab inside wake separation region **(d)** Long-term, quasi-steady angle

Figure 3.7: Instantaneous Mach number contours over the Human/Vehicle/Robotic Integration and Performance (HRVIP) logo/cylinder with tab, pinned at the centroid ($Re = 1e6$)

Half-Cylinder Pendulums

Finally, an asymmetric, half-cylinder was tested at two separate orientations. Figs. 3.8a and 3.8c show the starting conditions of "feathered" and face-normal orientations, respectively. These orientations were rigidly fixed to track the origin angularly in order to satisfy the same pendulum constraint as all other pendulum simulations. Center of mass and tether pin location were set to be the center of the full circle, for simplicity.

Each pendulum was set at an initial non-zero tether angle and, when released, traveled to a trim point, as expected for an asymmetric geometry. The feathered cylinder was already oriented such as to incur a near-minimal pitching moment, and its transient motion was simply to move

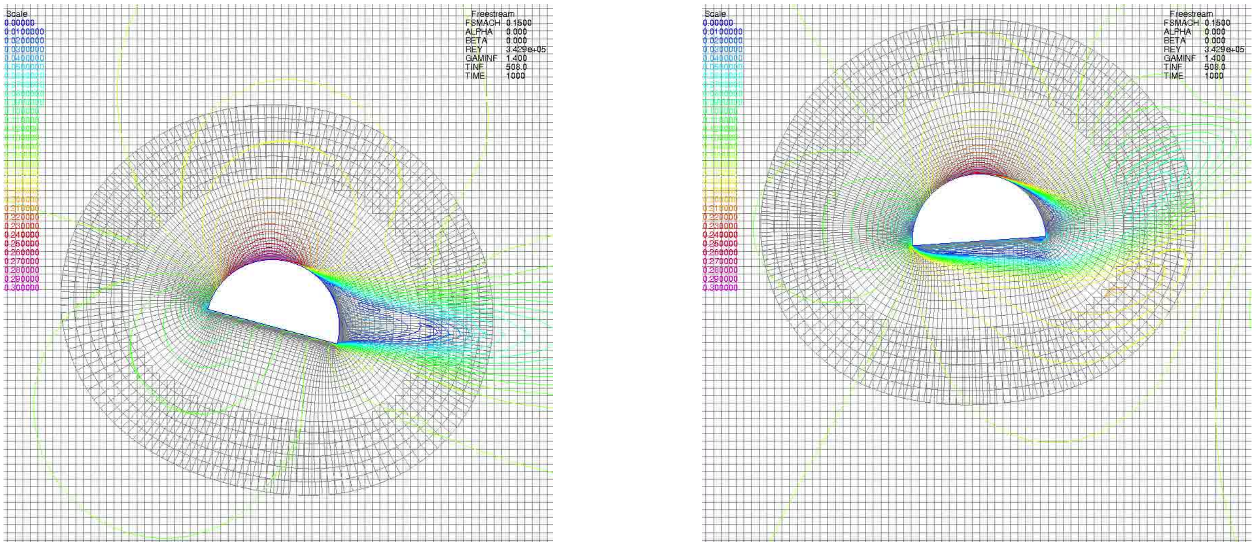

(a) Feathered, starting angle

(b) Feathered, quasi-steady trim angle

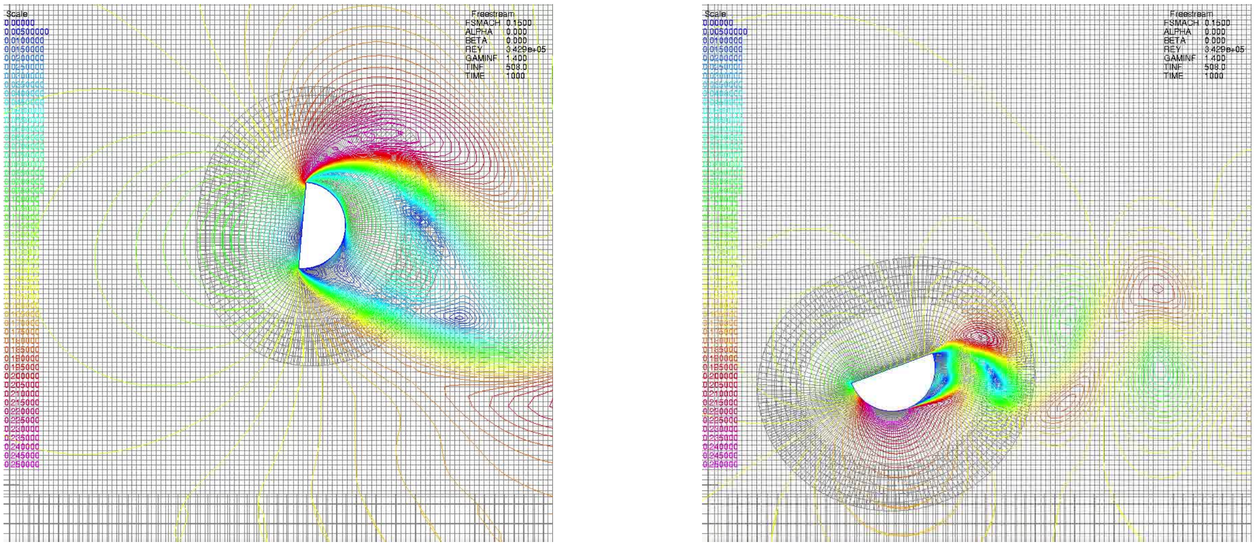

(c) Normal-facing, starting angle

(d) Normal-facing, quasi-steady trim angle

Figure 3.8: Instantaneous Mach number contours over tethered, half-cylinder, aerodynamic pendulums ($Re = 1e6$)

nearer the centerline (Fig. 3.8b). Its quasi-steady motion involved a small, periodic oscillation asymmetrically balanced around the centerline, due the the asymmetric pin location of the rigid tether and the asymmetric geometry of the aerodynamic body.

The face-normal cylinder, similarly, sought to reduce its induced pitching moment by minimizing its frontal area as seen by the incoming flow. Due to the rigid tether constraint on both the cylinder's angular position and its normal-facing orientation to the tether, the resulting end trim position was one of relatively large swing angle (Fig. 3.8d). Though seemingly counterintuitive, this position represents a static balance between the aerodynamic moment torquing the rigid pendulum clockwise about the tether and the aerodynamic drag pushing the pendulum counterclockwise. All of the simple pendulum geometries in this section exhibited intuitive dynamic responses, lending confidence to the functionality of motion constraint implementations in OVERFLOW Aero6DOF-mode.

3.4 Model Validation: Cylinder Aeropendulum

The goal of this work is to develop a model that provides accurate prediction of the motion of aerodynamically-driven, pendulum-like systems. This section showcases the results produced by the calibrated CFD and demonstrates its utility for engineering design purposes such as dynamic stability analysis. It also presents validation of accurate functionality by comparison of the moving-body results to the numeric, drag-based pendulum model developed for this purpose.

3.4.1 Simulation Results

Motion and Dynamics

The trajectory of the OVERFLOW GMP Aero6DOF-mode cylindrical pendulum, defined by the pitch/swing angle (θ), is traced in the upper plot of Fig. 3.9a along with the instantaneous total pendulum moment coefficient ($\Sigma C_{M,Y_i}$), and the body-reference-frame force coefficients are co-plotted below. The motion of the cylinder aeropendulum is a damped oscillation driven by the freestream drag force and damped by the tangential drag force, which is the behavior expected by theory for a pendulum with non-zero air resistance. The frequency of this primary swinging motion can be inferred to be approximately $3Hz$ from the fast Fourier transform (FFT) Power Spectral Density (PSD) analysis in Fig 3.9b. The CFD cylinder aeropendulum motion is additionally subject to a secondary oscillation of approximately $48.2Hz$, which is due to the influence of and proportional to the frequency of the unsteady, oscillating wake.

The effective angle of attack (α_{eff}) is dynamically affected by the motion of the pendulum. Its sign and magnitude are closely tied to θ, as the effective velocity (V_{eff}) of the pendulum is majorly derived from the freestream velocity, and, thus, α_{eff} is proportional the orientation of the pendulum to the freestream. However, due to the additional component of tangential swing velocity, α_{eff} generally lags θ in time and experiences larger-magnitude, secondary fluctuations due to the influence of the unsteady wake on local field velocity.

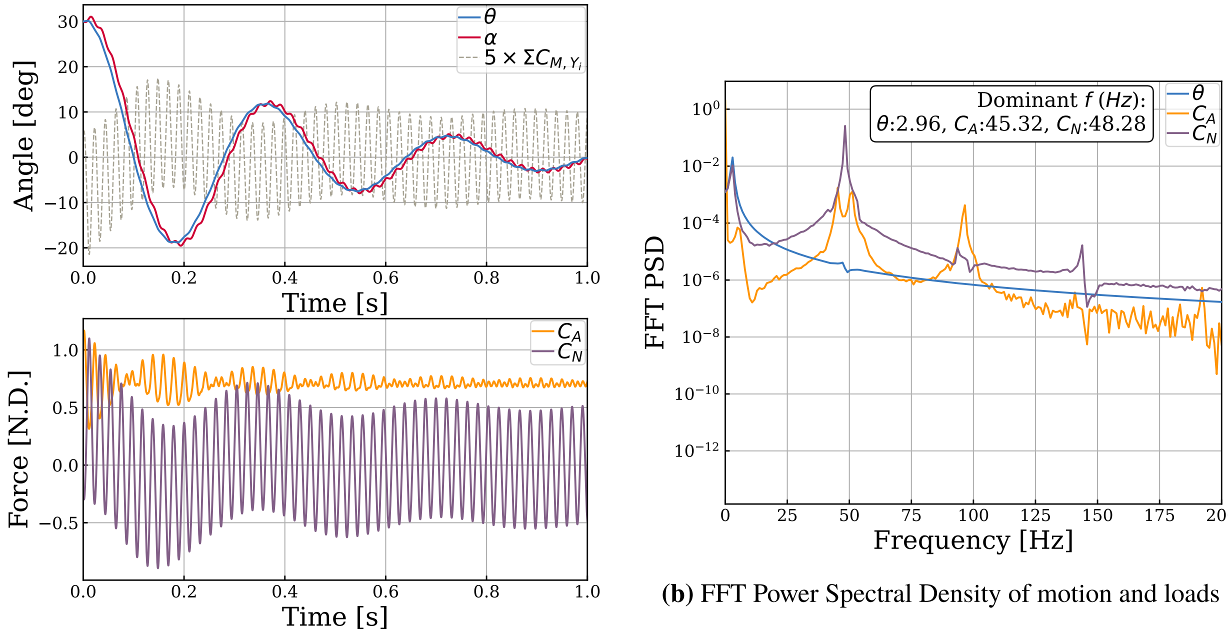

(a) Motion and loads time history

(b) FFT Power Spectral Density of motion and loads

Figure 3.9: Time histories and FFTs of motion trajectories and aerodynamic loads for a CFD-simulated, aerodynamically-driven, swinging, 2D cylinder, with parameters including pendulum pitch/swing angle (θ), effective angle of attack (α_{eff}), total pendulum moment coefficient ($\Sigma C_{M,Y_i}$), and axial/normal force coefficients (C_A/C_N)

Unsteady Aerodynamic Loads

The direct drivers of the primary and secondary modes of pendulum motion are the oscillating axial/drag force on the cylinder, time-histories of which are co-plotted in Fig. 3.9a. Both axial force coefficient (C_A) and normal force coefficient (C_N) oscillate at the same high secondary frequency as that of the motion and vortex shedding of the wake (approximately $48.2Hz$). Multiple harmonics of this fundamental tone are also present in the unsteady aerodynamic loads ($\approx 100Hz, 150Hz$). The aerodynamic loads are additionally modulated at a low frequency by the swinging motion of the pendulum; an effect that diminishes as the amplitude of the pendulum is reduced by aerodynamic dampening. The average value of C_A is non-zero and initially oscillates at a frequency of approximately $6Hz$, or twice that of the cylinder motion. This doubling is due to the fact that C_A magnitude is proportional to the alignment of the pendulum body axis with the incoming flow, which cycles twice in a single period of the pendulum swing. As pendulum motion damps towards a quasi-steady state, C_A approaches a constant averaged value of ≈ 0.7, which is the expected value for drag of a turbulent cylinder in crossflow [63].

C_N and $\Sigma C_{M,Y_i}$,

$$\Sigma C_{M,Y_i} = C_{m,i} + \frac{z_{cg}C_{X,i} + -x_{cg}C_{Z,i}}{L_{ref}} \tag{3.13}$$

the sum of all moment contributions about the inertial y-axis depicted in Fig. 2.1, which is also the tether point, are symmetric about the origin. These parameters are also modulated at the same frequency as the pendulum motion, as they are sensitive to relative motion in the tangential swing direction, which is proportional to the sign of the rate of pendulum swing, which reverses only one time per swing period. $\Sigma C_{M,Y_i}$ is the direct driver of the pendulum restoring force and is, thus, inversely proportional to θ.

Unsteady Flow

The swing of the cylinder aeropendulum from maximum-to-minimum amplitude during the time interval $t = 0\text{-}0.2s$ (where $t = 0s$ is when the pendulum is released from its stationary, θ_{max}) is visualized in Fig. 3.10, which illustrates the surrounding unsteady flowfield in terms of Mach number (M) contours and momentum streamlines. In the figure, time (t) advances chronologically from left-to-right, then top-to-bottom. The full arc of the pendulum's trajectory is divided equally into five angular locations: positive and negative θ_{max}, centerline ($\theta = 0$), and the midpoints between. Each row of the figure represents a short time interval that begins at one of these locations. Thus, short-term, bluff-body flow unsteadiness can be observed across each row (with a frame interval of $\Delta t = 4ms$) and long-term unsteadiness due to motion can be observed down each column (with a frame interval of $\Delta t \approx 40ms$).

Comparing each row, the general appearance and variation of the wake is similar for any given short-term interval. This suggests that, for these spectrally-disparate fundamental frequencies, the unsteady, nonmoving solution is essentially superimposed upon the motion of the cylinder and is slightly augmented by the motion, as is especially apparent in Fig. 3.10g, where the wake is angled away from the centerline due to the relative swing velocity of the pendulum.

The dynamic solution in Fig 3.10g is also directly compared to its stationary equivalent in terms of field C_P and momentum streamlines in Fig. 3.11. Both the stationary and moving-body simulations exhibit strong unsteadiness due to vortex shedding in the bluff-body wake, which is visible in the momentum streamlines and field C_P contours of Fig. 3.11 as a Kármán vortex street; the expected result for a stationary cylinder in crossflow. The frequency of vortex shedding is the same as that of the secondary oscillation of the pendulum motion (approximately $48.2Hz$), as this shedding

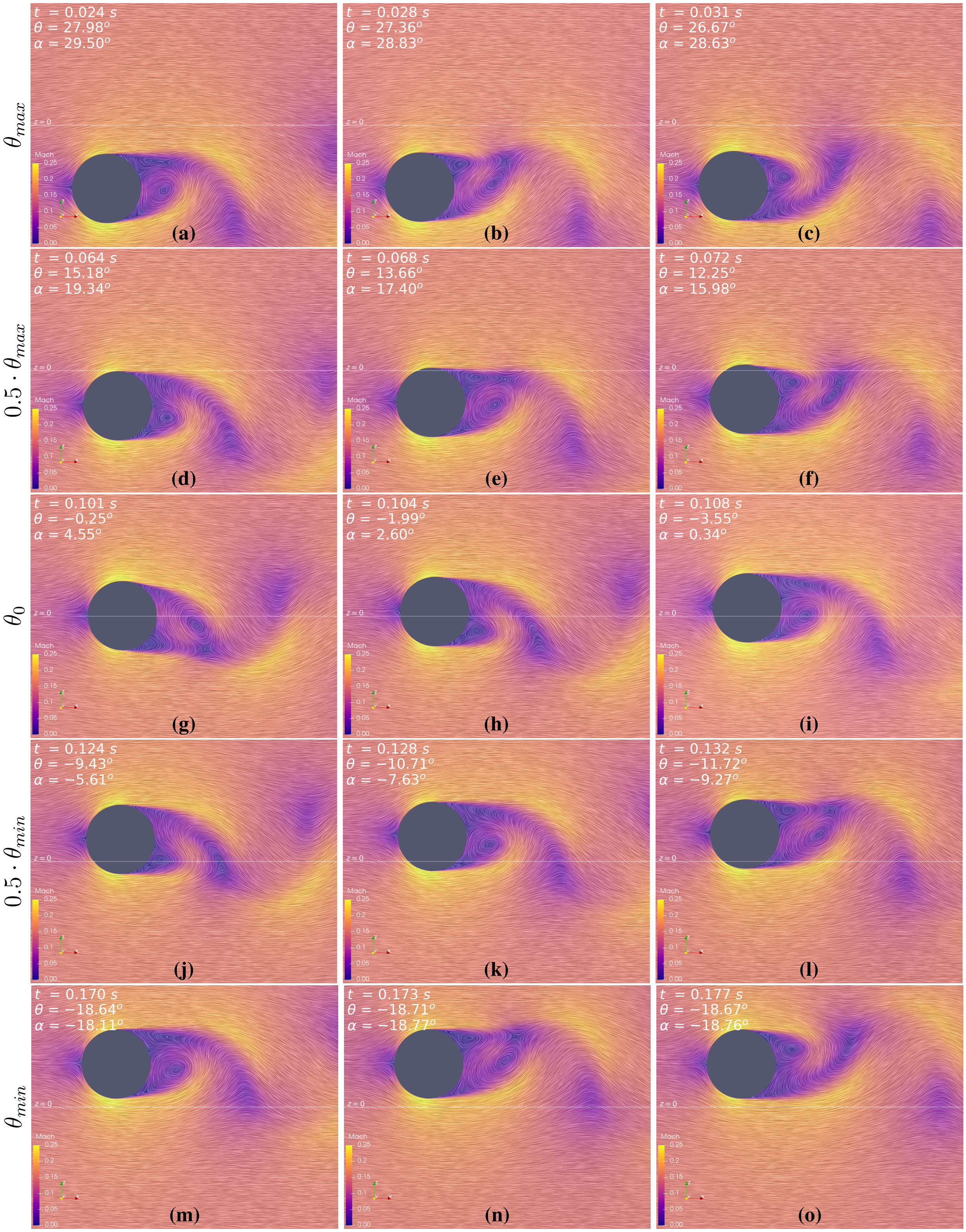

Figure 3.10: Chronologically-ordered, instantaneous frames of unsteady, flowfield Mach number contours and momentum streamlines surrounding a 2D cylinder aerodynamic pendulum swinging counterclockwise from maximum to minimum amplitude ($Re = 8.4e6$)

is the direct driver of that motion. There is no significant difference in vortex shedding frequency between stationary and moving pendulum systems. The non-zero angle that the vortex street makes with the centerline in the moving solution in Fig. 3.11b compared to the stationary, symmetric wake in Fig. 3.11a is indicative of the tangential drag force component that opposes the swing of the pendulum, reducing its momentum and damping its oscillation.

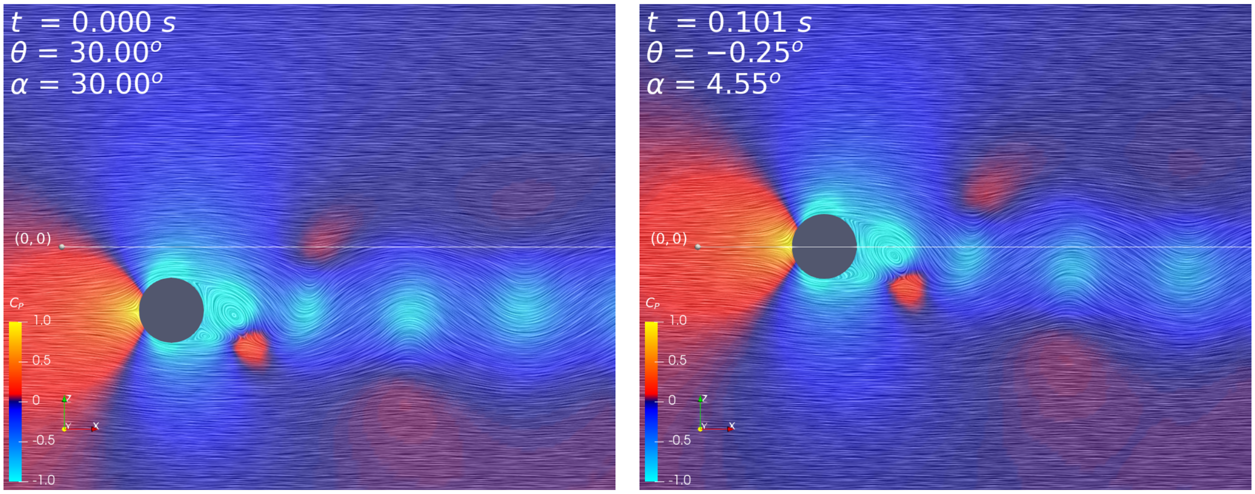

(a) Stationary cylinder ($\alpha = 0°, \theta = 30°$)

(b) Swinging cylinder ($\alpha = 4.55°, \theta = 0°$)

Figure 3.11: Instantaneous flowfield pressure coefficient (C_P) contours and momentum streamlines for a stationary and moving cylinder aerodynamic pendulum ($Re = 8.4e6$)

3.4.2 Comparison to Drag-Based, Numeric Model

This section validates the accuracy of aerodynamically-driven, coupled motion simulations in OVERFLOW that utilize off-body motion constraints by comparing the Computational Fluid Dynamics (CFD) cylinder aeropendulum from this section to the drag-based, numeric Ordinary Differential Equation (ODE) model derived in Chapter 2, as shown in Fig 3.12. The numeric validation model ("ODE") exhibits the same expected low-frequency, damped oscillation as the moving-body CFD solution ("CFD"), with a very similar primary swing frequency of approximately $3Hz$. This indicates that the averaged drag of the cylinder is the dominating driver of pendulum motion and that its effect is similar across both models. Unlike the OVERFLOW model, the swinging of the ODE aeropendulum model is not subject to a $48.2Hz$ secondary, high-frequency oscillation, as it does not model vortex shedding of the wake. This difference represents an increase in realism of the CFD model in terms of modeling the unsteady dynamics of an actual aerodynamic pendulum and is also likely related to the stronger damping of the CFD model compared to the ODE model, as the secondary accelerations of the pendulum are responsible for additional transfer of the body's momentum into internal energy of the flow through viscous interactions.

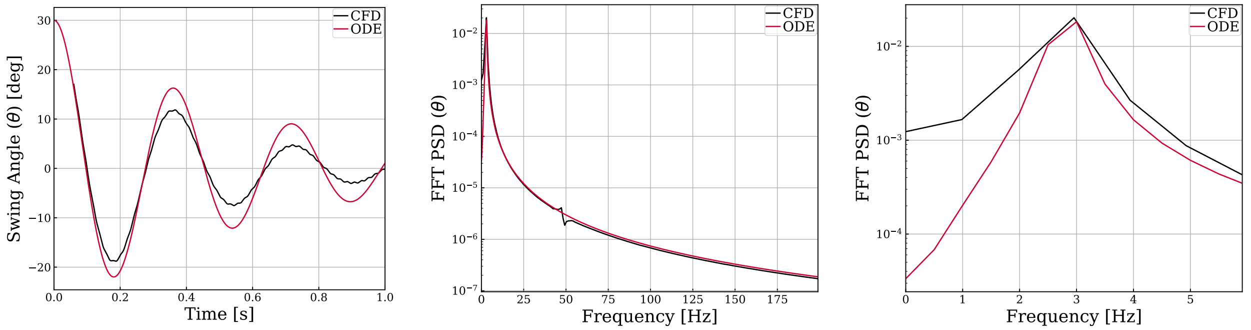

(a) Pendulum pitch/swing angle (θ) **(b)** θ FFT Power Spectral Density **(c)** θ fundamental frequency

Figure 3.12: Comparison of motion predictions by the OVERFLOW CFD pendulum and the drag-based, numeric ODE models of a 2D cylinder aerodynamic pendulum ($Re = 8.4e6$)

Overall, it can be concluded that OVERFLOW GMP's Aero6DOF-mode with off-body constraints is capable of producing realistic predictions of aerodynamically-driven motion. This assertion is validated by qualitative observation of the motion of the CFD model, which follows the expected behavior of an aerodynamically-driven pendulum with an unsteady wake as well as quantitative comparison with the simple, numeric ODE, drag model, which exhibits similar pendulum motion characteristics with explainable differences.

3.4.3 Aero6DOF vs Prescribed Motion

As explained in Section 2.3.2, OVERFLOW's GMP provides two modes of specifying relative grid motion: Aero6DOF-mode, aerodynamically-driven motion, as employed in the simulations described in this chapter and prescribed motion, where a user-defined fit-equation of a trajectory observed in a prior flight or wind tunnel test controls motion as a function of simulation time. In practice, prescribed motion is easier and more cost-effective to implement and analyze, but Aero6DOF is capable of simulating motion that is closer to reality. This section addresses the utility of prescribed motion simulation for applications like the Orion parachute and answers the question of whether the unsteady aerodynamic predictions of this simulation technique are fundamentally comparable to those of an Aero6DOF-mode simulation when an equivalent trajectory is prescribed.

The previous analysis in this chapter demonstrates that Aero6DOF-mode has a distinct advantage in its ability to predict the nature of previously unobserved, aerodynamically-driven motion. This capability is essential to the development process when there is no prior information about the dynamic nature of a potential design. However, for motion previously observed through other forms of testing, prescribed simulation can exact the most efficient emulation of that trajectory and reduces the overall demand for computational resource in the process. Therefore, it would be the CFD analyst's preference to employ prescribed motion whenever applicable, as long as it could be ensured that the realism and accuracy of the unsteady aerodynamic simulation would be comparable to that of an Aero6DOF run. The following example will demonstrate that prescribed motion is sufficient for realistic modeling moving-body aerodynamics when it is set to exactly follow a known motion track.

For the example demonstration, the damped θ oscillation of the 2D cylinder aeropendulum in Section 3.4 was fit by superimposing two sinusoids oscillating at the low and high dominant frequencies determined through FFT analysis, with the low-frequency function amplified by a decaying exponential. A cosine function was chosen for each fit because the oscillation commences at maximum amplitude. Least-squares minimization was used to determine the damping rate and appropriate amplitude of oscillation for each sinusoid, resulting in:

$$\theta(t) = 32.18e^{-2.75}\cos\left(2\pi\cdot 3t\right) + 0.2\cos\left(2\pi 48.2t\right) + 0 \tag{3.14}$$

where the offset is zero since the swing oscillation is symmetric. OVERFLOW GMP prescribes rotational movement as a rate, rather than a position, so the least-squares fit equation was differentiated with respect to time and then nondimensionalized for direct consumption by GMP through the input file `Scenario.xml`.

Figure 3.13a demonstrates the goodness of the motion fit by overlaying the motion tracks of the aerodynamically-driven ("6DOF") and prescribed motion ("EQN") CFD runs. The figure also shows good comparison between the unsteady aerodynamic loads predicted by the two methods. The lift and drag (proportional to C_N and C_A in the figure) of the prescribed motion simulation are both slightly greater in magnitude than that of Aero6DOF-mode, which may be due to an overestimation of the the secondary oscillation amplitude in the motion fit equation. This highlights a disadvantage of the prescribed motion technique: that it is only as accurate as the accuracy of the

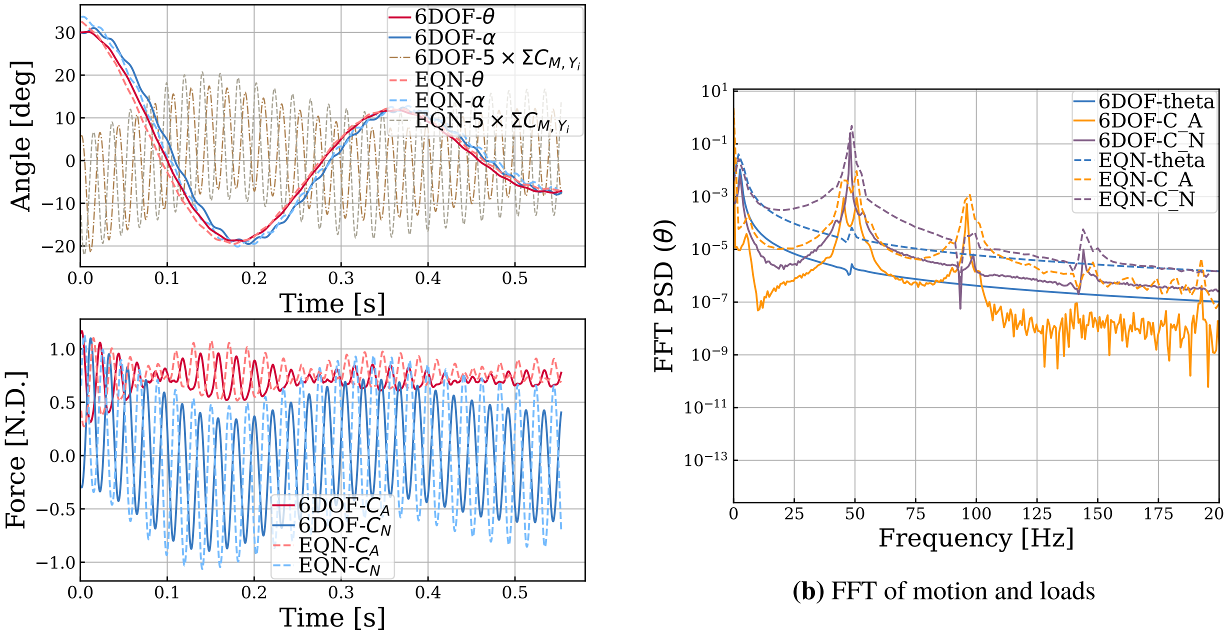

(a) Time history of motion and loads

(b) FFT of motion and loads

Figure 3.13: Comparisons between CFD simulation results for an aerodynamically-driven, 2D cylinder pendulum (“6DOF”) and an equivalent simulation of the same system (“EQN”) with motion prescribed to track the Aero6DOF-mode trajectory using a Least-Squares decaying exponential cosine fit

prescribed equation.

The frequency characteristics of the dynamic behavior of both simulations are notably similar, as especially apparent in the power spectral analysis of the motion and loads in Fig. 3.13b, where all dominant primary, secondary, and tertiary frequencies are all nearly identical. Good comparison of dynamic behavior is further apparent in Fig. 3.14, which represents the periodic, damping motion of the cylinder pendulums as an unstable limit cycle oscillation. Fig. 3.14a shows each simulation following a similar downward spiral towards a quasi-steady end state in rate of angle of attack ($\dot{\alpha}$)-α-space, which demonstrates dynamic similarity of the unsteady aerodynamics. Figures 3.14b and 3.14c, though noisy due to the oscillating wake, also show consistent overlap, indicating that the instantaneous dynamic loads in both simulations are comparable in aggregate.

This all shows that these two prescribed and Aero6DOF simulations are dynamically similar, and that prescribed motion may be effectively used to model the unsteady aerodynamics of a moving body with a previously-observed motion trajectory, while the more resource-intensive Aero6DOF-mode is required for analyzing untested designs.

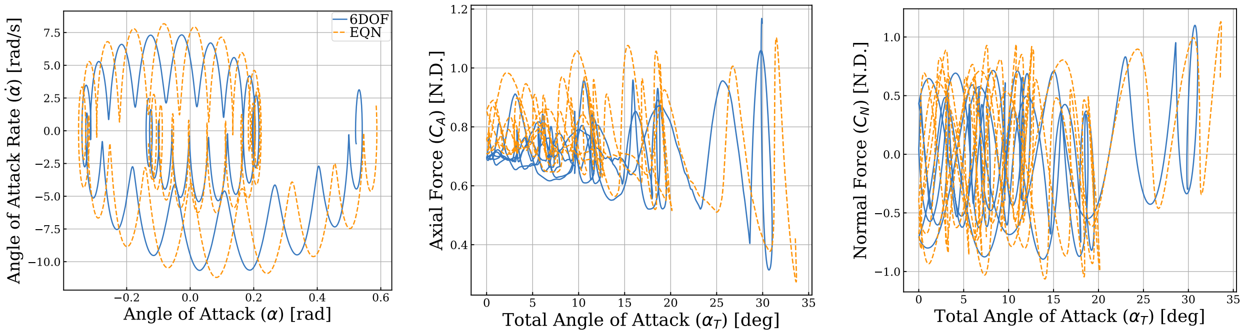

(a) Aerodynamic angle tracking **(b)** axial force coefficient (C_A) **(c)** normal force coefficient (C_N)

Figure 3.14: Trajectory comparisons between the aerodynamically-driven, 2D cylinder pendulum simulation and the equivalent-track prescribed motion run

3.5 Model Demonstration: Scoop Parachute-Analog

3.5.1 2D Scoop

After obtaining confirmation of the accuracy of the CFD aeropendulum model using the simple cylinder geometry, the capabilities of the model were leveraged to predict the motion and stability of a two-dimensional, simple parachute-analog or “scoop”. This case was run at the same reference length and freestream conditions as the cylinder aeropendulum in Section 3.4.1 for simplicity, as its freestream Reynolds number $Re = 8.4e6$ exhibited fully-turbulent boundary layer behavior like that expected for the actual parachute. Simulations were converged at the stationary angle $\theta = 15^\circ$ and then Aero6DOF-mode was initiated to release the pendulum. Good convergence was achieved for the moving simulation, with an initial residual convergence of 1×10^{-4} and an additional 2.25 orders of magnitude residual drop from 20 successive Newton sub-iterations.

Motion and Dynamics

The motion of the aerodynamically-driven, 2D scoop geometry considered for this analysis, plotted in Fig. 3.9a, is periodic in nature, unlike the damped motion of the cylinder. This does not necessitate that the geometry is inherently unstable, but instead that it is capable of entering a limit cycle oscillation if enough momentum is introduced to initiate pendulum motion (as is done for these simulations by initializing with a non-zero swing angle). For this specific case, the motion is also very sensitive to perturbation by the unsteady aerodynamics of the oscillating wake, as can be seen at $t \approx 1.3s$, where unsteady variance in the flow creates an excessive, non-periodic negative pendulum moment that forces the scoop out of its limit cycle oscillation and into a wide, transient swing. During this phase, previously-unobserved, unsteady aerodynamics occur, as the scoop is now oriented towards the freestream at nearly $\theta = 40°$, which causes excessive "spillage" of high-pressure air around the leeward edge of the scoop. This motion eventually damps, and a stable limit cycle oscillation recommences.

Focusing on the periodic portion of the scoop's trajectory from $t = 0.8$-$1.2s$, the frequency of this periodic motion is approximately $5Hz$, which is higher than the $3Hz$ observed for the damped cylinder. The amplitude of this oscillation is approximately $\theta_{max} = 15°$ and appears to depend on the alignment of the asymmetric geometry with the flow, as discussed in Section 3.5.1. Unlike the cylinder, the FFT PSD analysis in Fig. 3.15b does not show an obvious, secondary-dominate, high-frequency component to the pendulum motion. This is because the wake of the scoop is much more complex and chaotic than that of the cylinder, as indicated by the general noisiness of the FFT of the loads in Fig. 3.15b. Thus, influences on the scoop's motion by the unsteady wake are random and introduce many minor tones rather than distinct, harmonic peaks. Like the cylinder, α_{eff} lags the pendulum θ at a relatively constant offset of $0.011s$. The unsteady influence of the wake on α_{eff} is most apparent at the pendulum peaks where swing velocity is minimal and local V_{eff} is dominated by the wake.

Unsteady Aerodynamic Loads

Time histories of the unsteady aerodynamic loads are co-plotted with the pendulum motion in Fig. 3.15a. Like the cylinder, the loads oscillate about their short-term average but at a higher secondary frequency of $\approx 120Hz$ due to the unsteady wake of the scoop leading to minor variations in the location of the leading edge stagnation point. Further harmonics are lost in the noise of the wake, caused by unsteady vortex shedding, oscillations of the vent and gap jets, and interaction effects discussed later in Section 3.5.1.

The axial force coefficient (C_A) of the 2D parachute-analog scoop maintains a relatively constant average value throughout the stable portion of the trajectory equal to ≈ 1.0, which is notably larger than the average drag coefficient of the cylinder $C_d \approx 0.7$ and is due to the cushion of air trapped in its windward cavity that spills from the sides at high velocity and rapidly increases the thickness of the separated shear layer, widening the wake and effective diameter of the bluff body, which is by design for an aerodynamic decelerator. Conversely, the normal force coefficient (C_N) and the total pendulum moment coefficient ($\Sigma C_{M,Y_i}$) are modulated symmetrically about zero at a low frequency equal to that of the pendulum motion. These parameters are the direct drivers of pendulum motion, as can be observed in Fig. 3.15a, where they are inversely proportional to θ, creating a restoring moment for any angular deviation of the pendulum from $\theta = 0$. Asymmetry in the motion does occur when random fluctuations in C_N due to wake dynamics alter the swing trajectory, usually at instances of high momentum as at $t = 1.3s$.

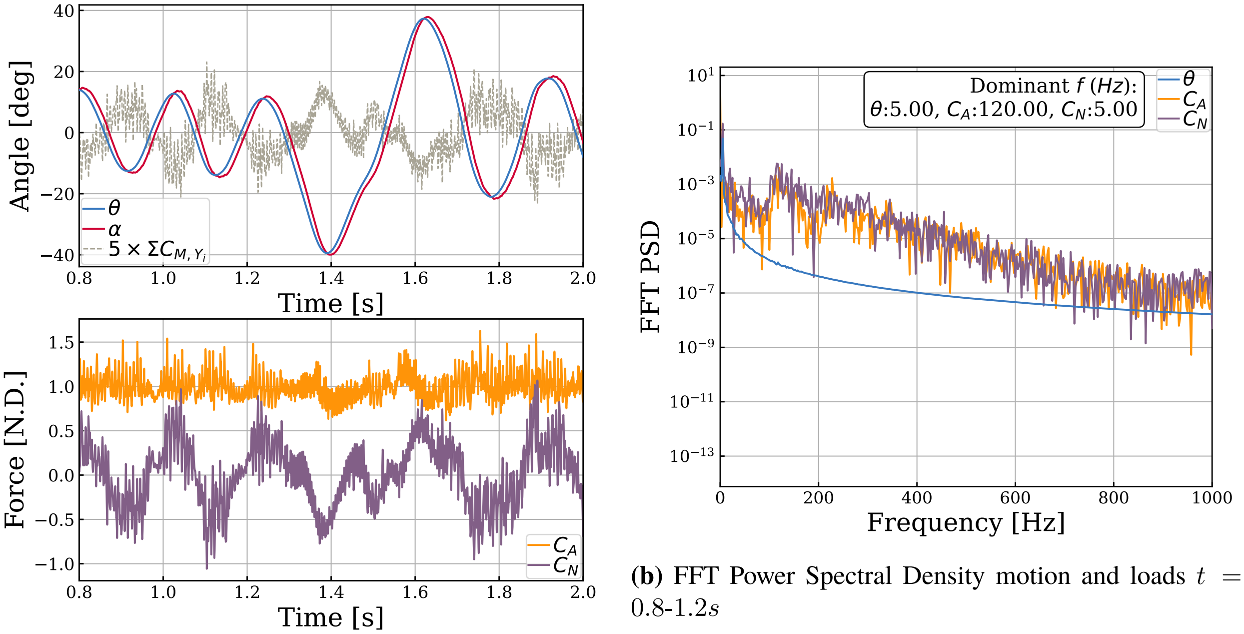

(b) FFT Power Spectral Density motion and loads t = 0.8-1.2s

(a) Motion and loads time history

Figure 3.15: Time histories and FFTs of motion trajectories and aerodynamic loads for a CFD-simulated, aerodynamically-driven, swinging, 2D scoop, with parameters including pendulum pitch/swing angle (θ), effective angle of attack (α_{eff}), total pendulum moment coefficient ($\Sigma C_{M,Y_i}$), and axial/normal force coefficients (C_A/C_N)

Unsteady Flow

Like the cylinder, the 2D scoop is a bluff-body in subsonic crossflow and displays similar periodic vortex shedding in its wake. Unlike the cylinder, however, the boundary layer separation location is fixed to the lip of the scoop, and there are additional unsteady interaction effects from the high-speed jets of flow traveling through the physical gaps in the scoop geometry. As flow travels over the scoop, its concave shape creates a cushion of high-pressure air in the cavity on the windward side (its primary source of drag). The pressure is relieved primarily through “spillage” of high-speed flow around the sides or “lip” of the scoop but also as air is forced through both the central vent and the porosity gap, inducing high-speed jets in the low-pressure wake. These jets displace the “spillage” vortices outward in the crosswise direction, leading to a wider wake and stronger surface pressure differential than the fully-turbulent cylinder flow. These phenomena can be witnessed for a stationary scoop aligned with the crossflow in the momentum streamlines shown in Fig. 3.16a. Another difference from standard bluff-body crossflow is that the Kármán vortex street is interrupted by additional vortex generation inside the wake due to the porosity gap jets. Shear layers originating from the edges of these gaps develop secondary wake vortices, which, for the stationary, $\alpha = 0°$ case in Fig. 3.16a, interact destructively with the primary Kármán vortices, dissipating the bluff-body wake relatively quickly. For the stationary scoop at higher angles of attack (Fig 3.16b), a large vortex spills off to the leeward side and, due to the high pitch/swing angle (θ) of the model, remains relatively clear of the rest of the wake, allowing much further propagation downstream than at $\theta = 0°$.

In the case of the moving scoop in Fig. 3.16c, the destructive action of the jets is less active at low angles because the motion of the pendulum physically separates the vortices shed at the extremes of the swing from those created by the jets, allowing wake vorticity to persist further downstream than in the stationary case. At peak swing angle, the relative, body reference frame, Z-direction speed of the pendulum reduces to zero, and the flow surrounding the dynamic scoop appears very similar to the stationary equivalent (Fig 3.16b vs Fig 3.16d). The dynamics of the moving scoop are most disparate from the stationary scoop at low angle of attack (Fig 3.16a vs Fig 3.16e), where the dissociation of the wake vortices through body motion alters the effective angle of attack, causing $\alpha = 0°$ to occur at $\theta \gg 0°$ and corresponds to a much more chaotic, unsteady wake condition than the stationary equivalent. Consequently, the aft surface pressure distribution on the moving scoop becomes similarly unsteady (the forward/interior surface pressure of the scoop can be considered roughly constant at all conditions due to the presence of the high-pressure air cushion), and the resulting unsteady surface loads significantly affect the dynamic stability of the geometry.

As with the cylinder, Fig. 3.17 depicts the time-varying nature of the body motion and unsteady flow for the scoop aeropendulum as it travels through a maximum-to-minimum swing from $t = 0.8\text{-}0.9s$. Time frames advance in the same manner as Fig. 3.10: left-to-right, top-to-bottom, with short-term intervals along the rows and long-term intervals down the columns. Like the cylinder, the aerodynamics of the scoop are subject to two modes of unsteadiness: local oscillations of the bluff-body wake and gross oscillations due to body bulk motion. Local unsteadiness is dominated by

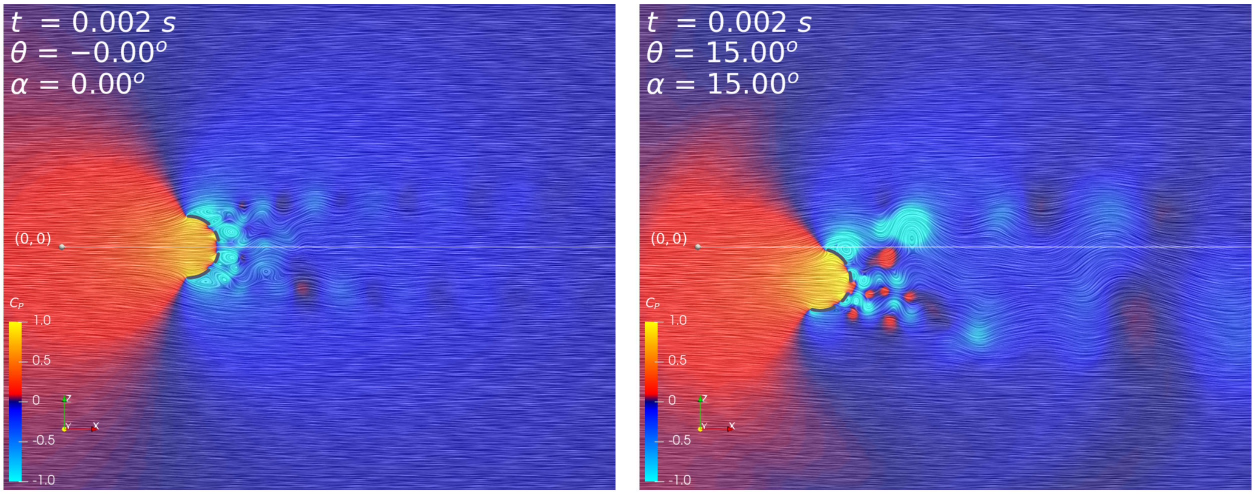

(a) Stationary ($\alpha/\theta = 0°$) **(b)** Stationary ($\alpha/\theta = 15°$)

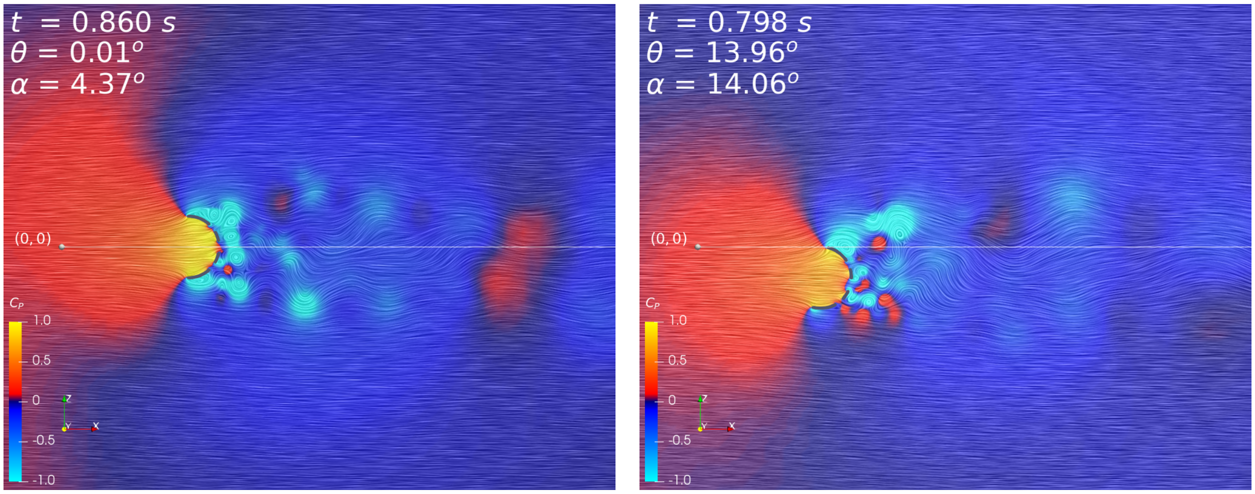

(c) Swinging ($\alpha = 4.4°, \theta = 0°$) **(d)** Swinging ($\alpha = 14°, \theta = 14°/max$)

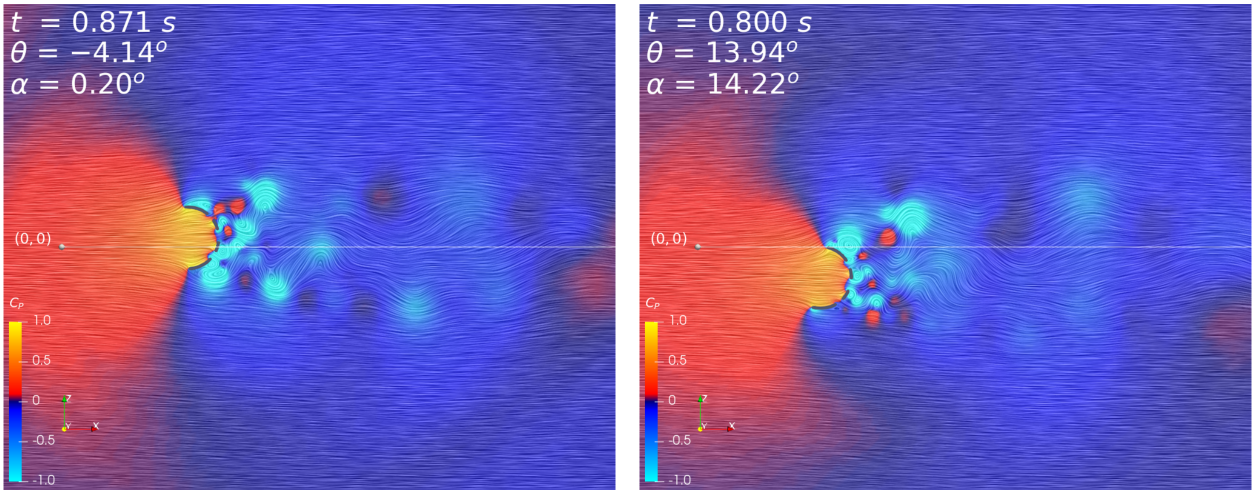

(e) Swinging ($\alpha = 0°, \theta = -4.1°$) **(f)** Swinging ($\alpha = 14.2°/max, \theta = 13.9°$)

Figure 3.16: Instantaneous flowfield pressure coefficient (C_P) contours and momentum streamlines for a stationary and moving 2D scoop aerodynamic pendulum ($Re = 8.4e6$)

the interaction of the shed vortices and porosity jets. At large angles (Figs. 3.17a-3.17c and 3.17m-3.17o), leeward lip vortex spillage occurs at a frequency of approximately $113.6Hz$, and the leeward porosity ring jet oscillates from positive to negative skew at a similar rate.

The vent jet is larger than the porosity ring jets and has no regular oscillation pattern but is instead subject to the influences of the shed vortices and jets to either side of it. Occasionally, when contained in a symmetric wake and undisturbed (as at zero swing angle in Fig. 3.17g), it generates symmetric vortices on either side of the vent at a very high frequency of $397Hz$. The symmetry of its behavior implies that it has less of an influence on the lateral stability of the motion and may function as a simple, linear mechanism for decreasing the pressure of the trapped air, thus reducing the total drag. The wide range of frequencies over which these unsteady phenomena occur contributes to the complexity and chaos observed in the solution for this dynamic system.

The bulk unsteadiness and motion of the scoop occurs in two distinct modes, depending on swing angle. The first unsteady mode occurs when the swing angle is $|\theta| < 5^\circ$, i.e. where the scoop is traveling through the centerline region. During this stage of the aerodynamics, the outboard vortex shedding becomes roughly symmetrical on both lips of the scoop, making the motion indeterminately stable, with no strong driver away from center except the momentum of pendulum, which carries it through. If swing momentum is reduced sufficiently, the scoop can remain within this region stably, but micro-fluctuations of the unsteady wake will likely ultimately jostle the scoop out of the stable center region. The second unsteady mode occurs outside of this band, where the leeward side of the scoop (interior to the swing) begins to shed a strong vortex, which slows the scoop's rotation and pulls it back to center. At this same condition, on the opposite, windward edge of the geometry, this vortex completely diminishes, as the outboard edge of the scoop is aligned with the flow and, thus, the boundary layer remains mostly attached to this segment, producing a weaker lift force than its leeward, high-angle-of-attack counterpart. This lift disparity is the source of the pendulum restoring moment and is present for both the stationary and moving geometries at high swing angles, which indicates that this geometry is statically stable at large swing angles. It appears that the alignment and attachment of the flow to the windward scoop segment is the primary driver determining the magnitude of the swing amplitude of the Aero6DOF pendulum, which is a truly useful result for parachute design and a distinct advantage of this tool. In contrast, a prescribed motion simulation would simply travel further through the swing arc, regardless of aerodynamic

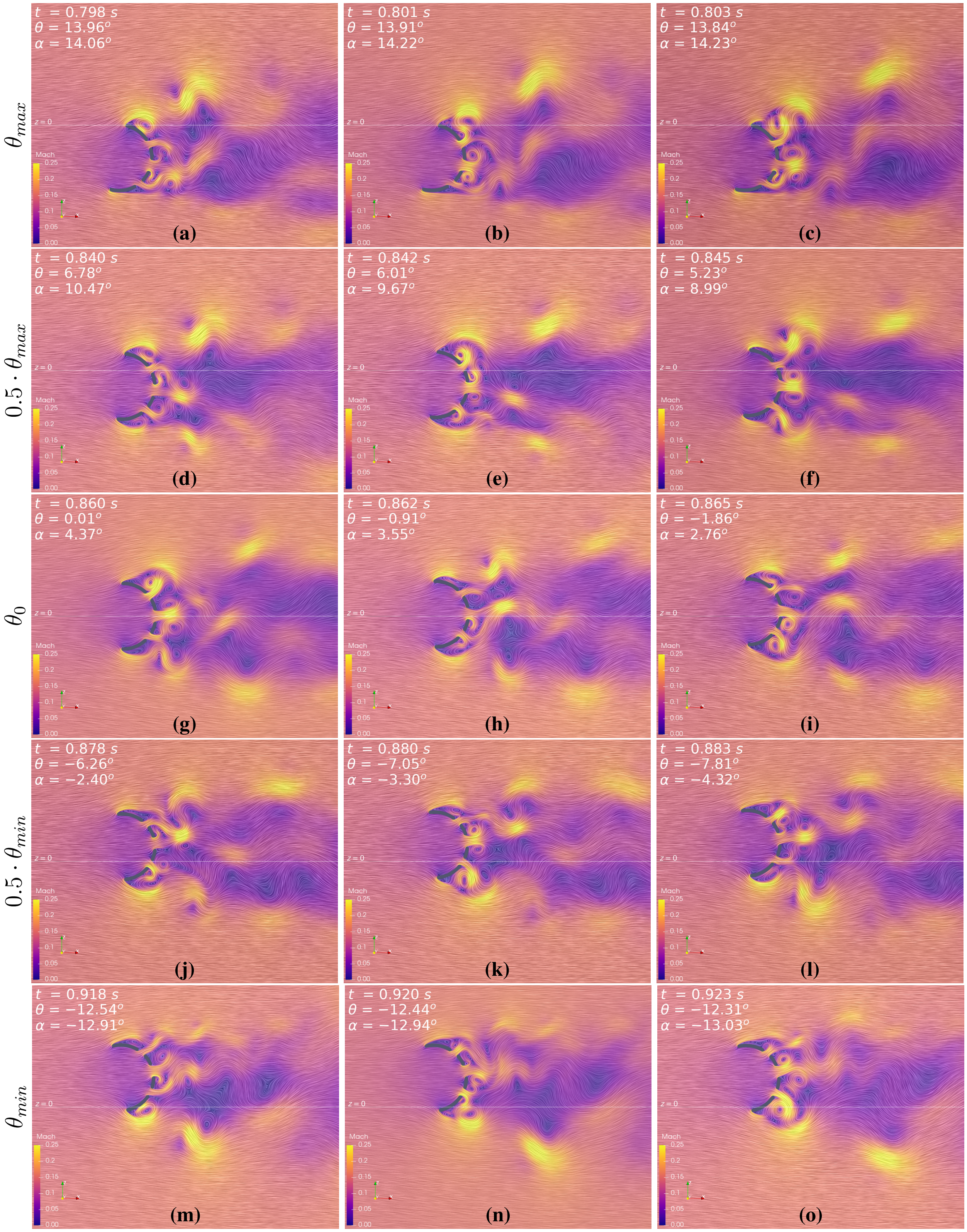

Figure 3.17: Chronologically-ordered, instantaneous frames of unsteady, flowfield Mach number contours and momentum streamlines surrounding a 2D scoop aerodynamic pendulum swinging counterclockwise from maximum to minimum amplitude ($Re = 8.4e6$)

influence, as instructed, and would provide the design engineer with an incorrect representation of the dynamical characteristics of this system.

3.5.2 3D Scoop

In addition to the two-dimensional parachute-analog, it was also desired to observe the effects of three-dimensional flow and multi-dimensional motion on the dynamics of the scoop aeropendulum system. For this purpose, a 3D version of the scoop grid was run constrained to both a 1-DoF, planar oscillation and a 2-DoF precessing oscillation, where the pendulum could rotate in any angular direction about the tether location.

Unlike the 2D flow equivalent, the wake of the 3D scoop was non-oscillatory, reducing the complexity of the aerodynamically-driven motion. Also unlike the 2D case, it was found that a trim condition exists for both the 1-DoF and 2-DoF 3D scoop pendulums at $\theta_s \approx 30°$, where θ_s represents the polar angle in spherical coordinates (the 3D equivalent of the 2D pitch/swing angle (θ)). In these simulations, the scoop was found to swing outward from its original starting angle and then exhibit a damping, planar oscillation about its trim angle as the total pendulum moment coefficient ($\Sigma C_{M,Y_i}$) went to zero, as shown in Fig. 3.18a. In the 2-DoF motion case, an additional total azimuthal pendulum moment coefficient ($\Sigma C_{M,Z}$) was introduced by the swing of the pendulum about the second spherical coordinate: the azimuthal angle (ϕ_s), which is also equivalent to the yaw angle (ψ) for this system. This moment does not damp to zero, but, rather, approaches a value of $C_{M,Z} \approx 0.02$, causing the scoop to begin a conic precession about its polar trim angle. This precession is most clearly observed in Fig. 3.18b, which shows the parametric motion of the scoop's centroid in two dimensions. In the figure, the 2D and 3D 1-DoF scoops' trajectories are depicted as vertical lines, as they are fully contained within the $y = 0$ plane. The 2D scoop exhibits a limit-cycle oscillation symmetric about the origin/centerline and the 3D, 1-DoF scoop trims to one side. The 3D, 2-DoF scoop also initially exhibits planar motion (depicted as a diagonal line with a slope determined by the initial values of polar angle (θ_s) and ϕ_s), but as it stabilizes about its polar trim, its azimuthal precession is seen as a tangential divergence from the initial swing plane.

Observing the flow at the scoop's polar trim condition in Fig. 3.19, it can be hypothesized that this angle corresponds to the alignment of the scoop's porosity gap with the crossflow direction, creating a minimum moment condition. In the figure, the strong jet shed from the upper side of

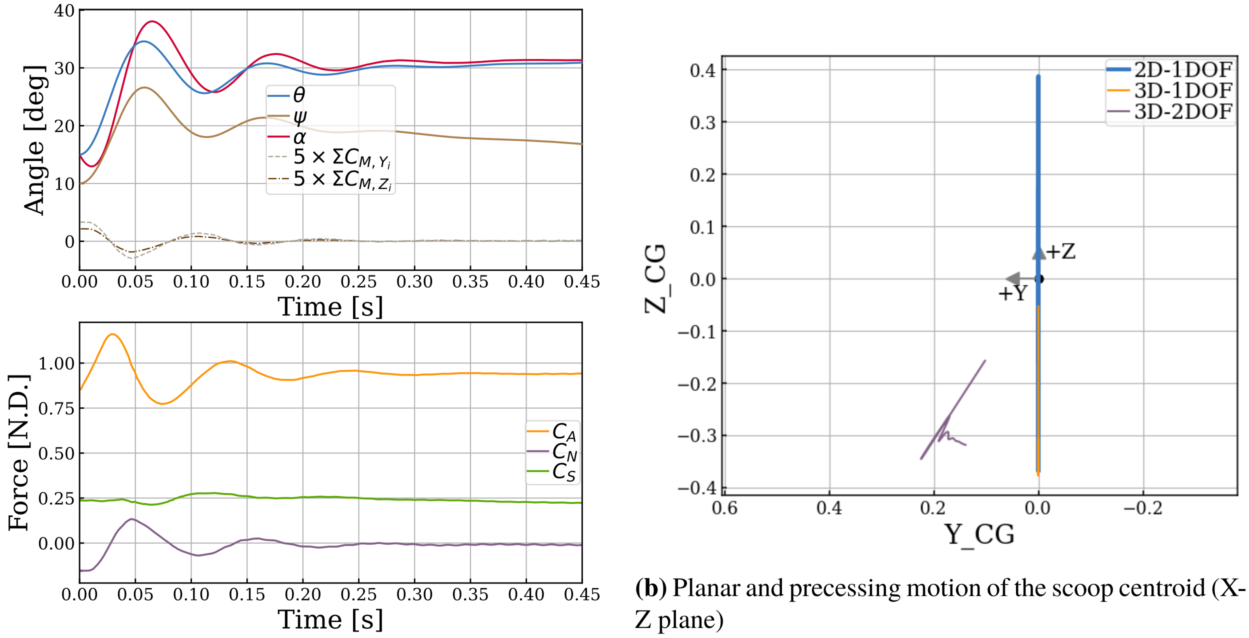

(b) Planar and precessing motion of the scoop centroid (X-Z plane)

(a) Motion and loads of a 3D, 2-DoF scoop

Figure 3.18: Aerodynamically-driven motion and loads of various scoop pendulums

the gap (interior to the swing) is essentially parallel with the direction of the crossflow. Indeed, simulations where this porosity gap was filled in entirely resulted in an unstable scoop that did not trim. The occurrence of trim for the 3D scoop geometry may be related to a relative weakening of the influence of the vortex shed from the canopy skirt compared to the 2D equivalent, which has an infinitely long vortex in the pitching plane in contrast to the ring vortex shed in 3D, which induces a moment in the swinging direction at only a single plane.

More investigation is required to assert the physical validity of this trim condition, as a number of the modeling simplifications made here (e.g. URANS turbulence modeling, explicit solution of body dynamics, etc.) could contribute to an artificial trim. For example, an unsteady wake induced by higher-fidelity turbulence modeling might prevent the pendulum from stabilizing in its trim location. In future investigations, experimental comparison would be ideal, both for validating the existence of a trim condition for this geometry and for comparison of the aerodynamically-driven motion, in general.

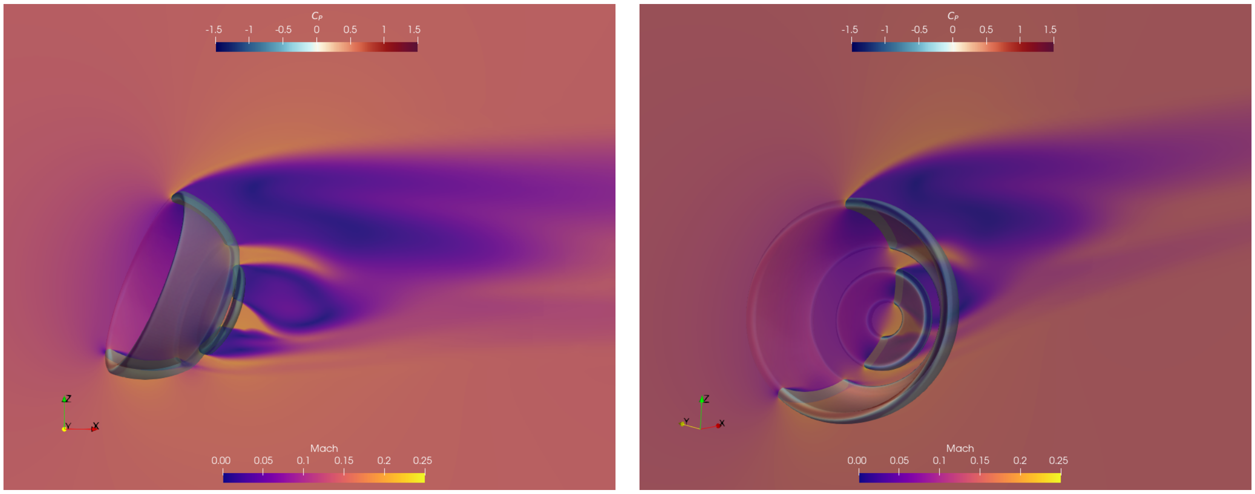

(a) Scoop gap jet aligned with crossflow

(b) Isometric view

Figure 3.19: Symmetry-plane flow slices showing the non-oscillatory wake of the 3D scoop at the trim condition

3.6 Summary

The work in this chapter demonstrated that OVERFLOW GMP can be used to accurately simulate aerodynamically-driven motion that is constrained at a point that is physically displaced from a body's center of mass in accordance with Research Aim I. A 2D cylinder geometry was used to develop an aerodynamic pendulum CFD model, which was calibrated through an extensive sensitivity study. Confidence was established in the realism of this model's flow physics solution by comparison to static wind tunnel experiments, which demonstrated realistic modeling of both the averaged integrated loads and the unsteady flow behavior. Validation of the accuracy of the coupled dynamics solver was demonstrated by comparison to a state-space, drag-based, numeric model of the same pendulum, increasing confidence in the ability of this model to predict realistic dynamic responses of untested flight geometries. The aerodynamically-driven pendulum motion was also matched with a prescribed motion simulation to demonstrate that this second, simpler technique is sufficient for accurate modeling if (and only if) a realistic motion trajectory is known a priori.

With validation of the aeropendulum model achieved, the tool was then used to analyze a simple analog of a parachute. Unsteady aerodynamics and motion of this previously untested design was simulated and was found to exhibit a stable limit-cycle oscillation in 2D. The 3D equivalent, instead, showed a tendency to trim at a swing angle of $\theta = 30°$ and also precess in a cone about that angle.

Further understanding of this trim phenomenon and of the unsteady aeropendulum system in general could be better informed in future work by an analogous wind tunnel test of these geometries.

Chapter 4

Parachute Pendulum CFD Model

4.1 Introduction

Research Aim II of this dissertation was to model the aerodynamic loads and dynamic stability of the pendulum motion of the Orion Multi-Purpose Crew Vehicle (MPCV) main parachute using rigid-body, prescribed motion Computational Fluid Dynamics (CFD) and to demonstrate accuracy sufficient for general engineering design purposes. Physical accuracy of the model was validated by direct comparison to the sub-scale wind tunnel test (WTT) of the same geometry conducted by Anderson et al. and discussed in Section 1.2.2. High-accuracy CFD solutions were achieved through high-fidelity modeling of the test article geometry. Prescribed motion was employed since known motion tracks were available from photogrammetry of the WTT.

Before making comparisons to experimental results, the CFD parachute model was tuned through an extensive sensitivity study to ensure acceptable convergence and to affirm the validity of the approximations made in the model. Then, the fully-calibrated model was simulated in an analogous condition to that of the WTT for comparison. Comparisons were also made to the aerodynamically-driven scoop from Chapter 3 to assess the relevance of that simple geometry as a true parachute-analog.

4.2 Model Development

4.2.1 Assumptions and Simplifications

The parachute prescribed motion model that was developed in this research is based directly on the stationary, rigid parachute CFD analysis conducted by Greathouse and Schwing (2015) [18].

Adaptation of their stationary parachute simulation to a dynamic pendulum simulation was made tenable by applying assumptions about and approximations of the parachute motion in addition to the rigid parachute CFD best practices already established in their study. The resulting moving parachute pendulum model is subject to the following assumptions and simplifications:

- Geometry simplifications
    - The parachute canopy geometry is rigid and does not allow transient structural deformations like "breathing". The bulk nature of the dynamics is attributed to the average inflated shape of the canopy.
    - The parachute tether is also rigid, allowing no roll rotation (axisymmetric geometry) or lengthening or slackening (transient spring-damping effects).
    - The parachute fabric is nonpermeable. Omitted mass flow through the canopy material is compensated by geometric porosity.
    - The dynamical influences of certain parachute geometry features (e.g. small porosity windows) are secondary in effect to other characteristics (e.g. vent, porosity ring) and can be omitted while still recovering the primary dynamic stability characteristics of the parachute.
- Flow modeling simplifications
    - Freestream flow during flight and WTT ($M = 0.03$) is incompressible and can be scaled to higher, incompressible Mach number to avoid low-Mach preconditioning approximations by the CFD solver while maintaining dynamic similarity.
    - The WTT and flight Reynolds number of $Re = 9e6, 2.4e6$ both exhibit fully-turbulent shear layers that separate from the fixed location of the parachute skirt lip and are thus self-similar.
    - Bulk behavior of the unsteady, bluff-body wake can be reasonably approximated with Unsteady Reynolds-averaged Navier-Stokes (URANS) turbulence modeling given that boundary layer separation is geometry-determined.

  - Flow and vortex shedding is symmetric about the pitching plane for a 1-DoF, axisymmetric, parachute pendulum and can be approximated with a mid-plane symmetry boundary condition to reduce computational resource requirements.

- Dynamics and stability analysis assumptions

  - The dynamic stability characteristics of the parachute are unchanged when scaling between incompressible Mach numbers when the dynamic pressure ($\overline{q}$) is scaled proportionally.
  - Multi-DoF WTT parachute motion can be sufficiently approximated with a 1-DoF equation fit to the pitch/swing angle (θ) observed with photogrammetric vent tracking.
  - Direct comparison between the planar oscillations of the CFD parachute pendulum and the precessing motion of the WTT can be made using phase plane analysis dependent on the total angle of attack $\alpha_T = \cos^{-1}(\cos\alpha\cos\beta)$ due to the parachute's axisymmetric geometry [82].
  - Individual parachute instability is a direct cause of parachute cluster pendulum motion [13], therefore, stability improvements to a single parachute canopy should improve the overall stability of a parachute cluster (though analysis of the entire cluster is necessary to recover dynamic effects of chute-chute proximity interactions [14]).
  - Upstream wake influences from the attached capsule and tether have negligible effects on parachute dynamic stability characteristics for a sufficiently large canopy [4, 14, 83].

A number of these assumptions and simplifications were assessed and justified by parametric variation of simulation parameters, as discussed in Section 4.3. Each of these simplifications represent an aspect of the model provided by the current research that could be enhanced in future implementations to improve the realism and accuracy of the predicted aerodynamics and to better-match WTT results for refinement of uncertainties.

4.2.2 Parachute Geometry

The geometry of the Orion MPCV Engineering Design Unit (EDU) ringsail parachute modeled in this research is described in detail in Section 1.2.1. Some simplifications to the drop test and

WTT EDU article were made in the CFD geometry for ease of modeling. Specifically, porosity "windows" seen in Fig. 1.5b at every 5th gore of the 7th sail (3rd from the skirt) were not included in the computational model, as their effects were deemed secondary to the skirt ring vortex and porosity gap jet as the main drivers of wake unsteadiness.

In addition to the flight-scale Orion MPCV main parachute geometry simulated in free-air, parachute pendulum motion was also simulated for a two-segment, Disk-Gap-Band (DGB) parachute within the National Full-scale Aerodynamics Complex (NFAC) $80'$x$120'$ test section analogous to the test conducted by Schairer et al. (2018) [84] of the Mars2020 parachute as part of related work. The relevance of these simulations to the current work is the additional modeling of the wind tunnel test section walls and of any blockage incurred by the large parachute geometry within this enclosed volume [85]. The DGB parachute geometry is notably different from that of the Orion ringsail, in that it is designed for supersonic flight conditions rather than subsonic descent. The canopy of this parachute consists of only one apex ring segment with a central vent and one band segment at the skirt instead of a sail. These two segments are separated by a large geometric porosity gap. Though the complexity of this geometry is significantly reduced in comparison to the Orion ringsail, the primary hemispherical shape interrupted by a central vent and large circumferential gap is similar, so general comparisons can be made between these two geometries for the purposes to assessing the sensitivity of simulation results to wind tunnel blockage. The differences between the Orion ringsail and DGB parachute geometries can be compared in Figs. 4.2d and 4.3b, respectively.

As a topic related to parachute geometry, it is relevant to note that the parachute body force reference frame is rotated $180°$ about the y-axis/θ-axis relative to that defined for the aerodynamic pendulum in Fig. 2.1. This design choice is an artifact of the parachute being mounted on the portion of the spacecraft that faces forward during launch and aft during reentry. The parachute retains its orientation axes from the launch phase of the flight envelope for compatibility with the entire launch system, even though that forward phase of flight is unrelated to the actual operation of the parachute. Consequentially, parachute drag and axial force occur with a negative sign during normal operation, so the y-axis of the axial force coefficient (C_A) plot in Fig. 4.4 has been inverted to maintain an intuitive orientation, where increases in y indicate an increase in magnitude. Additionally, the normal force is reported as the missile-frame normal force coefficient ($C_{N,m}$), which takes advantage of the axisymmetric nature of the parachute geometry to transformation variations due to the aerodynamic clocking angle (ϕ_c) into a single plane, allowing direct comparison between planar and precessing motion. To avoid confusion, force and moment results reported in the parachute reference frame will be given the $|_P$ notation.

4.2.3 Simulation Design

The freestream conditions of the Orion EDU parachute wind tunnel test as well as those of the moving parachute CFD simulations for this research are summarized below in Table 4.1 for the three comparison cases, which are:

"WTT": The wind tunnel test of the $35\,\%$-scale EDU parachute conducted in the NFAC $80'$x$120'$ by NASA and its associated partners

"EDU": A CFD simulation of the full-scale Engineering Design Unit prescribed to an approximation of the motion observed in the WTT

"DGB": A simple prescribed motion CFD simulation of the full-scale Disk-Gap-Band parachute with modeling of the NFAC $80'$x$120'$ test section geometry

The Orion EDU CFD model geometry is generated at flight-scale, rather than the $35\,\%$-scale of the WTT model for compatible use in flight databases. This scale change corresponds to a factor of 2.5 increase in the Reynolds number (Re), but comparability between simulation and test is maintained because both flows are fully-turbulent and flow separation always occurs at the lip of the parachute skirt. Parametric simulation study in Section 4.3.3 demonstrates that this change in Reynolds number (Re) has minimal effect on the dynamic loads of the parachute.

The CFD simulation freestream Mach number is scaled from the Orion MPCV flight condition of $M = 0.03$ to $M = 0.15$ to improve numerical stability by avoiding low-Mach preconditioning in the OVERFLOW CFD tool [18]. Simulation freestream density (ρ_∞) was selected such that simulation $\overline{q}$ would scale proportionally to the freestream velocity (V_∞), preserving the dynamic stability characteristics of the moving system. In this case, both V_∞ and $\overline{q}$ are increased by similar factors of 5 and 4.55, respectively. Because the relative motion of the pendulum geometry affects the local $\overline{q}$ in these simulations, the prescribed motion equations designed from observations of the flight and WTT motion is also scaled in the same manner.

Simulations of the DGB parachute within the wind tunnel test section were designed for a different WTT, so dynamic similarity is not maintained between this simulation and the Orion parachute WTT used as validation in this research. However, this difference can be compensated for with an appropriate scaling factor in order to compare gross trends in dynamic stability for the purposes of assessing the effects of blockage within the wind tunnel. Differences in Re are also acceptable for the same reasons as the Orion parachute simulation.

Table 4.1: Summary of freestream conditions for the sub-scale wind tunnel test and full-scale, prescribed motion CFD simulation of the Orion parachute

	Chute	$\boldsymbol{L_{ref}(ft)}$	$\boldsymbol{M_\infty}$	$\boldsymbol{V_\infty(^{ft}/_{s})}$	$\boldsymbol{\overline{q}(psf)}$	$\boldsymbol{\rho_\infty(^{slug}/_{ft^3})}$	$\boldsymbol{Re}$
WTT	35%EDU	40.6	0.03	33.2	1.36	$2.47e$-3	$9.00e6$
EDU	EDU	116	0.15	166	6.19	$4.51e$-4	$2.36e7$
DGB	DGB	48.0	0.107	119	16.78	$2.37e$-3	$3.62e7$

Solutions for bluff-body flow are generally unsteady, so a time-accurate solver is utilized with multiple Newton sub-iterations at each time step to improve convergence. Time is advanced implicitly using the Beam-Warming scalar pentadiagonal scheme [86]. Time step size was determined by successively decreasing the step size until the behavior of the results became independent of this change (Section 4.3.2). The two-equation Shear Stress Transport (SST) Reynolds-averaged Navier-Stokes (RANS) turbulence model is employed [80] for modeling of the primary characteristics of the massively-separated parachute wake, which is shown to be an acceptable approximation by comparison to an analogous Detached Eddy Simulation (DES) simulation in Section 4.3.5

4.2.4 Prescribed Motion Development

Prescribed motion of the moving parachute simulations was developed in a step-wise fashion, with successive improvements to the fidelity of the simulation's replication of the WTT motion. This process allowed the determination of CFD best practices for moving-body parachute simulations. Table 4.2 describes the various stages of simulation development, and Fig. 4.1 shows the corresponding simulation geometries and flowfields.

Initial simulation prototyping began with simple geometry and basic pitching motion about the parachute's own centroid ("Pitching", Fig. 4.1a). Next, the EDU parachute was prescribed to swing

Table 4.2: Parachute pendulum motion CFD model fidelity improvements

Case	Geometry	Prescribed Motion Equation
Pitching	Simple EDU	Simple pendulum, pitch about centroid, WTT frequency
Swinging	EDU	Simple pendulum, swing about tether, flight freq./amp.
DGB	DGB+Walls	Simple pendulum (DGB WTT frequency/amplitude)
WTT-Track	EDU	2-frequency Fourier decomposition of EDU WTT motion

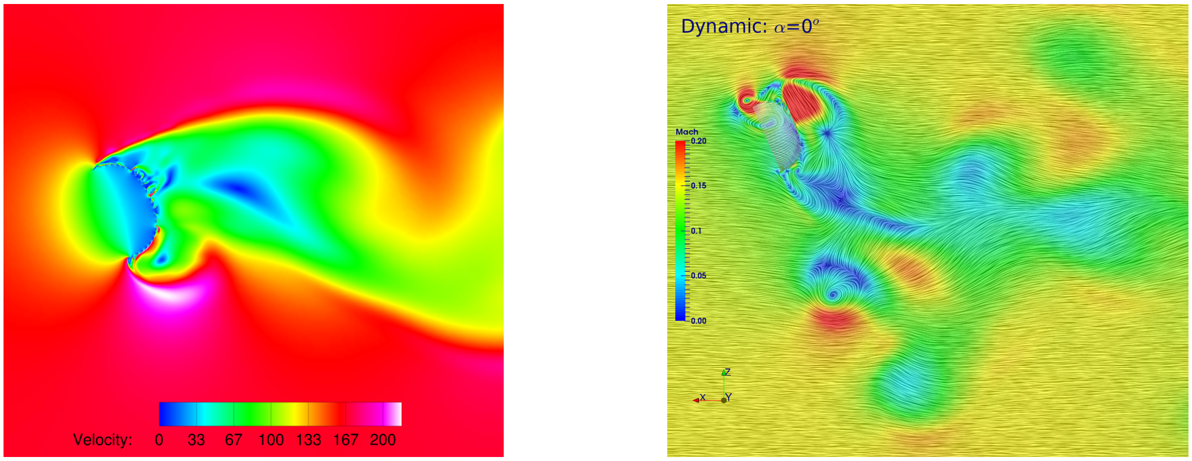

(a) Simple pendulum pitching about centroid (EDU)

(b) Simple pendulum swinging about off-body tether location (EDU)

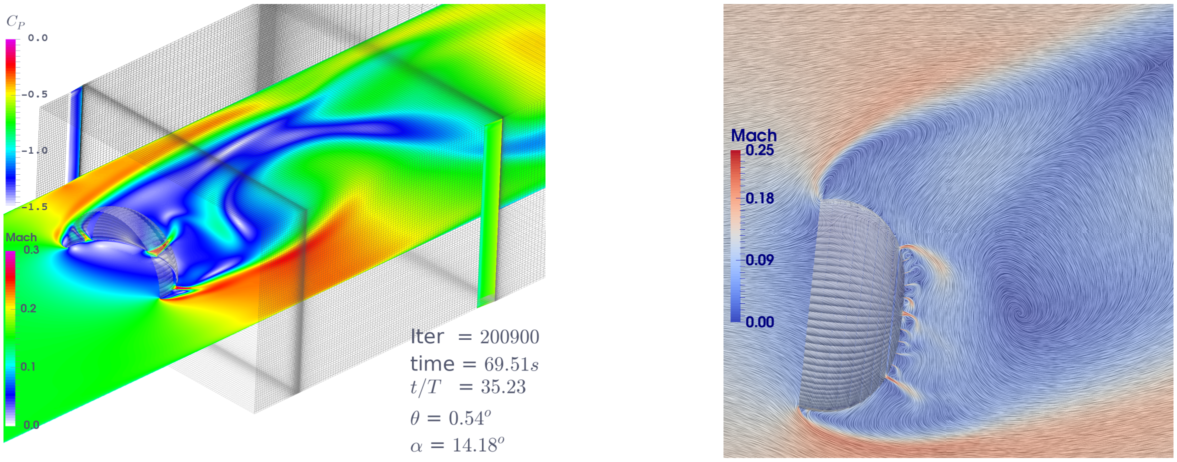

(c) Simple pendulum swinging within wind tunnel walls (DGB)

(d) 2-frequency fast Fourier transform (FFT) fit of EDU WTT motion

Figure 4.1: Developmental stages of the prescribed parachute CFD model, with increasing fidelity of motion and geometry

about an off-body tether location according to the scaled swing frequency and amplitude of oscillation observed in drop testing ("Swinging", Fig. 4.1b). This implementation served as the tuning model for grid and time step sensitivity studies and provided estimates of the dynamic aerodynamics of the main parachute in flight. Additional dynamics post-processing methodologies were developed for this and following simulations that computed the relative dynamic aerodynamics in the moving body reference frame (See Chapter 2). Then, various sensitivity studies were performed with the DGB parachute within the NFAC $80'$x$120'$ test section in order to establish further confidence in the validity of the simplifications and approximations made for these simulations.

Finally, the WTT EDU comparison simulation motion trajectory ("WTT-Track", Fig. 4.1d) was derived by decomposing the motion observed in testing into superimposed sinusoidal functions. The observed WTT trajectory was fit just after initial release, when motion was primarily planar, to maintain compatibility between the multi-DoF, precessing WTT and symmetry plane-constrained simulation. The frequencies of the WTT-measured pitching/swing angle θ were decomposed using FFT analysis and the two dominant frequencies were used to approximate the motion with the form:

$$\begin{gathered}\omega_1 = 2\pi(0.186\,246 Hz),\ \omega_2 = 2\pi(0.200\,573 Hz) \\ A_1 = 0.011\,695°,\ A_2 = 4.268\,271°,\ A_3 = 1.001\,533°,\ A_4 = 4.983\,758° \\ \theta(t) = -A_1 \sin(\omega_1 t) - A_2 \cos(\omega_1 t) + A_3 \sin(\omega_2 t) + A_4 \cos(\omega_2 t) + \theta_0\end{gathered} \tag{4.1}$$

where ω are the natural frequencies of the oscillation and A are the associated Fourier coefficients and the initial swing angle is equal to the maximum swing angle $\theta_0 = \theta_{max}$. However, for prescribed motion simulation in OVERFLOW Geometry Manipulation Protocol (GMP), the rate of motion is the controlled variable, so Eqn. 4.1 is differentiated with respect to time to obtain the simulation prescribed motion equation:

$$\dot{\theta}(t) = -A_1\omega_1 \cos(\omega_1 t) + A_2\omega_1 \sin(\omega_1 t) + A_3\omega_2 \cos(\omega_2 t) - A_4\omega_2 \sin(\omega_2 t) \tag{4.2}$$

where $\dot{\theta}$ is the pitch rate of the parachute and the initial pitch rate is zero for a pendulum starting at the apex of its swing $\dot{\theta}_0 = 0$. This motion track operated at a lower frequency and amplitude than the flight behavior and provided directly analogous results to the WTT. As stated in Section 4.2.1, direct comparison between test and simulation was possible using phase-plane analysis of total angle of attack (α_T).

As a result of this successive enhancement of motion complexity, a refined, best-practice convergence procedure was established for moving-body pendulum runs and is as follows:

1. Flow initialization: full-multigrid, steady-state
    - Stationary, at maximum swing angle (zero relative swing velocity)
2. Flow convergence: stationary, time-accurate
    - Achieve realistic flowfield for pendulum motion initial condition
3. Transient: moving, time-accurate
    - Prescribed motion is initiated
    - Run until transient start-up effects have propagated downstream
4. Periodic: moving, time-accurate
    - Motion and aerodynamic forces are regularly periodic
    - Quasi-steady sample data may be acquired

4.2.5 Grid Development

Computational meshes for the Orion EDU parachute were generated following the same strategies presented for the aerodynamic pendulum simulations in Section 3.2.2. The following section describes the specific techniques required to model the various parachute geometries considered in this study as discrete, structured, overset, volume meshes.

Grid Generation

Parachute surface meshes are generated using the process developed by Greathouse and Schwing for the static parachute study. The inflated geometry of the parachute canopy is determined using the Sandia National Labs Canopy Loads Analysis (CALA) tool [87]. This structural model iteratively computes the geometry of a single parachute gore (angular section shown in Fig. 4.2a) using stress-strain relations and inputs concerning the specific geometry features of the parachute. A surface mesh is then mapped onto this gore geometry model and is revolved about the parachute axis of symmetry to create the complete axisymmetric parachute surface geometry.

Like the simulations in Chapter 3, the parachute volume grid systems are built using Chimera Grid Tools (CGT) Grid Scripts, which grow the near-body volume using hyperbolic stretching from the surface grids and then surround the geometry with nested, off-body box grids to capture the wake and farfield. The resulting general grid system is depicted in Fig. 4.2. The parachute canopy near-body geometry consists of individual, periodic volume grids for each ring. Fine, isotropic box grids occupying the vent region ("ventbox") and closely surrounding the parachute ("chutebox") move with the parachute to convey fine flow features like the unsteady, turbulent jets that are induced through the central vent, between the eleven ring gaps, and through the fullness of the sails. A fixed "wakebox" extends downstream to provide fine grid resolution for bluff-body wake propagation, and nested off-body box grids extend out to the farfield to connect the near-body and wake solutions to the freestream boundary condition.

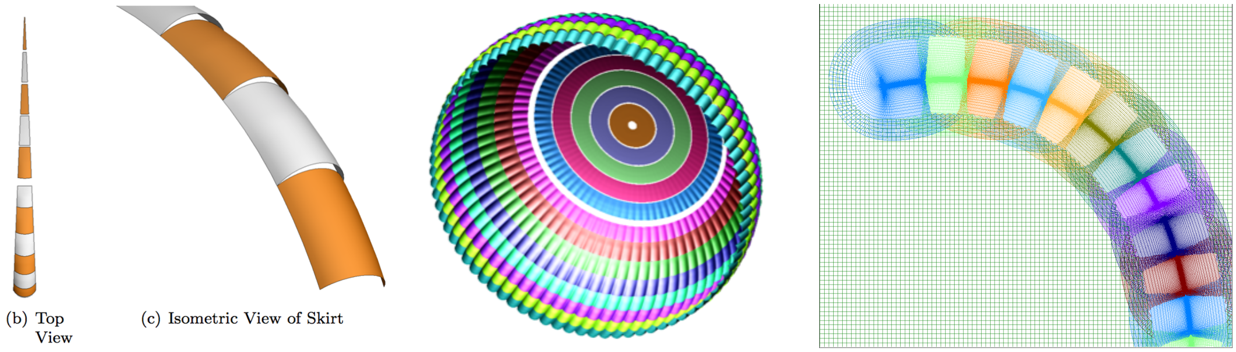

(a) Single parachute gore from inflation model [18] **(b)** Surface mesh basis for volume grid generation **(c)** Slice of individual volume grids for each ring segment

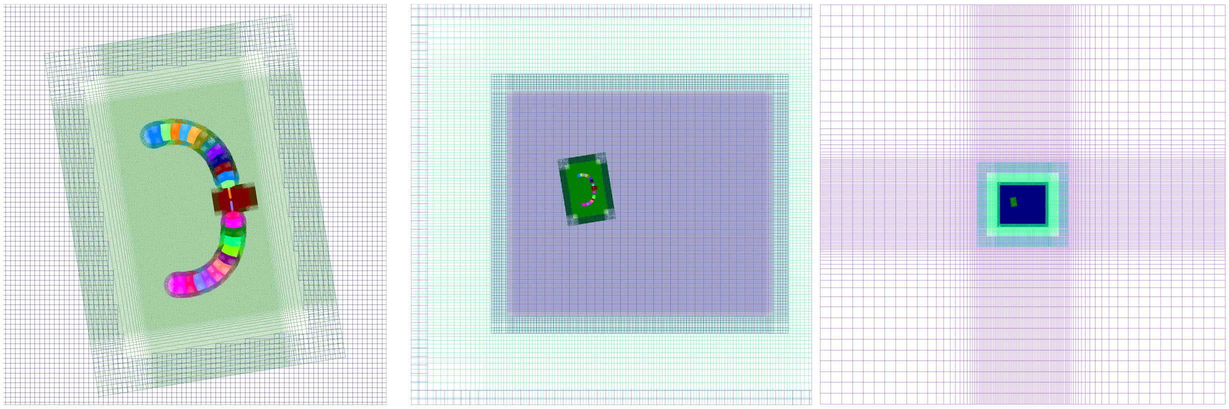

(d) Body-motion-tracking boxes **(e)** Stationary wake-resolving box **(f)** Farfield boxes

Figure 4.2: The Orion parachute surface grid (full hemisphere shown for demonstration) and the half-symmetry volume grid system generated from that surface, shown in $y = 0$-symmetry-plane slices

Domain Connectivity

Unlike the Aeropendulum, parachute simulations for this work were completed before mixed-mode PEGASUS 5/Domain Connectivity Function (DCF) was implemented in OVERFLOW and, thus, use traditional DCF with a custom phantom cutter process developed for this work. DCF is required for moving-mesh CFD because cell blanking and interpolation stencils must be recomputed at each time step if there is relative overset grid movement. Static solutions using DCF were compared to simulations with PEGASUS 5 grids to confirm similar functionality. These comparisons determined that the best practice for DCF hole cutting of parachute grids is to extract surfaces from the volume grids of each parachute segment, creating "phantom" cutter surfaces (see Fig. 4.3). These surfaces are "X-rayed" and use a zero-cutting distance to give almost exact control of interpolation regions and enable fine cutting within the small parachute gaps without restricting the expansive cutting elsewhere around the segment. The resulting grid system achieves similar overlap and interpolation to that of an optimized PEGASUS 5 equivalent and consists of approximately 100 million vertices when a half-symmetry plane boundary condition is employed to reduce grid size by a factor of 2.

Though the modern mixed-mode PEGASUS 5/DCF process that is now available in OVERFLOW would be more automatic and potentially optimized, the phantom cutter approach provides

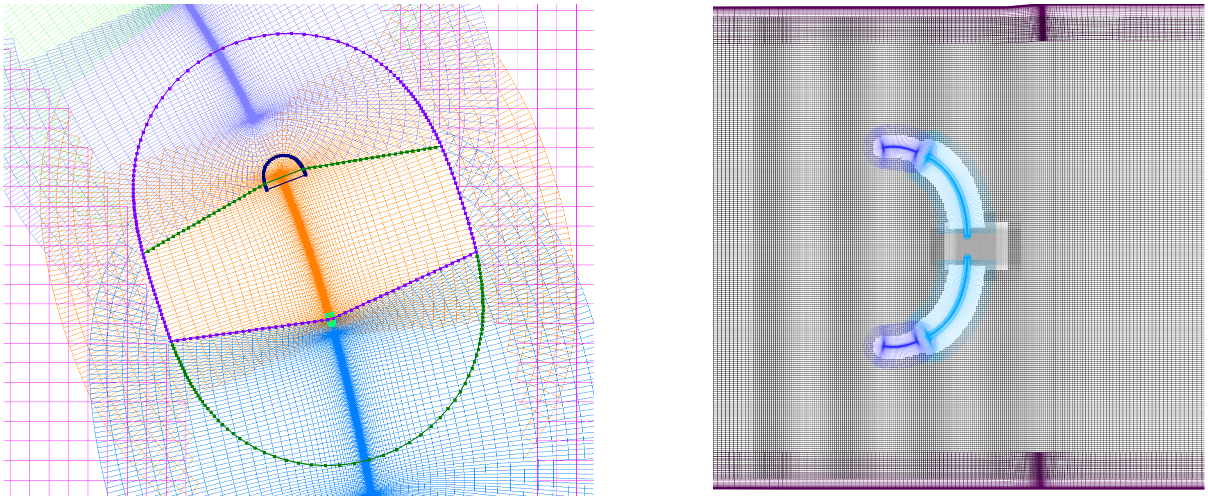

(a) Outlined phantom cutter grids (four for each parachute segment)

(b) Phantom cutter cell-blanking for DGB parachute within wind tunnel test section

Figure 4.3: Examples of efficient cell blanking and interpolation between overlapping parachute segments created by DCF phantom cutters, show in $y = 0$-plane slices

one distinct advantage in that it does not require a body-tracking chutebox to maintain relative interpolation stencils like mixed-mode DCF would. This allows simpler grid construction when the parachute is contained within a wind tunnel geometry like the DGB parachute in Fig. 4.3b, as additional instruction would be required to prevent a chutebox from penetrating the walls at the apex of its swing and creating flow leakage out of the test section.

4.3 Sensitivity Studies

4.3.1 Grid Size Sensitivity

Solution independence from grid resolution was ensured through a series of comparison studies. Mesh generation best practices that were determined from each of these tests were incorporated into following simulations. First, for the initial swinging parachute, the resolution of the parachute near-body volume mesh was refined by increasing the angular resolution of the parachute surface grid. Refinement was increased until the small, turbulent, near-body features (such as the separated shear layer starting at the skirt lip and the jets formed in each gap) were well resolved and visually unchanged by further grid refinement.

Solution sensitivity to the resolution and sizing of the wake resolution grids was also assessed in a similar manner. Inclusion of the body-tracking “chutebox” was a direct result of these studies, as the resolution of the fixed-position wakebox alone was insufficient to accurately resolve the fine flow features induced by the vent and each of gaps and also within each sail’s fullness.

4.3.2 Time Step Sensitivity

Solution independence from time step size was determined by successively decreasing the physical time step DT until the integrated aerodynamic loads became independent of this change. These tests were completed for each unique parachute simulation with a moving parachute to ensure the chosen time step was sufficiently small when accounting for the additional relative swing velocity. Fig. 4.4 shows the axial and normal body force convergence of the “Swinging” parachute from Fig. 4.1b, which represents the greatest freestream Mach number and relative pendulum movement combination, and is, thus, the most sensitive to time step size.

Time histories of C_A and normal force coefficient (C_N) are reported in the parachute reference frame ($|_P$) discussed in Section 4.2.2 and are plotted in the left column of Fig. 4.4. Corresponding phase plane mappings of these parameters as a function of α_T can be found in the right column of the figure. The time histories show diminishing sensitivity to as time step is reduced, with minimal differences in peak force magnitude below $DT = 0.5$. The phase plane analysis shows the relevance of time insensitivity to accurate dynamic stability modeling, particularly in the divergence of the Blue $DT = 1.0$ C_N curve from its counterparts. This form of analysis will be used in the following sections to demonstrate similarity of solutions and analyze parachute pendulum dynamic stability.

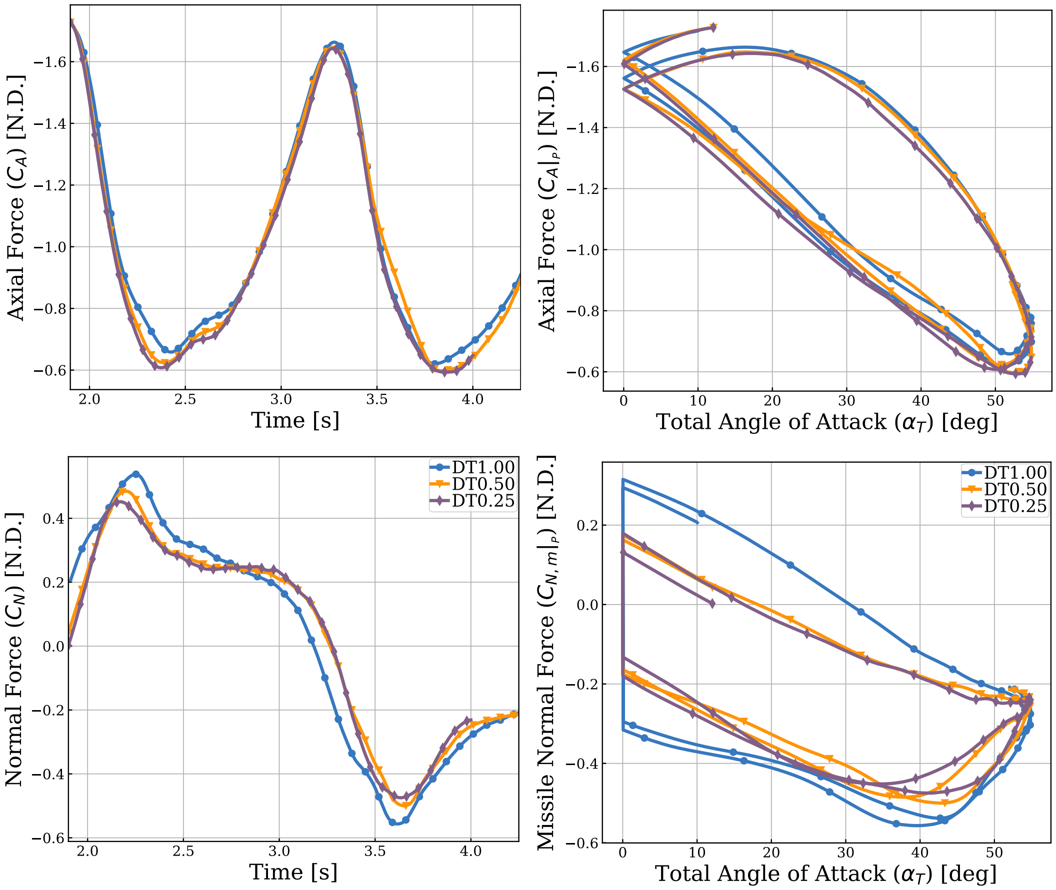

Figure 4.4: Time step sensitivity study for a parachute prescribed to a simple pendulum approximation of the motion observed in flight testing, where diminishing dependence occurs at $DT = 0.5$

4.3.3 Reynolds Number Scaling

The prescribed, swinging parachute was also run at the wind tunnel Re to demonstrate that the flight and WTT conditions are self-similar. The resulting dynamic, unsteady, aerodynamic loads on the parachute were minimally different than the flight-scale case, suggesting minimal dependence on Re at these scales. Figure 4.5 corroborates this conclusion with comparisons of the URANS bluff-body wakes generated in each case. Slight differences are apparent in the steady flagging

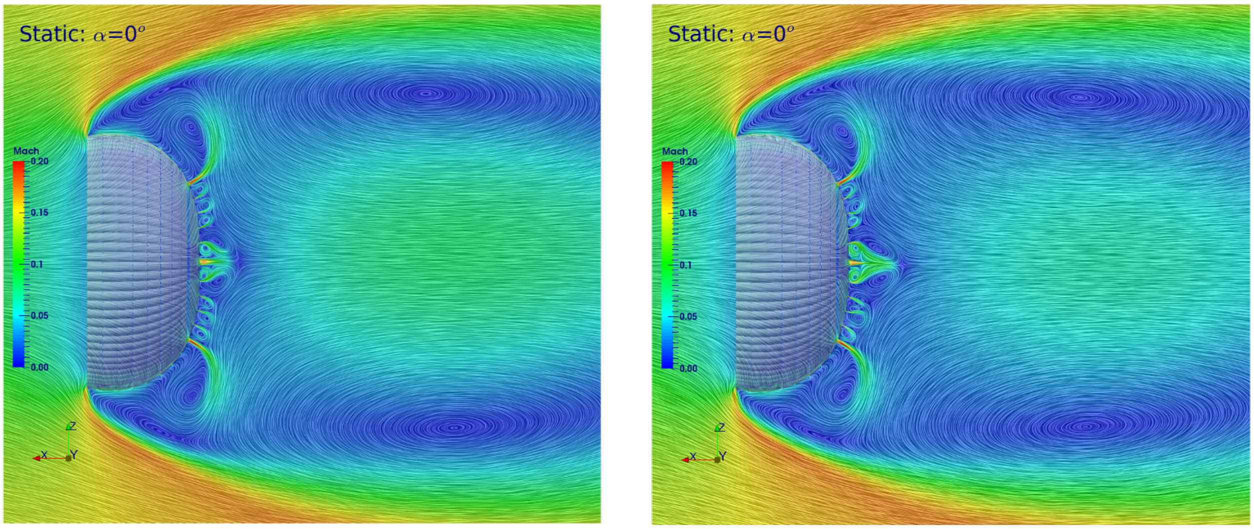

(a) Full-scale Re, $\alpha = 0°$ **(b)** Wind tunnel-scale Re, $\alpha = 0°$

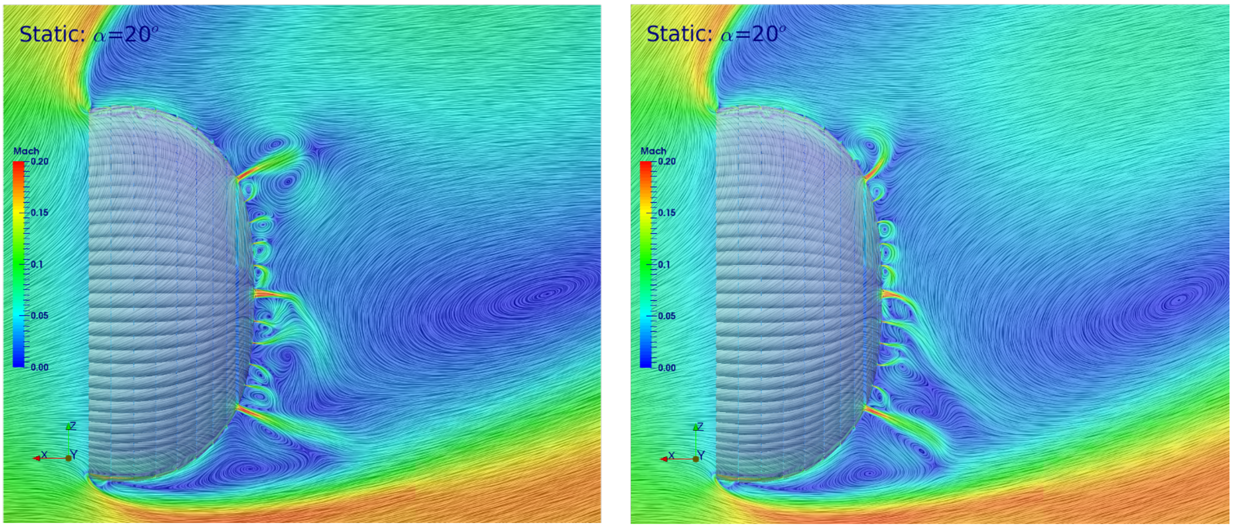

(c) Full-scale Re, $\alpha = 20°$ **(d)** Wind tunnel-scale Re, $\alpha = 20°$

Figure 4.5: Static, URANS parachute simulations at flight- and wind tunnel-scale Reynolds number $(Re = 16965in^{-1}/6937.75in^{-1}, M = 0.15)$

position of the various gap jets, but the bulk shape of the wake and size and position of the skirt lip shear layers are minimally different.

4.3.4 Wind Tunnel Walls

Simulations of the DGB parachute inside of the NFAC $80'$x$120'$ test section geometry were utilized in this work to assess the assumption that similar dynamic stability trends will be obtained for parachutes in free air and within the wind tunnel. Qualitative differences in the flowfield can be compared between the two cases in Figs. 4.1c and 4.1d. Both parachutes exhibit a bluff-body wake with strong vortex shedding on the leeward side of the pendulum swing and jet-like features from the porosity gaps that interact with the main turbulent wake dynamics. In the case of the DGB parachute, blockage is apparent in the high speed flow that jets around each side of the parachute. However, the effects on the fine features of the near-body flow around the parachute are relatively minimal. The windward separated shear layer is already compressed close to the body for the EDU free-air simulation, so the proximity of the wind tunnel walls in the DGB simulation does not significantly alter this spacing, and gap jet behavior remains relatively independent of wall influences, as the jets are contained within the separated wake region.

Qualitative comparison of the integrated aerodynamic loads between these two different parachute geometries is made possible by scaling the aerodynamic coefficients of the DGB by a factor of 0.333 and is shown in Fig.4.6. Both C_A and missile-frame normal force coefficient ($C_{N,m}$) show trends of the same sign with respect to α_T, which suggests that the dynamics of the parachutes are not fundamentally different, despite their different geometries and the presence of walls for the DGB. Differences in the C_A trends are likely due to wind tunnel blockage and may possibly be corrected with derived blockage relations [85]. However, the missile-frame normal force coefficient ($C_{N,m}$) trend of the DGB parachute is notably weaker by approximately $79\,\%$ and may be due to the proximity of the wind tunnel walls at large pitch/swing angle (θ)/angle of attack (α). Rapid flow in the narrow gap between the wall and the windward side of the parachute induces low pressure on the outside surface of the parachute and might diminish the restoring pendulum moment typically created by the leeward shed vortex in the wake (as seen for the scoop in Section 3.5), leading to a flatter $\frac{dC_N}{d\alpha}$ slope. The total error observed here includes additional inaccuracies due to geometry discrepancies, which are significant, so it is expected that the total effect of wind tunnel wall modeling should be less significant for a common parachute geometry.

A more directly-compatible comparison between simulations of an identical parachute geometry with and without wind tunnel walls is required to determine if this effect is truly due to the influence of the walls or instead dependent on another factor of the parachute geometry or freestream flow. Given the current data, it can be suggested that the most ideal comparison of CFD to wind tunnel conditions would include modeling of the wind tunnel test section walls, but that broad dynamic stability trends should still be recoverable in the free-air model.

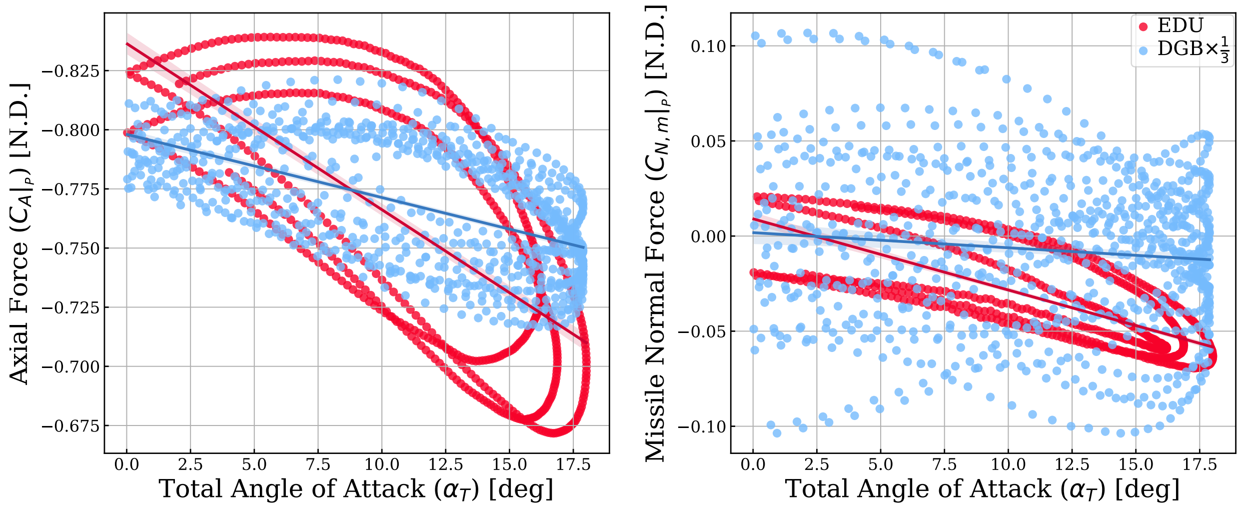

Figure 4.6: Loads comparisons between free-air Orion EDU and walled-in DGB parachute pendulum CFD simulations, where DGB aerodynamic coefficients are scaled to present a better comparison of dynamic stability trends

4.3.5 Turbulent Wake Modeling

All prior moving parachute simulations in this work utilized a URANS turbulence model, which does not resolve the full spectrum of turbulent length and time scales in the parachute wake. Though URANS has proven to be effective in specific applications of bluff-body wake modeling, especially for cases where boundary layer separation locations are geometrically determined and thus accurately predicted [61, 62] as with the sharp-edged parachute skirt, it is essential to the current research to investigate the effect of higher-fidelity turbulence modeling strategies, as discussed in Section 1.2.3.

Realism of the URANS turbulence modeling of the bluff-body wake was assessed by comparison to a simulation with DES turbulence modeling of the DGB parachute inside the wind tunnel test section. Fig. 4.7 compares the fidelity of turbulence modeling in the wake between URANS on the left and DES on the right. The URANS wake is characterized by large, coherent turbulent structures such as the smooth, separated shear layer, the vortex spilling out of the parachute skirt during the downward swing in the bottom-most image of Fig. 4.7a, and the strong jets shed from the vent and porosity gap. The DES wake reflects these primary URANS features but is additionally composed of many more fine turbulent structures and is more three-dimensional in nature. The porosity jets also tend to more quickly dissipate by destructive interference with wake turbulence, and their more-unsteady nature causes interaction with the lip shear layer, disrupting its smooth propagation downstream. Still, the bulk shapes of the bluff-body wakes in each simulation are relatively similar at any given time, which translates into acceptable comparison between the instantaneous aerodynamic loads plotted in Fig. 4.8.

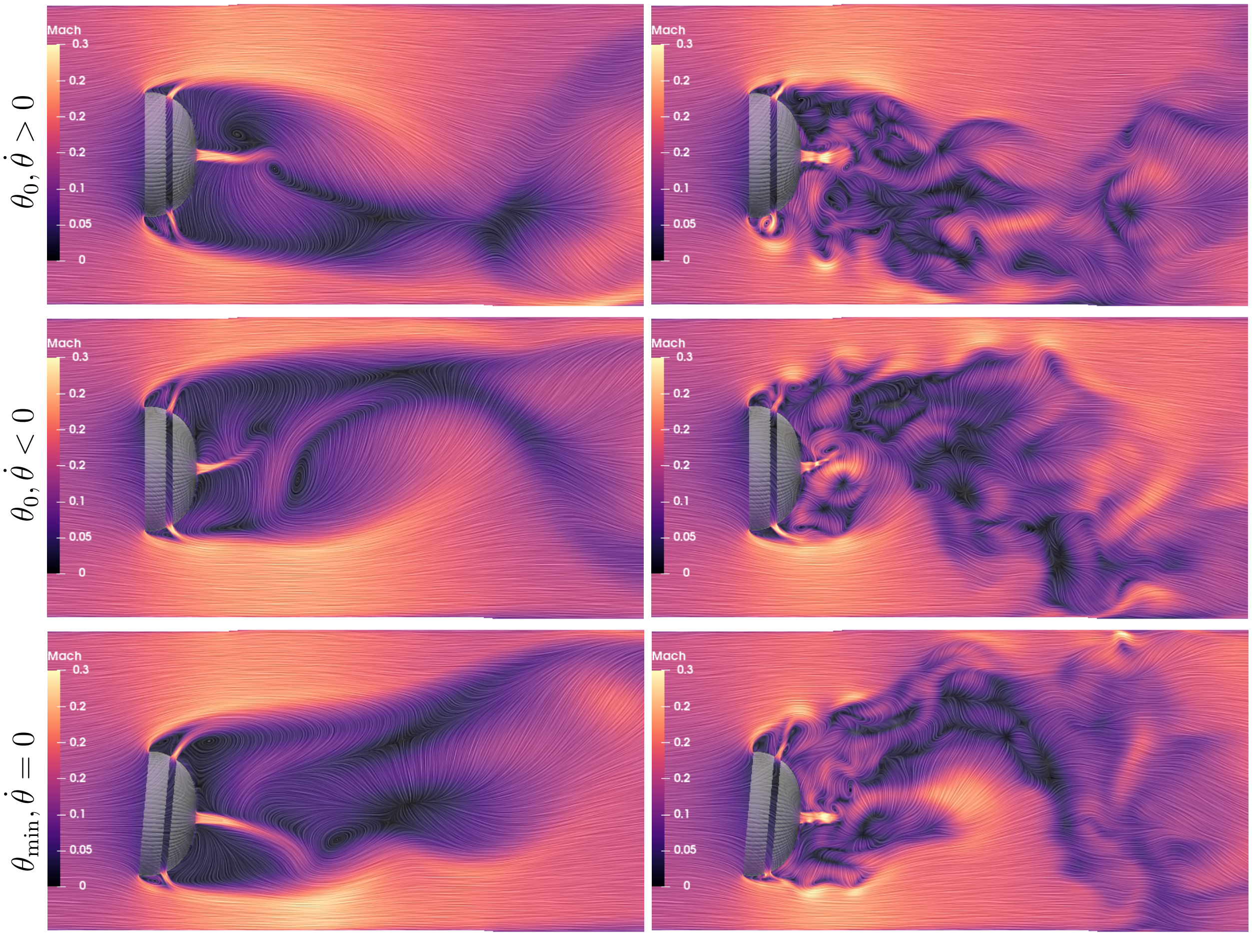

(a) URANS **(b)** DES

Figure 4.7: Instantaneous wakes generated by prescribed motion, swinging parachutes simulated using various turbulence modeling techniques

The $\frac{dC_A}{d\alpha_T}$ trends of both cases have nearly identical slopes, with the DES case incurring an approximately $1.25\,\%$ larger drag. The weak trend in $C_{N,m}$ previously observed for the DGB parachute is further diminished by DES turbulence modeling. In the bottom image of Fig. 4.7b, the equivalent of the URANS leeward vortex is decimated by interaction with the gap jet and turbulence decay, which might result in a loss of restoring moment. Additionally, the windward gap jet is seen to interact with the skirt shear layer for the DES case, a complex effect that could act to further diminish

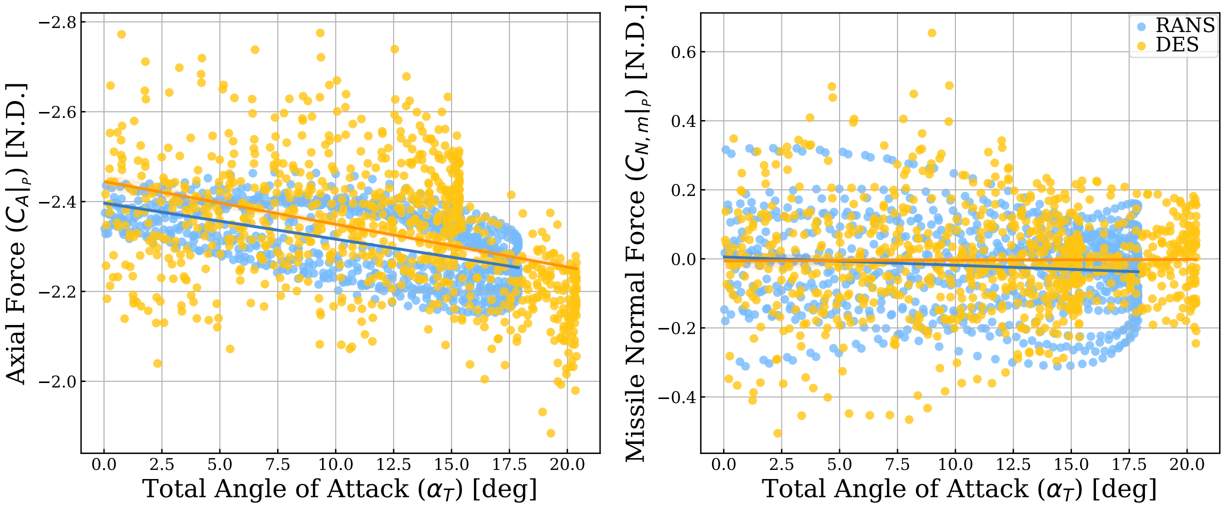

Figure 4.8: Loads comparison of DGB parachute in NFAC $80'$x$120'$ test section using URANS and DES turbulence modeling

the restoring pendulum moment.

These findings imply that increased realism in the details of the flow physics can be obtained from DES turbulence modeling, but that the bulk unsteady behavior of the parachute is acceptably modeled with URANS. No modifications were made to the computational domain for the DES simulation, so further insight might possibly be gained by globally refining the wake-capturing box grid or applying Adaptive Mesh Refinement (AMR) and also repeating the time step sensitivity study to uncover any additional unsteadiness.

4.3.6 Conclusion

This section investigated the sensitivity of the Orion EDU parachute pendulum simulation to grid cell and time step size as well as various approximations made in the model. Parametric variation of simulation parameters demonstrated that scaling of the fully-turbulent wind tunnel-scale Re to flight Re does not fundamentally alter the aerodynamic characteristics of the moving parachute. The effect of modeling wind tunnel walls was shown to be potentially significant but that generally similar dynamic stability trends are also observed in free-air simulations. Improved fidelity turbulence modeling in the form of DES was shown to augment the parachute dynamic stability trends, but not to change them fundamentally, indicating that DES introduces greater realism to the simulation, but that URANS provides a reasonable approximation of the unsteady wake.

These conclusions lend confidence to the validity of the approximations made in Section 4.2.1 and suggest that comparable aerodynamics to the WTT should be produced with a prescribed motion, flight-scale, free-air, URANS simulation of the Orion EDU parachute.

4.4 Model Validation

4.4.1 Comparison to Wind Tunnel Test

With the CFD model calibrated and simplifications tested, it was time to validate the computational results by comparison to the NFAC wind tunnel test data. As discussed in Section 4.2.4, a direct-comparison CFD simulation to the sub-scale WTT was achieved by prescribing the Orion EDU parachute grid to a planar swinging motion equation derived from the two primary frequencies of the observed WTT motion. Filling out the slow, meandering track of the WTT motion in simulation was computationally expensive and required upwards of $150\,000$ time steps and $134\,000$ CPU hours to complete. Figure 4.9 compares the dynamic motion and resulting aerodynamic loads of the simulated parachute to the data recorded in the WTT. The left image demonstrates the dynamics resulting from the θ motion fit equation of the prescribed CFD in terms of α_T and rate of angle of attack ($\dot{\alpha}$). Though the motion tracks are similar in shape and trend, the CFD pendulum does not achieve as great of magnitudes of α_T, which emphasizes the nonlinear relationship between the parachute swing attitude that was observed and approximated in the prescribed motion equation and the resulting aerodynamic parameters. The multi-dimensional nature of the WTT motion is likely the primary reason for these differences. In the test, the parachute achieved larger angles of attack than the CFD motion fit and almost always maintained an $\alpha_T > 0$ due to its precessing motion, while the CFD pendulum would come to a clean stop ($\alpha_T = 0$) at the apex of each swing. Precession also accounts for the additional noise seen in the WTT trajectory. Overall, however, the motion of the CFD simulation is sufficiently similar for the purposes of comparison, but even more compatible results could be obtained from a multi-DoF precessing motion fit.

The images in the middle and right of Fig. 4.9 present the trends of the body-frame axial and normal aerodynamic loads with respect to α_T. C_A compares remarkably well for URANS modeling of a dynamic, bluff-body wake, with only $1.08\,\%$ difference in the average magnitude and $< 10\,\%$ in slope. This is an excellent result, as drag is the primary performance metric of a parachute and its accurate prediction is essential for CFD model results to be useable in the parachute design process.

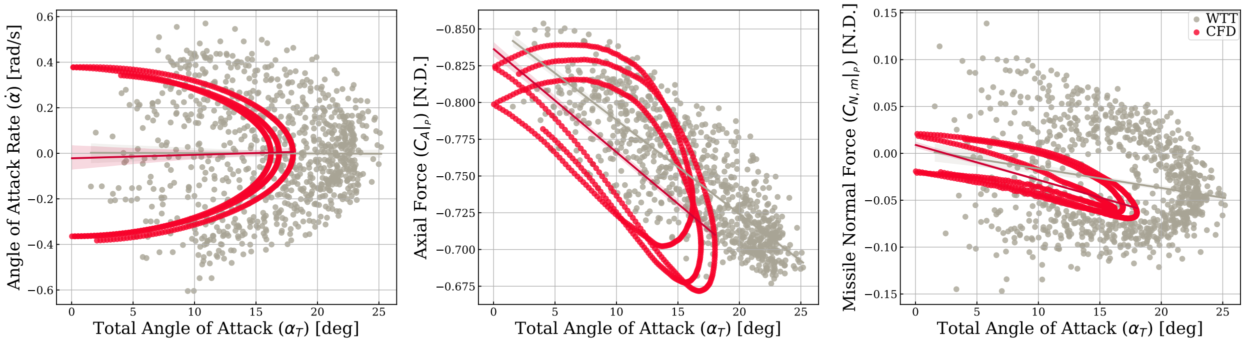

Figure 4.9: Comparisons between the Orion parachute NFAC wind tunnel test results and the parachute pendulum CFD model predictions

Differences in slope are due to a small divergence of the CFD trend at high α, which is likely due to the rigid modeling of the canopy geometry, which does not account for small deflation of the skirt area at larger angles. Fortunately, error in the CFD leads to under-predictions of dynamic drag, making the model overly-conservative, which is preferable to the alternative.

The stability-driving $C_{N,m}$ also compares reasonably well in average magnitude between cases, with a $13\,\%$ difference. Both the WTT and the CFD indicate that the EDU parachute geometry is dynamically stable ($\frac{dC_N}{d\alpha} < 0$), though the CFD model tends to over-predict the magnitude of this stability by approximately $69\,\%$ with linear regression slopes of $\frac{dC_N}{d\alpha} = -0.118 rad^{-1}, -0.200 rad^{-1}$ for the WTT and CFD, respectively. The differences in trend can be visually attributed to the bias of the CFD data to one side of the linear regression trend at higher α, which may be due to a combination of multiple modeling simplifications, including the lack of flexibility and porosity of the modeled parachute fabric, wind tunnel wall effects, which tended to decrease the C_N magnitude in Section 4.3.4, inadequately-modeled turbulent effects in the wake, especially at swing apexes, which also improved comparisons in Section 4.3.5, general inadequacies of the motion fit function, and, most significantly, reduced dimensionality of the planar CFD pendulum, which does not model the complex multi-DoF interactions of turbulent aerodynamic features.

The CFD model is also more accurate at recovering dynamic stability trends at lower-α ranges with $51\,\%$ difference for $\alpha \leq 15°$ and only $1.4\,\%$ difference for $\alpha \leq 10°$, which is an important result as this indicates that the model is capable of realistically assessing the root aerodynamic causes of pendulum motion initiation, which occurs at small α. Overall, the similarity between simulation and experiment is strong enough to support the assertion that rigid-body, high-fidelity geometry modeling of a moving parachute can produce unsteady aerodynamic loads of realistic magnitude and trend. It is expected that higher-fidelity modeling of the WTT parachute model trajectory, either through a more complex prescribed motion fit or aerodynamically-driven motion, would reduce the CFD model's error.

4.4.2 Comparison to Scoop Simple Parachute-Analog

It was also of obvious interest to compare the CFD parachute pendulum results to the scoop simple parachute-analog from Chapter 3 as an Aero6DOF simulation of a fully-3D, high-fidelity, parachute geometry precessing in multiple DoFs was outside of the scope of this work. Similar aerodynamic behavior between the two cases would support promoting the aeropendulum scoop from a simple GMP motion prototyping model to a surrogate for parachute dynamics modeling and design at a fraction of the computational cost.

Flow visualizations of the full-scale EDU parachute prescribed to track the WTT motion case are presented in chronological order swinging in a clockwise arc from maximum amplitude in Figs. 4.10a-4.10d and are compared to the flow surrounding the 2D planar and 3D precessing swinging scoops at an analogous condition in Figs. 4.10d-4.10f. The $y = 0$ flow slice shows the typical, prescribed motion, URANS results for a rigid parachute, with strong cylindrical and annular jets emitting from the vent and porosity gap and flagging with unsteadiness and the motion of the parachute. These flow phenomena are similar to those induced in the wake of the Disk-Gap-Band-design of the scoop.

The EDU ringsail near-wake is also influenced by many small annular jets emanating from the smaller gaps between the rings near the parachute apex. Unlike the 2D scoop and more similar to the 3D scoop, the 3D parachute wake does not exhibit unsteady, periodic Strouhal vortex shedding, and the separated shear layer leaving the parachute skirt grows at greater rate, even on the windward side. This creates a wider wake behind the parachute relative to its diameter that fully-encompasses the sub-flows from the porosity features. Like the scoop, large vortical structures are shed from the skirt of the parachute as it travels from maximum to minimum θ, but there are fewer interaction effects of these features with the weaker turbulent jets of this geometry, so their behavior with respect to the swinging motion is more reliably periodic in nature. Despite these significant differences in geometry and methods of grid motion, the overall similarity in the shapes of the wakes and semi-spherical shell geometries contribute to first-order similarity in flow features, which is reflected in

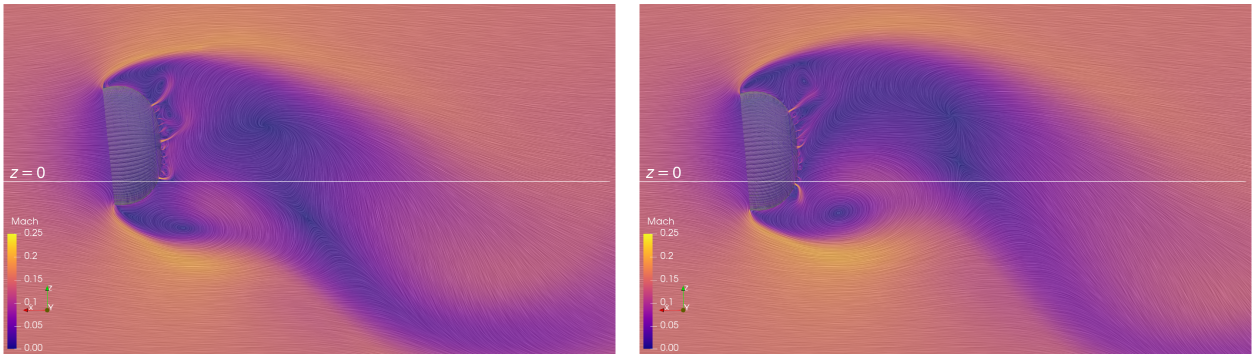

(a) EDU $\theta = \theta_{max} = 6.6°$ **(b)** EDU $\alpha = 0°$

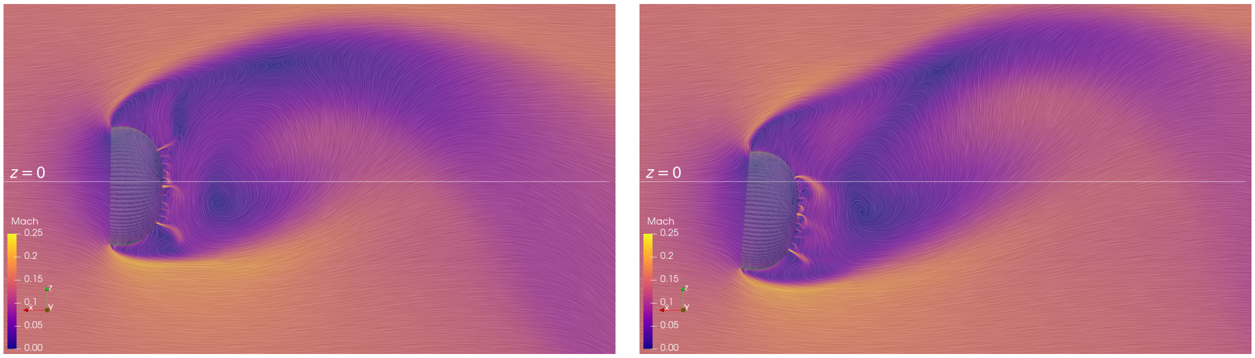

(c) EDU $\theta = 0°$ **(d)** EDU $\alpha = \alpha_{max} = 13.7°$

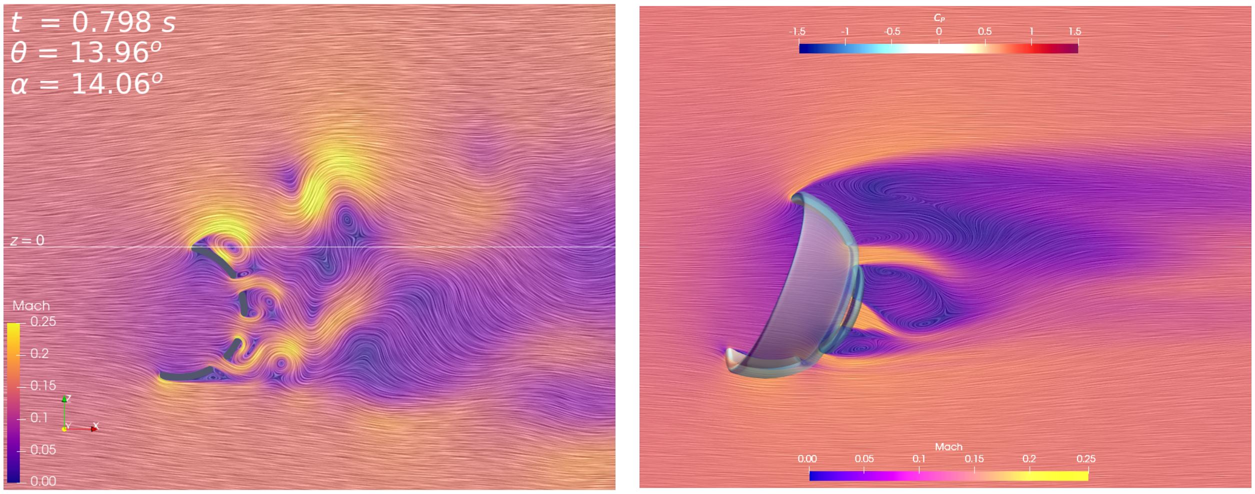

(e) 2D Scoop **(f)** 3D Scoop (2-DoF trim)

Figure 4.10: Instantaneous $y = 0$-plane Mach contours and momentum streamlines of the full-scale, Orion EDU parachute at $M = 0.15$ ("WTT-Track") swinging clockwise from maximum positive amplitude (labeled in chronological order (a)-(d)) and of the 2D and 3D scoop simple parachute-analog geometries at maximum swing amplitude, for comparison

the integrated aerodynamic loads shown in Fig. 4.11.

Figure 4.11 also compares the aerodynamically-driven motion of the scoop to the prescribed track of the CFD EDU parachute. The 2D scoop swings at a significantly higher frequency and amplitude and has a correspondingly larger magnitude of α than the prescribed parachute, but is similar in trend, while the 3D scoop motion is significantly skewed, which is likely due to minimal motion at low α and a damping oscillation about non-zero α. Despite the dissimilarities in motion, the scoops maintain the same aerodynamic load trends as observed for the WTT and prescribed motion parachute simulation. In particular, the slope of C_A for the 2D scoop compares well, though its incurred drag is approximately $30\,\%$ greater in magnitude. Both scoops also tend to indicate stronger dynamic stability than the parachute, with $\frac{dC_{N,m}}{d\alpha_T} = -0.506rad^{-1}, -0.360rad^{-1}, -0.200rad^{-1}$ for the 2D scoop, 3D scoop, and CFD EDU parachute, respectively. The greater-than-factor-of-two difference between the 2D scoop and the parachute may be partially related to the divergent swing transient motion mode experienced by the 2D scoop. However, considering the significant differences between geometries (complexity and number of dimensions) and motion (prescribed, small angles versus aerodynamically-driven transient swings), it is a positive and useful result that the signs of the stability trends are the same and that the slopes are on the same order of magnitude.

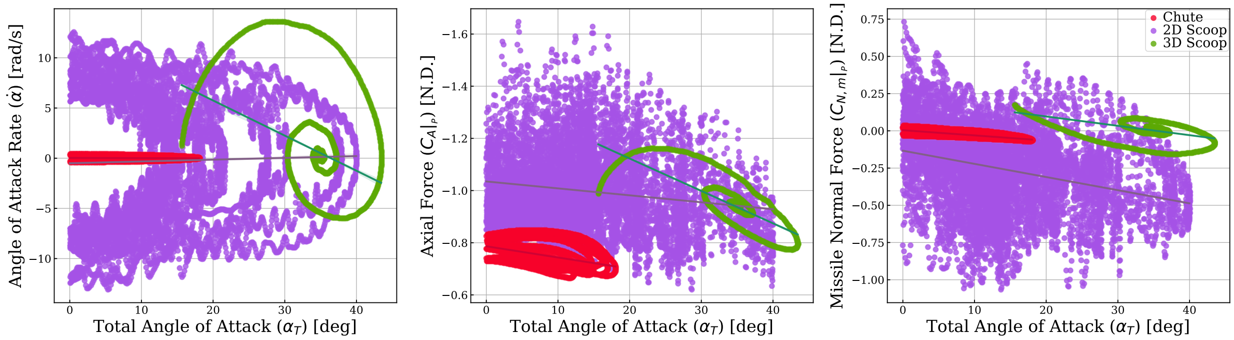

Figure 4.11: Comparison of periodic, aerodynamic loads modeled by the Orion EDU parachute prescribed motion CFD model to the aerodynamically-driven "scoop" parachute-analog simulation

It would be of great interest to apply the aerodynamically-driven pendulum methodology to the high-fidelity parachute geometry to assess if this difference in trend is due to the geometry and flow condition variations, or if constrained Aero6DOF motion is producing a fundamentally different result not modeled by the prescribed motion estimate. Overall, despite the highly-simplified nature of the scoop geometry and the minimized grid resolution of those simulations, the comparisons between 3D parachute and 2D simple parachute-analog are not dissimilar, enough so that the dynamic stability trends of the scoop can be analyzed to gain insight into parachute dynamics and that the analog model might be useful for future applications of parachute design.

4.5 Summary

In summary, this analysis has demonstrated that the dynamic stability characteristics of a swinging parachute can be accurately modeled using URANS CFD with a rigid-body, high-fidelity geometry, overset grid model and satisfies the objectives of Research Aim II. Several assumptions and simplifications were required to enable feasible modeling of this dynamic system, and the acceptability of these approximations was demonstrated through parametric sensitivity studies. It was found that freestream flow conditions can be scaled as long as they remain in the incompressible regime with a fully-turbulent Reynolds number and that the $\overline{q}$ and prescribed pendulum motion are scaled proportionally to velocity. Wind tunnel wall effects and higher-fidelity resolved turbulence were found to have some effect on the results of the model, suggesting that incorporation of these additional complexities would provide even better comparison to experimental data. Comparable motion to that observed in the wind tunnel test was derived through Fourier decomposition and a 2-frequency, single-plane approximation of the 6-DoF, precessing WTT motion and was found to be acceptable for achieving comparable dynamic loads behavior within $2\,\%$ for $\alpha \leq 10°$ and with $1.08\,\%$ drag accuracy and $< 10\,\%$ accuracy in stability for all α, which should be improvable with Aero6DOF motion. It was also shown that the scoop simple parachute-analog exhibits dynamics that are notionally similar to the Orion EDU parachute model, with same-order trends and approximately $30\,\%$ difference in drag. These behaviors are similar enough this model might be used for initial prototyping of future parachute designs.

The next extension of this work would be to simulate the EDU parachute with aerodynamically-driven motion. Though the prescribed motion derived from Fourier approximation was sufficiently similar for validation by comparison, the selected motion track is inherently simpler than the true parachute motion observed in testing. More complex motion approximations could be derived, but the realism of this approach would never fully match the ability of an OVERFLOW GMP Aero6DOF-mode simulation. With confidence established in both the accuracy of OVERFLOW flow solutions for the Orion parachute and in the usage of constraints in GMP to model pendulum motion, the CFD process developed in this work is now a viable option for prototyping untested parachute geometries for the purposes of estimating dynamic stability trends and designing wind tunnel or flight experiments.

CFD will provide additional insight to traditional testing methods, primarily in its ability to map parachute dynamic responses to unsteady, turbulent flow effects induced by subtle features in the parachute design; features that can now be fine-tuned in an informed manner. Ideally, this will reduce the amount of wind tunnel and flight testing required to certify a parachute for a new vehicle and also lead to new innovation in fundamental parachute design.

Further improvements to this model could be obtained by further relaxing the approximations made in Section 4.2.1. Improved wake modeling using DES is an immediately available option for increasing the realism of the simulation. More significant improvements would involve implementing a fabric porosity boundary condition to emulate the permeable nature of parachute fabric and to introduce Fluid-structure Interaction (FSI) methods, beginning by relaxing of the rigid tether constraint in order to allow motion damping along that axis and then improving to a periodic, prescribed deformation of the parachute canopy itself to emulate the “breathing” expansions and contractions a fully-inflated parachute can be subject to.

Chapter 5

Aerodynamic Pendulum Stability Analysis

In this chapter, the aerodynamic pendulum CFD model developed in Chapters 3 and 4 will be applied in a dynamic stability analysis to demonstrate its utility for parachute design, in accordance with Research Aim III. An extensive stability analysis of the specific Orion Engineering Design Unit (EDU) parachute geometry was previously performed in various research efforts using both analytic methods [26] and wind tunnel [13], static CFD [18], and flight data [15]. Additionally, Section 4.4.1 demonstrated that the moving-mesh CFD model of the EDU parachute developed in this work produces analogous results to the other studies of the same geometry. Therefore, the stability analysis in this chapter will focus on the two-dimensional, aerodynamically-driven scoop from Section 3.5 in order to take advantage of the rapid turnaround between runs for this prototyping model and to gain insight into a previously-unanalyzed, excessively dynamic aeropendulum system.

The stability analysis of the scoop will consist of an assessment of the static stability, after which a dynamic stability increment will be computed to demonstrate the magnitude of dynamic effects in this system. Then, a parametric study of geometric porosity variations is also performed to highlight the ability of this Aero6DOF model to predict motion responses of untested geometries and assess their estimated dynamic stability and performance.

5.1 Stability Analysis

Parachute static and dynamic stability is characterized by the body pitching moment coefficient (C_m) about the parachute centroid and normal force coefficient (C_N), which creates a moment about the tether anchor location, driving pendulum motion. For a bluff-body parachute, $C_m \propto C_N$, so the analysis of only one of these parameters is sufficient for characterizing pendulum stability [14]. In the parachute reference frame ($|_P$), which is depicted in Fig 5.1 and is rotated $180°$ about the body pitch axis Y_b relative to the stability axes reference frame used for the scoop aeropendulum analysis in Fig 2.1, a positive body C_m tends to effect an acceleration that increases the pitch/swing angle (θ) and angular velocity ($\dot{\theta}$). Thus, for a parachute to be considered statically stable, which is defined as "returning to its equilibrium position when it is displaced from its equilibrium position" [14], increases in θ, which generally correspond to increases in angle of attack (α), must tend to decrease C_m. This assertion provides the stability criterion:

$$\frac{dC_m}{d\alpha} < 0 \tag{5.1}$$

A configuration that is statically stable will exhibit this criterion for a steady-state and small disturbances. In contrast, a parachute is considered dynamically stable if "its aerodynamic forces and moments decrease the amplitude of each succeeding oscillation toward zero or to a small steady-state amplitude" [14]. This indicates that dynamic stability must be assessed in a time-dependent manner, and that complete damping of oscillations is not a strict requirement for parachute dynamic stability, as tethered, bluff-body objects tend to be pendulous by nature and that the focus of design is, instead, to reduce the magnitude and intensity of these oscillations as much as feasibly possible.

While Eqn. 5.1 will be the primary design criterion for a stable geometry, the scoop is a direct analog to a parachute, so relative drag performance between designs will be a close, secondary consideration, as this parameter defines the design's performance as a decelerator. As detailed in Section 2.4, analyses of the stability criterion are performed with transformed reference parameters to account for precession and rolling of the axisymmetric geometry. Thus, the following discussion will consider the total angle of attack (α_T), defined in Eqn. 2.10, which consolidates α to a single plane for any given side-slip angle (β), and the missile-frame pitching moment coefficient ($C_{m,m}$), which eliminates differences in comparisons of axisymmetric geometries due to roll or precession by rotating the reference frame about the aerodynamic clocking angle (ϕ_c), defined in Eqn. 2.11.

5.1.1 Static Stability Analysis

The stability analysis will begin by considering the static stability of the scoop from Section 3.5.1. For a design to be dynamically stable, it must also be statically stable, so this is an important assessment to make during the initial design process. Static stability data is also easier

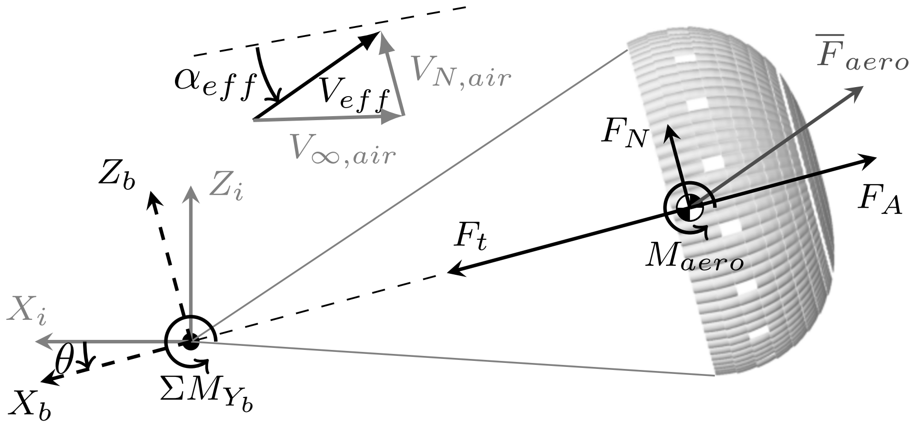

Figure 5.1: Free-body diagram for a parachute swinging counter-clockwise with a negative $\dot{\theta}$ (all velocities shown are of the relative air)

to obtain than dynamic stability data, as it does not require movement of the geometry and can be collected for a fixed model in wind tunnel and CFD tests. For this reason, aerodynamic databases are primarily constructed from static data, and dynamic stability is accounted for by applying an increment to the database derived from an often-one-off dynamic flight test, tethered or prescribed motion wind tunnel test (WTT), or, as in this study, from a moving-mesh CFD simulation. The analysis here will follow a similar process: first assessing the baseline static stability of the design and then determining how the dynamics increment this behavior, if at all. An ideal design would be statically stable, and dynamic tests would produce no increment to the stability assessment.

For the static stability analysis, the 2D scoop was simulated at discrete, fixed α. Each solution was allowed to converge, and unsteadiness of the oscillating wake was quantified by averaging the aerodynamic loads over a representative time interval and reporting the variance within this window about the average value. Such results are presented in Fig. 5.2, where the black circles represent average values for the stationary scoop loads and the vertical bars indicate the variance. The figure also presents the unsteady loads of the equivalent swinging scoop, for comparison.

Observing the general trends of the static loads with respect to α_T, it is clear that multiple stability modes exist at different levels of α_T, and a sharp discontinuity in stability at $\alpha_T \approx 7°$ is readily apparent. The modality of the static stability behavior, combined with significant unsteadiness for this geometry and flow condition, apparent from the variance bars, motivated a piecewise, least-squares regression, polynomial fit of the data. For the design of each curve fit, iterative changes of the α_T-interval and polynomial order were made and the optimal fit was selected based on residual minimization. Curve fits are a common practice for aerodynamic experimental analysis and for database design as they provide smooth derivatives for statistical dynamics simulations and control algorithms. Both $C_{m,m}$ and axial force coefficient (C_A) in Fig. 5.2 exhibit a linear region at low-α and a nonlinear region for α after the discontinuity, so a linear regression was applied at low-α and the nonlinear region was fit with a cubic polynomial. For simplicity, linear interpolation was used to bridge the two functions. In a production design of this parachute-analog scoop, higher-order fitting and smoothing techniques would be utilized to produce a more exact and robust representation of the data, however, the current methods are sufficient for the purposes of this demonstration. The resulting polynomials are also plotted in Fig. 5.2 and their equations are:

$$
\begin{aligned}
C_A(\alpha_T \leq 6^\circ) &= 0.0148\alpha_T + -0.8778 \\
C_A(\alpha_T > 6^\circ) &= -0.0184{\alpha_T}^2 + -0.8536 \\
C_{m,m}(\alpha_T \leq 4^\circ) &= 0.0230\alpha_T + -0.0098 \\
C_{m,m}(\alpha_T > 6^\circ) &= -0.1240{\alpha_T}^3 + 0.0056{\alpha_T}^2 + 0.4204
\end{aligned}
\tag{5.2}
$$

where secondary-order coefficients are omitted for simplicity.

Using the polynomial approximations for $C_{m,m}$ to guide the static stability analysis, it can be determined that the 2D scoop is statically unstable $\left(\frac{dC_m}{d\alpha} > 0\right)$ for low α, then, the scoop discontin-

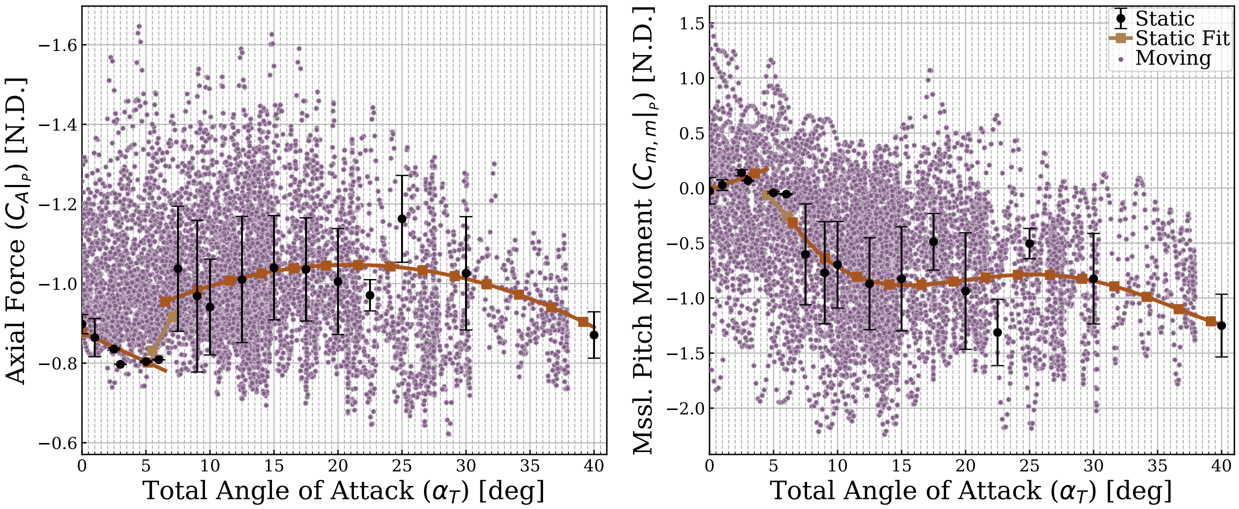

Figure 5.2: Unsteady aerodynamic loads induced on a 2D scoop at fixed angle of attack (represented by an average value bounded by the standard deviation over the averaging interval), piecewise, least-squares regression, polynomial curve-fits of the static data, and unsteady loads for an analogous, swinging scoop

uously becomes statically stable for $5^\circ \lesssim \alpha_T \lesssim 15^\circ$, then weakly unstable at higher α, and finally stable again for the largest α. Small α instability is likely attributable to vortex shedding on either side of the 2D skirt, which tends to oscillate the pendulum away from a stable equilibrium and was determined to be the root cause of pendulum motion of parachutes from the Orion EDU testing campaign [15]. As α increases, the flow around the nonmoving geometry steadies and the influence of the off-body vortices diminish, but the offset of the symmetric body tends to induce a destabilizing, positive C_m. Then, a discontinuity in stability response occurs at $\alpha \approx 7^\circ$ and corresponds to the normal-alignment of the scoop's porosity gap with the freestream direction, which can be observed in Fig. 3.17d. It is possible that this alignment is further enhancing the geometric porosity of the scoop by increasing the frontal area of the gap with respect to the flow direction and is alleviating the C_N and C_m that typically result from the pressure of cavity-trapped air acting on the back of the canopy. Indeed, a step-change in C_A occurs at this angle, which indicates a reduction in cavity pressure. However, at almost the same instance as this alignment, the angle of the canopy is such that spillage of high-pressure air over the lip of the skirt resumes, generating strong, off-body vortices that create a restoring moment for the pendulum. Correspondingly, the scoop transitions into a statically stable mode for moderate α. At larger $\alpha_T \approx 20^\circ$, a weak negative static stability occurs and is likely due to an increasing alignment of the body normal direction Z_b with the freestream flow and a corresponding decrease in the cavity pressure and strength of shed vortices. At the highest α, the scoop is unconditionally stable as its normal direction is nearly-fully align with the freestream, and almost all induced pressure force served to create a restoring pendulum moment. The direct insight into the aerodynamic cause of these stability behaviors is the distinct advantage of the CFD analysis technique presented by this work. For a real design process, identification of this coincidental gap alignment in simulation might give the designers sufficient information to reiterate the geometry with a more optimal porosity gap location before testing, avoiding the additional cost of repeated experiments.

Comparing the static loads in Fig. 5.2 to the moving scoop, we see that some of these static stability modes are potentially well-emulated in the dynamic response, especially at higher α. This is logical, because the dynamic scoop is moving at lower relative velocities at high θ, when large α occurs, so the flow should be more similar to the stationary equivalent. Indeed, the weak instability at medium α and strong stability at large α serve well to explain the transient swing behavior observed for the scoop when momentary randomness in the flow allowed the geometry to enter the weakly-correlated region and continue swinging out to high angles before returning and eventually restoring into the stable region below $\alpha < 15°$. However, at lower α, there are obvious bias-differences between the stationary and moving loads. It is the ultimate merit of this work's CFD pendulum model to be able to predict dynamic stability characteristics, so the following section will discuss these differences further.

5.1.2 Dynamic Stability Analysis

In this section, the dynamic stability of the 2D scoop is analyzed and compared to its static stability in an incremental fashion, where to total aerodynamic coefficients are decomposed as:

$$C_{tot} = C_{stat} + C_{dyn} \tag{5.3}$$

The coefficient increment due to dynamic effects (C_{dyn}) serves as a clear indicator of where in the flight space dynamic stability effects are most significant $(C_{dyn} \gg 0)$ and also emulates how Aero6DOF data would be enfolded into an existing flight database constructed from static WTT and CFD data. In this analysis, C_{dyn} is computed by differencing the total aerodynamic loads of the moving case (C_{tot}) in Fig. 5.2 with the piecewise polynomial fit of the static loads (C_{stat}) for the same scoop at fixed angles. The result is the dynamic increment distribution in Fig. 5.3, which is compared to the static increment for reference. Like the static results, the dynamic loads increment was fit with a polynomial using least-squares regression, which is also included in the figure. In these instances, a single, continuous polynomial was sufficient, with a parabolic and cubic fit serving best for C_A and $C_{m,m}$, as shown below:

$$\begin{aligned} C_A(\alpha_T) &= 0.0211x^2 + -0.2279 \\ C_{m,m}(\alpha_T) &= 0.0368x^3 + -0.0017x^2 + -0.1763 \end{aligned} \tag{5.4}$$

Observing the stability-relevant dynamic increment $C_{m,m}$ first, it can be determined that dynamic stability does have strong effects on the trajectory of the scoop at certain portions of the pendulum's swing. Dynamic $C_{m,m}$ is of greatest magnitude at low α and the slope in this region indicates that the scoop is dynamically unstable at small angles in addition to being statically unstable. This explains why the 2D scoop was subjected to periodic oscillation and did not damp to a stable, centerline equilibrium. As previously stated, this is likely due to strong side forces from the

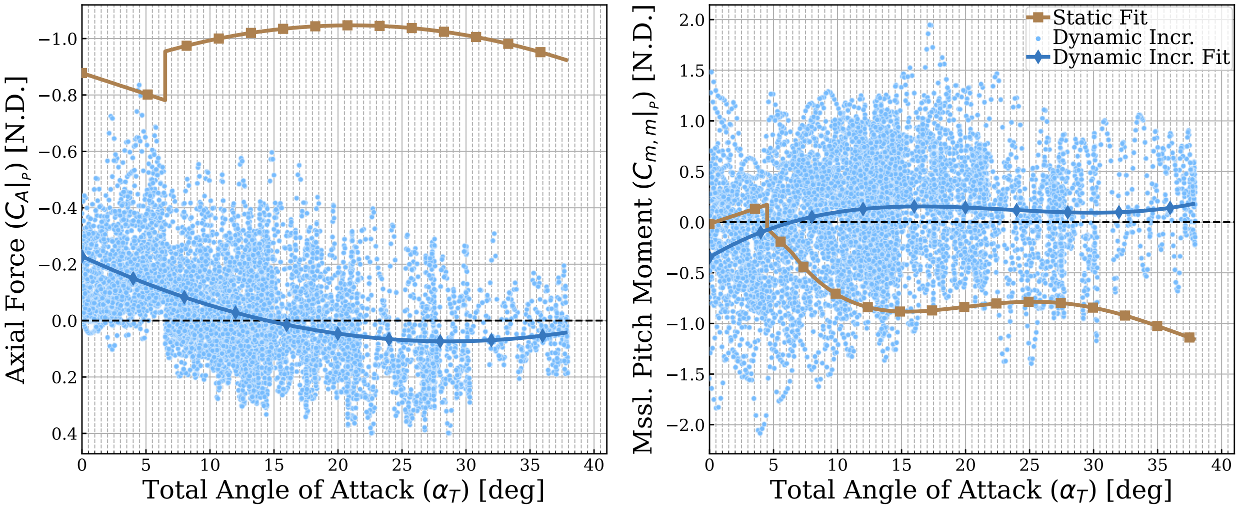

Figure 5.3: Static and dynamic stability increments for a 2D scoop, fitted with piecewise polynomials

vortices shed on both sides of the scoop at low α. The discontinuity at $\alpha_T \approx 7°$ does not distinctly affect the dynamic stability behavior of the scoop and is likely due purely to the alignment of the geometry features discussed in the previous section. At medium and high α, dynamic effects are minimal, incrementing the loads slightly, but not altering the stability characteristics (the minor, dynamically unstable trend at the highest α is an extrapolation artifact of the polynomial fit and could be improved with a more sophisticated curve-fit). Some augmentation of the drag (C_A) is also attributable to dynamic effects and is strongest at lower α, with an approximately $25\,\%$ drag increase that diminishes parabolically to zero at $\alpha_T \approx 20°$. This drag increase may be due to the augmentation of α by effective velocity (V_{eff}) at low θ, when the body axial direction (X_b) is aligned with the flow, resulting in large C_A. Though dynamic drag increase should not be relied upon as a design factor (increased declaration performance does not justify a preference for unstable pendulum motion), it increases the conservatism of the design rather than diminishing drag performance margins.

Overall, the scoop is dynamically unstable at small α, which exacerbates its static instability at these conditions, but is otherwise dominated by static stability trends for most flight α. Unfortunately, the instability of the design at small angles is a significant flaw for an aerodynamic decelerator, so the recommendation resulting from this analysis would be to redesign the scoop to improve small-angle static and dynamic stability. Fortunately, this work provides a methodology for rapidly prototyping parametric variations of the scoop geometry considered here in order to determine more stable designs, and an example of this process is found in the next section.

5.2 Parametric Stability Design

In this section, a comparison between multiple geometry variations of the scoop parachute-analog are compared to demonstrate the utility of the OVERFLOW CFD pendulum model as a stability design tool. Developing a dynamically-optimized scoop was not an aim of this research, so the following designs do not drive towards a superior choice, but simply exemplify how changes to the geometric porosity of a drag body can alter its dynamic stability. Geometric porosity tends to increase the stability of a parachute design by allowing flow through the aft of the parachute, reducing the pressure inside of the parachute cavity and the strength of the ring vortices shed from the canopy skirt that are the source of instability [14].

The baseline scoop geometry discussed throughout this work was constructed in the manner of a Disk-Gap-Band (DGB) parachute with a central vent of $11\,\%$ geometric porosity and a single porosity gap of equivalent size, bringing the total geometric porosity of the shape to approximately $20\,\%$. This geometry is visible as the purple cross-section in Fig. 5.4a, where the porosity gap is two separate openings on either side of the vent for a 2D geometry. A subset of the other geometric porosity variations of this design considered in this study are also depicted in Fig. 5.4a, and are identified by their geometric porosity as a fraction of the baseline value. In addition to independently varying the size of both the vent and gap, some geometries omit the gap entirely, resulting in a open-back cross-section representative of an annular parachute design. All of these geometries were simulated as Aero6DOF-mode pendulums at the same 2D conditions, and their resulting trajectories are presented in Fig. 5.4b. It is also worth noting that the simple design of the DGB parachute is best-suited to supersonic flow conditions, such as Mars Entry, Descent, and Landing (EDL), so the simulations of this geometry at subsonic Mach number (M) in this study result in inherently oscillatory motion.

Dynamic stability of each system is assessed through phase plane analysis in $\dot{\alpha}$-α-space, which allows intuitive assessment by proportional representation of the pendulum swing angle magnitude (α/x-axis) and the swing rate (rate of angle of attack ($\dot{\alpha}$)/z-axis). An unstable parachute, whose aerodynamic forces and moments tend to increase oscillatory angles and rates, traces an outward spiral, diverging from its equilibrium. This behavior is observed for the annular parachute (no porosity

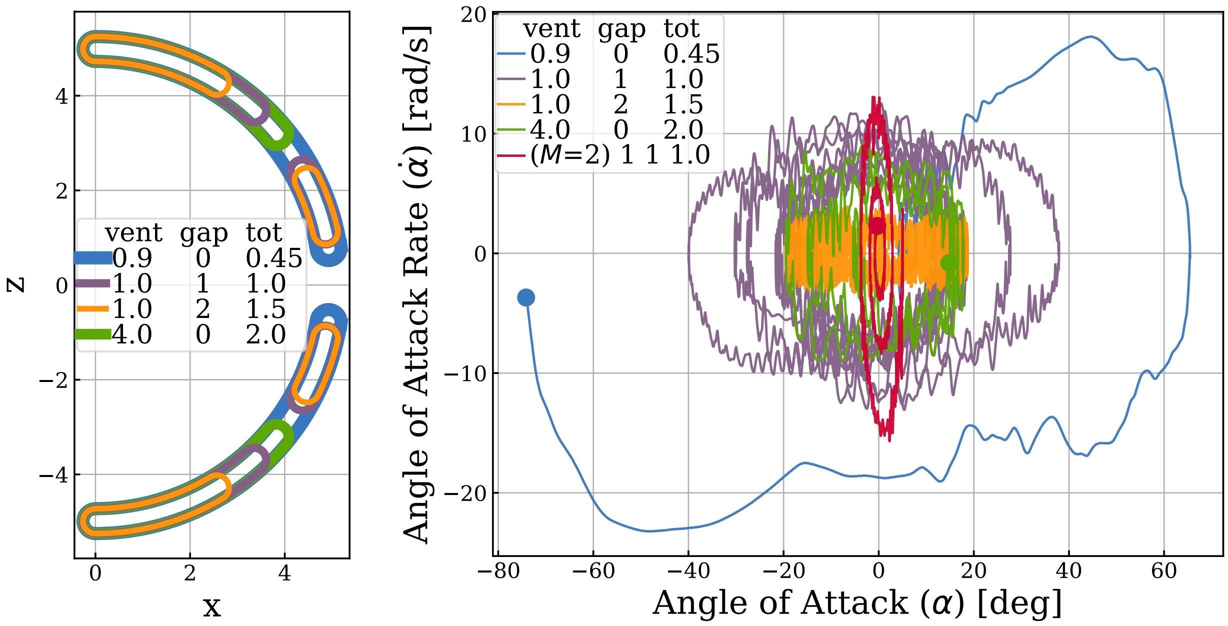

(a) Various 2D scoop geometries, where geometric porosity is listed as a fraction of the baseline value

(b) Rate of angle of attack-angle of attack phase plane comparison of various 2D scoop designs, where the end of each trajectory's time interval is indicated with a circular marker

Figure 5.4: Dynamic responses of 2D scoop geometries with various amounts of geometric porosity

gap) with baseline vent size (blue), which has half of the total geometric porosity of the baseline case and is subject to correspondingly stronger vortex shedding. Conversely, a stable parachute that damps all swinging disturbances follows a downward spiral that ends at a single point on the phase plane, as is exhibited for the supersonic M case in red in Fig. 5.4b, which is the baseline scoop simulated at the intended design conditions for a DGB parachute.

A parachute undergoing pendulum motion traces out a repeatable, closed track as it swings back and forth, resulting in a stable limit cycle. This is demonstrated by the baseline 2D scoop run, plotted in the same color (purple) as previous sections. In Fig. 5.4b, this case traces a closed, roughly oval trajectory in $\dot{\alpha}$-α-space, maintaining an average $\alpha \approx 20°$ while cycling in $\dot{\alpha}$. Geometries that have a tendency for pendulum motion will attract to this limit cycle, regardless of initial motion condition. The divergent, transient swing of the 2D scoop, observed in Section 3.5.1, is an example of this "attractor" nature, where a momentary disturbance causes the trajectory to deviate from the repeated oval shape, but the trajectory returns to its "stable," swinging state in less than one cycle. Improvements in dynamic stability can be visualized as reductions in the area of these closed contours, which corresponds to reduced swing angles and rates. This occurs relative to the baseline case for the DGB variation with a twice as large gap, whose orange phase plane trace is a tighter oval, with reduced rate of swing.

In addition to assessing improvements in dynamic stability, a full parachute design process must also be a trade study that focuses on retaining the desired drag performance of the decelerator, as this is the primary performance metric of a parachute. Because geometric porosity tends to improve stability while reducing drag, these two metrics are inversely proportional, and an optimal design process will seek to find the ideal compromise of acceptable deceleration with stable dynamics. For the scoop geometries considered in this research, this trade study is represented in Table 5.1, where the decelerator performance is quantified by the average drag coefficient (C_D) throughout a pendulum's trajectory and the dynamic stability is indicated by the absolute average values of the aerodynamic angle and angular rate, which should be minimized for ideal dynamic stability performance. The inverse relationship between these design criteria is readily apparent in the table, with stark drag losses and reduced oscillation magnitudes for geometries with increased porosity. Not all porosity changes result in an equivalent effect, however, as is demonstrated by Designs 3 and 4, both of which have the same total geometric porosity, achieved by doubling the baseline size of the gap or vent, respectively. Despite their similar total porosity, Design 4 exhibits both superior drag <u>and</u> reduced swing angle magnitude to Design 3, indicating that the baseline subsonic DGB parachute design might be better-improved by increasing vent porosity over gap porosity. The table also indicates that the DGB design generally out-performs the annular parachute cross-sectional designs for this condition, as annular Design 5 has inferior drag and increased swing angle and rate compared to DGB Design 4, despite its increased geometric porosity.

In general, given the coarse granularity of this demonstration, none of the designs are a clear front-runner for ideal scoop performance, which highlights the complexity of the parachute design process and emphasizes the need for detailed analysis with advanced optimization techniques in the production approach for dynamic stability design. Fortunately, the CFD parachute pendulum motion model provided by this work is ideally suited for this process, as it provides rapid turnaround time between design iterations and trivial "construction" of new model geometries. Overall, this qualitative comparison demonstrates that the OVERFLOW CFD pendulum model predicts correct dynamic stability responses to parametric design changes based on known principles of parachute stability design [18, 15] and indicates that this form of parametric study can be utilized in production

Table 5.1: Trade study of deceleration performance and dynamic stability characteristics for various 2D scoop designs

		Porosity Fraction			Absolute Average		
No.	Style	Vent	Gap	Total	C_D	α	$\dot{\alpha}$
1	Annular	0.9	0	0.45	1.77	32.58°	11.72
2	DGB	1.0	1	1.0	1.03	14.36°	5.38
3	DGB	1.0	2	1.5	0.59	11.05°	1.10
4	DGB	2.0	1	1.5	0.73	8.77°	3.57
5	Annular	4.0	0	2.0	0.70	9.60°	4.24
6	Annular	5.0	0	2.5	0.46	10.1°	4.00

for more complex geometries such as the Orion main parachute.

5.3 Summary

This chapter demonstrated the use of the OVERFLOW CFD pendulum model for the purposes of dynamic stability design as the focus of Research Aim III. Unsteady aerodynamic loads from fixed and moving simulations of the same 2D scoop geometry were analyzed in terms of static and dynamic stability. The scoop was found to be statically stable at most swing angles experienced by parachutes in flight during deployment and after inflation $(5^\circ < \alpha < 15^\circ)$, but was statically unstable for small α. Dynamic effects compounded this instability, demonstrating that dynamics can also be a contributor to initiating pendulum motion. Finally, the CFD pendulum tool demonstrated its ability to assess relative stability performance by simulating various 2D scoop designs in order to observe limit cycle oscillations in motion phase planes.

Logical future applications of this tool and process might involve a true stability design of the scoop parachute-analog that utilized an optimization algorithm to produce the ideal geometry for maximum aerodynamic stability with desired drag performance. Aside from demonstrating the utility of this CFD model, the resulting design from this analysis might be better suited for realistically emulating parachute dynamics. It would also be of interest to simulate the Orion Multi-Purpose

Crew Vehicle (MPCV) EDU parachute in Aero6DOF-mode, and then perform a parametric study of geometric porosity and dynamic stability analogous to the static stability study by Greathouse and Schwing.

Chapter 6

Conclusion

A number of crewed space vehicles are currently in development and will rely on parachutes to decelerate and land safely on Earth. High-drag parachute designs can be inherently unstable, and in one- or two-parachute clusters, these instabilities can compound to introduce pendulum motion, creating a hazard for crew and cargo during an off-design touchdown. Fundamental understanding of the dynamics and aerodynamics of parachutes is essential to safely design these descent systems. Though the concept of the parachute has existed for centuries, recent developments in Computational Fluid Dynamics (CFD) and Fluid-structure Interaction (FSI) have provided new insights into the dynamics of parachutes. However, the majority of these computational models are exploratory and lack the rigorous testing that the aerospace industry requires for production tools.

This research has demonstrated that a rigid-geometry parachute CFD simulation with grid motion driven by the aerodynamics of the solution can combine the maturity of modern, industry-grade CFD solvers with a simplified representation of parachute pendulum motion to obtain acceptable, rate-dependent, aerodynamic data for the purposes of comparative dynamic stability design. Validation of these methods is essential for confident use in the industry and has been accomplished in the current study by direct comparison to wind tunnel data. The tool that resulted from this research was employed in a dynamic stability analysis of a parachute-analog geometry in order to demonstrate functionality and utility. This model provides the parachute industry with a method of predicting parachute dynamic stability characteristics at relatively low cost prior to more expensive wind tunnel and flight testing operations. It also provides the ability to simulate parachute aerodynamics at infeasible testing conditions like supersonic Entry, Descent, and Landing (EDL) into the atmosphere of Mars and to allow complex wake interaction analyses such the influence of the capsule tethered upstream of an inflated parachute [83] or a parachutist in the wake of a large cargo aircraft [88].

6.1 Summary

Several Aims were established at the beginning of this work to guide the research and are summarized as follows:

Aim I Develop and validate a CFD model of an aerodynamically-driven pendulum

Aim II Develop and validate a CFD model of parachute pendulum motion

Aim III Demonstrate model utility through dynamic stability analysis based on geometric porosity

This section summaries how these Aims were accomplished in the current research, emphasizes the effectiveness of the models developed by this work, and details the best practices determined by this study. Chapter 1: Introduction, explained the motivation for this work, gave a review of the literature in order to establish the need for this moving-mesh, rigid-body CFD parachute pendulum model, and provided an overview of previous parachute tests and analyses utilized for comparison to this work.

Chapter 2: Pendulum Modeling and Analysis Tools, gave derivations and descriptions of the software tools developed and utilized to simulate aerodynamically-driven pendulum motion. A drag coefficient-based, numeric, Ordinary Differential Equation (ODE) model of an aeropendulum was derived for comparison to the CFD pendulum model. The model assumed a constant drag coefficient (C_d) for a circular cylinder pendulum bob in order to derive a single governing equation for the 1-DoF system. The equation was placed into state space form and solved explicitly in a predictor-corrector fashion. Coordinate reference frames and common parameters for vehicle stability and aerodynamics utilized in this work were derived. Also provided was an overview of OVERFLOW's Geometry Manipulation Protocol (GMP) tool, which allowed grid motion during the CFD simulation driven by integrated aerodynamic loads and constrained about an off-body tether location. A dynamic aerodynamics post-processing Python software suite called `overdyn` was also developed as part of this work and its functionality and usage were described. This tool processes raw OVERFLOW aerodynamic loads and moving-body state parameter outputs to return a collected time history of the simulated object's dynamic and aerodynamic parameters in relevant coordinate reference frames. The tool also creates visualizations for assessing CFD simulation convergence and the analysis of aerodynamic loads.

In Chapter 3: Aerodynamic Pendulum CFD Model, a model of a simple, aerodynamic pendulum was developed in the OVERFLOW CFD tool, and validation of predicted motion accuracy was established by comparison to the numeric ODE aeropendulum model, satisfying the objectives of Research Aim I. The model was calibrated through sensitivity studies and by comparison to wind tunnel tests of stationary circular cylinders. Qualitative functionality of constrained, aerodynamically-driven motion in OVERFLOW was confirmed by simulating pinned, elongated geometries like a flat plate and a cylinder with a tab and observing that these geometries rotated, oscillated, and damped to a "feathered" neutral orientation aligned with the freestream flow. The accuracy and realism of the CFD pendulum model was quantitatively confirmed by direct motion comparison between a simulated circular cylinder pendulum and the drag-based, numeric ODE model from Chapter 2. Both models exhibited a damped oscillation of a similar magnitude and frequency of $f \approx 3Hz$, which is the expected result for a pendulum with aerodynamic drag opposing its swing. The CFD model motion was additionally subject to a secondary, high-frequency oscillation of $f \approx 48.2Hz$ superimposed on its primary swinging motion caused by the fluctuating, unsteady, bluff-body wake, which represents an additional level of complexity uncovered by the CFD model. A parachute-analog scoop geometry was also simulated to demonstrate the model's ability to predict trajectories induced by aerodynamically complex flows. This simulation exhibited a primary, periodic swing of $f \approx 5Hz$ and $\theta_{max} \approx 15°$, but was highly sensitive to random influences from the unsteady, turbulent wake and geometry flow features like the strong jet emitting from the porosity gap. Such influences combined to momentarily eliminate vortex shedding from the high-pressure cavity at non-zero angle of attack (α), and the resulting loss in pendulum restoring moment induced a transient, divergent swing of $\theta_{max} = 40°$ that was ultimately damped, after which periodic pendulum motion resumed. This example highlights the model's ability to uncover multi-modal, dynamical behaviors that are time-dependent and chaos-induced, which cannot be achieved using traditional stationary CFD or wind tunnel testing (or even prescribed motion CFD).

Three-dimensional flow and motion effects were also investigated with the scoop model. For the chosen conditions, the 3D wake was non-oscillatory and the selected geometry was observed to trim at an angle of 30°, even when free to rotate in 2-DoF, where the scoop exhibited a precession about its trim angle. At the trim angle, pitching moment coefficient (C_m) and normal force coefficient (C_N) reduced to zero and correspond to an alignment of the inboard edge of the porosity ring with the freestream flow.

In Chapter 4: Parachute Pendulum CFD Model, Research Aim II was achieved by developing and validating a CFD model of pendulum motion of the Orion Multi-Purpose Crew Vehicle (MPCV) Engineering Design Unit (EDU) parachute. The model was subject to simplifications and assumptions including a rigid canopy and tether, no fabric porosity, and Unsteady Reynolds-averaged Navier-Stokes (URANS) turbulence modeling. Applicability of these assumptions was assessed through sensitivity and parametric study and is addressed in the Research Questions section below. Best practices were established for both prescribed and Aero6DOF moving-body pendulum CFD simulation convergence stages as:

1. Stationary, steady-state flow initialization, at maximum swing angle
2. Stationary, time-accurate initial flow condition convergence
3. Motion initiation and dissipation of transients
4. Quasi-steady, periodic, pendulum motion

Stable and accurate motion predictions were facilitated by employing high-accuracy, implicit schemes combined with small time steps and a significant number of sub-iterations (20) to allow for maximum flow convergence at a given location before computation of coupled body motion. Simulations were designed to be analogous to the $35\,\%$-scale wind tunnel test (WTT) of the same geometry conducted in the National Full-scale Aerodynamics Complex (NFAC) $80'$x$120'$ test section. Comparisons to this test showed good agreement between trends and magnitude for unsteady aerodynamic loads as a function of α, validating the accuracy of the CFD pendulum model. Superior agreement could be obtained with a higher-order approximation of the WTT motion or an Aero6DOF motion simulation of the EDU parachute. Overall, it was shown that the dynamic stability characteristics of a swinging parachute can be accurately modeled with quantifiable uncertainties using URANS CFD with a rigid-body, high-fidelity geometry, overset grid model.

Finally, in Chapter 5: Aerodynamic Pendulum Stability Analysis, the utility of the model as a parachute design tool was demonstrated by performing a dynamic stability assessment of parametrically varied 2D scoop geometries, completing Research Aim III. For the baseline geometry, a static stability analysis of $\frac{dC_N}{d\alpha}$ revealed that the scoop was unstable at low α and stable for $5° < \alpha < 15°$, creating a tendency towards pendulum motion. At medium α, the scoop was weakly unstable and then stable again at the highest α, as demonstrated by the observed transient swing. Dynamic stability was computed as an increment and found to compound low-α instability, but to have a diminishing effect on static stability trends at higher α. Comparison of the relative dynamic stability of varied scoop geometries was achieved through rate of angle of attack-angle of attack phase plane analysis of the simulated trajectories and confirmed that increased geometric porosity from the baseline model tended to decrease the magnitude of but not to extinguish pendulum motion, while decreasing porosity resulted in dynamically unstable behavior. The inversely proportional relationship between optimal deceleration performance of a parachute-like geometry and its dynamic stability was also demonstrated and methods for analysis and optimization of this trade study utilizing this CFD pendulum model were proposed.

6.2 Research Questions

In preparation for this research, several questions arose and were asked in Section 1.3 in hopes that the model developed for this work would provide insight into these unknowns. They were:

1. Can rigid-body CFD with nonporous surfaces accurately model parachute pendulum aerodynamics?
    (a) Is self-similarity maintained when scaling from wind tunnel test conditions to flight?
    (b) Can the dynamic load trends of a parachute WTT be recovered in CFD simulation without modeling wind tunnel wall effects?
    (c) Is URANS turbulence modeling sufficient for recovering the bulk unsteady nature of moving, bluff-body wakes?
2. Is the root cause of parachute dynamic instability the same shed ring vortex that causes static instability?

3. Does CFD of moving bodies prescribed to a known motion track resolve aerodynamic responses as accurately as aerodynamically-driven motion?
4. Can the simple parachute-analog model be used as an accurate surrogate of true parachute aerodynamic response?

The answers to these questions were derived from the findings of this research and are presented in the following sections.

Can rigid-body CFD with nonporous surfaces accurately model parachute pendulum aerodynamics?

Yes. In direct comparison to wind tunnel test data (see Fig. 4.9), the CFD model developed in this work predicted average drag to within $1.08\,\%$, with $< 10\,\%$ under-prediction in trend, which bodes well for the model's ability to provide realistic performance metrics for parachute design. CFD modeling of dynamic stability trends was $1.4\,\%$ accurate based on $\frac{dC_{N,m}}{d\alpha_T}$ for small $\alpha \leq 10°$, which is useful for modeling the root cause of pendulum motion initiation. However, the simulation was less accurate ($13\,\%$ difference average missile-frame normal force coefficient ($C_{N,m}$), $69\,\%$ difference $\frac{dC_{N,m}}{d\alpha_T}$) when including the entire α-space observed in drop test pendulum motion. These uncertainties could be improved by prescribing simulated parachute pendulum motion with a more accurate fit of the WTT motion or with Aero6DOF motion, but are useable as-is for comparative studies of the relative dynamic stability of different parachute geometry designs. Overall, the current Orion EDU parachute pendulum motion CFD model can predict dynamic loads with as little as $2\,\%$ error for certain flight motion-modes.

Is self-similarity maintained when scaling from wind tunnel test conditions to flight?

Yes. The wind tunnel test conditions ($M = 0.03, Re = 9.00 \times 10^6$) are incompressible, and the separated boundary layer leaving the parachute skirt is fully-turbulent, with a fixed separation location at the skirt lip. As expected, comparative CFD studies (see Fig. 4.5) demonstrate that aerodynamic loads are insensitive to increases to the flight value of Reynolds number $Re = 2.36 \times 10^7$. Additionally, when the Mach number (M) is scaled by a factor of five to $M = 0.15$ to avoid solver low-M preconditioning, dynamic similarity of the loads coefficients is maintained as long as the freestream density (ρ_∞) is scaled so as to alter dynamic pressure ($\overline{q}$) by the same factor and the rate of any prescribed motion is also scaled by this factor.

Can the dynamic load trends of a parachute WTT be recovered in CFD simulation without modeling wind tunnel wall effects?

Yes, with some resulting error of approximation. The effect of modeling wind tunnel walls was shown to alter axial force coefficient (C_A) and C_N trends enough to be potentially significant, but that general dynamic stability trends are preserved. Accurate quantification of the total error increment due to wind tunnel wall effects was not possible in the current research due to the parachute geometry differences in the comparative studies, but the overall difference due to simulation in free-air should be less than the $79\,\%$ difference observed in Fig. 4.6.

Is URANS turbulence modeling sufficient for recovering the bulk unsteady nature of moving, bluff-body wakes?

Yes. Comparisons of URANS simulations to higher fidelity Detached Eddy Simulation (DES) simulations of the same swinging parachute (see Fig. 4.8) demonstrated that unsteady drag magnitude was predicted within $1.25\,\%$, which is acceptable for CFD parachute design accuracy. However, frequencies of the unsteady response and the strength of the stability trends showed incremental difference, which implies that DES turbulence modeling further improves the accuracy of the model.

Is the root cause of parachute dynamic instability the same shed ring vortex that causes static instability?

Yes. In the moving-mesh parachute CFD simulation developed for this work, the ring vortex is shed from the skirt as high-pressure air spills out of the cavity, as was also observed in the static CFD tests by Greathouse and Schwing. At small α, this vortex exhibits a two-dimensional oscillation across a single diameter of the skirt, inducing high-speed flow on alternating outboard sides of the parachute as the shear layer separates and before the vortex begins to roll up (see Fig. 3.17). The CFD pendulum model demonstrates that the regular frequency of this oscillation has a compounding, destabilizing effect on parachute motion, building the system's angular momentum until the parachute swing exceeds the unstable regions $(-5^\circ < \alpha < 5^\circ)$, at which point a pressure-based, damping moment created by the crosswise orientation of the parachute with respect to the flow tends to restore the centerline orientation. The combination of these opposing effects results in sustained pendulum motion of the parachute.

Does CFD of moving bodies prescribed to a known motion track resolve aerodynamic responses as accurately as aerodynamically-driven motion?

Yes, with accuracy proportional to the approximation of the target motion and only for previously-observed motion tracks. Comparisons of a circular cylinder prescribed to a motion trajectory derived from a least-squares regression, sinusoidal fit of the motion observed for the same cylinder simulated with aerodynamically-driven motion showed equivalently similar unsteady aerodynamic responses, with only slight differences in phase and magnitude (see Fig. 3.13a). This is an important result, as prescribed motion simulations are often more practical to implement and efficient to complete, making them a more feasible option for many engineering applications. However, the minor differences in the two comparison cases demonstrate that the accuracy of the prescribed simulation is dependent on the accuracy of the trajectory model, and complex and chaotic trajectories like a ballistic range test might be more accurately and efficiently modeled with Aero6DOF-predicted trajectories. In addition, the use of prescribed motion simulation for accurate dynamics modeling is restricted to known motion trajectories, limiting its utility to refining model uncertainties and to incrementing aerodynamic databases (both important applications). And for producing estimates of dynamic stability for new, untested geometries, as in Fig. 5.4b, the predictive nature of Aero6DOF-mode is a requirement.

Can the simple parachute-analog model be used as an accurate surrogate of true parachute aerodynamic response?

Yes, for initial design and notional trends purposes. The 2D, Aero6DOF-mode scoop showed first-order similarity to the prescribed Orion EDU parachute, with a $30\,\%$ difference in drag magnitude and $\frac{dC_{N,m}}{d\alpha_T}$ of the same sign and $2.5\times$ the magnitude (see Fig. 4.11). The differences in these values are explainable due to the significant differences in model geometry, flow dimensionality, and motion fidelity and are too large to justify the 2D scoop as a perfectly self-similar analog of the Orion EDU parachute but are sufficiently similar for determining notional trends pertaining to parachute dynamics and for performing comparative studies of features like geometric porosity. The 3D scoop model produced more similar stability trend results to the parachute than the 2D case, but its polar trim behavior is significantly dissimilar to the observed motion of the parachute, so the simulation of this specific geometry is not sufficient for emulating Orion EDU dynamics.

6.3 Future Work

In this research, baseline uncertainties for a moving-mesh CFD model of parachute pendulum motion were established to inform the creation of dynamic stability increments to aerodynamic databases. The magnitude of these uncertainties could be refined by higher-fidelity approximation of the conditions of the WTT comparison case. Inclusion of wind tunnel walls and DES turbulence modeling in the simulation of the Orion EDU parachute should provide unsteady aerodynamic loads that are more like those measured in the WTT, especially at higher α. Most significantly, an aerodynamically-driven, Aero6DOF-mode simulation of this parachute would eliminate errors due to approximations in the prescribed motion fit equation and provide a straightforward path to simulating multi-DoF, precessing trajectories like those observed for the WTT model. With improved uncertainty quantification, the next logical application of this model would be a follow-on to the parametric study of the effect of geometric porosity of the EDU parachute geometry on static stability by Greathouse and Schwing that would utilize Aero6DOF-mode to additionally uncover dynamic stability effects and further inform the design of similar parachute systems. It would also be of interest to model exotic parachute flight conditions, such as supersonic Mars EDL.

Additional validation of the model's ability to predict aerodynamically-driven motion could be obtained by performing an analogous wind tunnel test to the scoop parachute-analog. This would provide general truth data for a simple aerodynamic pendulum, which is sparsely available in the literature and would allow the assessment of unexpected CFD simulation results like the polar trim of the three-dimensional scoop geometry.

Beyond these applications, further improvements to the model could be obtained by increasing the complexity of the modeled systems and relaxing more of the simplifications required by rigid-body CFD. Introduction of FSI capabilities to allow “breathing” deformation of the canopy at the apex of its swing or axial translation of the canopy due to tether or tension might alleviate excessive loading that causes the rigid-body simulation to deviate from the WTT trends. Modeling of fabric porosity using a flow-through boundary condition would also improve results by allowing fine-tuning of the simulation drag without requiring changes to the geometric porosity.

Additional complexities of the parachute descent system could also be modeled, including ingestion of and interaction with the wake of the vehicle tethered upstream of the parachute, which could have adverse effects on parachute stability and contribute to the initiation of pendulum motion. Though it was established that the dynamic stability of a single parachute canopy is a root cause of parachute cluster instability, canopy-to-canopy proximity interactions of parachutes, both from combination of turbulent structures in the wake and from geometry deformations due to collision, could also result in potential secondary effects on dynamic stability and is an additional level of fidelity that could be modeled in the future with this technique.

Bibliography

[1] L. Da Vinci, "Codex atlanticus," Biblioteca Ambrosiana, Milan, vol. 26, p. 1, 1894. [Cited: 1 and 2]

[2] Q. Sima, Records of the grand historian: Han dynasty. Columbia University Press, 1993, vol. 65. [Cited: 1]

[3] A. A. Siddiqi, Challenge to Apollo: The Soviet Union and the Space Race, 1945-1974. National Aeronautics and Space Administration, NASA History Division, Office, 2000, vol. 4408. [Cited: 1]

[4] T. Knacke, "The Apollo parachute landing system," in AIAA Second Aerodynamic Decelerator Systems Conference, 1968. [Cited: 1, 3, and 74]

[5] J. Mckinney, P. Ferguson, M. L. Weber, A. Taylor, A. R. Diaz, and T. DePauw, "Boeing CST-100 Landing and Recovery System Design and Development Testing," in AIAA Aerodynamic Decelerator Systems (ADS) Conference, 2013, p. 1262. [Online]. Available: https://doi.org/10.2514/6.2013-1262 [Cited: 1]

[6] H. Gehman, S. Turcotte, J. Barry, K. W. Hess, J. N. Hallock, S. B. Wallace, D. Deal, S. Hubbard, R. E. Tetrault, S. E. Widnall, D. D. Osheroff, S. Ride, and J. Logsdon, "Report of columbia accident investigation board," 2003. [Cited: 1]

[7] J. Karcz, S. Davis, M. Aftosmis, G. Allen, N. Bakhtian, A. Dyakonov, K. Edquist, B. Glass, A. Gonzales, J. Heldmann et al., "Red dragon: Low-cost access to the surface of mars using commercial capabilities," in Concepts and Approaches for Mars Exploration, Houston, Texas, 2012. [Cited: 2]

[8] NASA, "Eft1 - the splashdown of orion," 2014. [Online]. Available: https://www.youtube.com/watch?v=XkXzZ4xwJKQ [Cited: 2]

[9] NASA, "Orion's Parachute System," factsheet brochure. [Cited: 2]

[10] Mission Evauation Team, "Apollo 15 Mission Main Parachute Failure Anomaly Report No. 1," National Aeronautics and Space Administration, Manned Spacecraft Center, Tech. Rep., 1971. [Cited: 3]

[11] S. Clark, "Boeing identifies cause of chute malfunction, preps for Starliner launch," Nov. 2019. [Cited: 3]

[12] R. Machin and E. Ray, "Pendulum Motion in Main Parachute Clusters," in 23rd AIAA Aerodynamic Decelerator Systems Technology Conference. Daytona Beach, FL: American Institute of Aeronautics and Astronautics, Apr. 2015, p. 2138. [Online]. Available: https://doi.org/10.2514/6.2015-2138 [Cited: 3, 6, 8, and 10]

[13] B. P. Anderson, J. Greathouse, J. Powell, J. C. Ross, B. Porter, P. W. Goulding, M. Zwicker, C. Mollmann, E. T. Schairer, and L. K. Kushner, "Sub-Scale Orion Parachute Test Results From the National Full-Scale Aerodynamics Complex 80- by 120-ft Wind Tunnel," in

24th AIAA Aerodynamic Decelerator Systems Technology Conference. Denver, Colorado: American Institute of Aeronautics and Astronautics, Jun. 2017, p. 4203. [Online]. Available: https://doi.org/10.2514/6.2017-4203 [Cited: 3, 6, 8, 9, 10, 72, 74, and 97]

[14] R. C. Maydew, C. W. Peterson, and K. J. Orlik-Rückemann, Design and Testing of High-Performance Parachutes, ser. AGARDograph. Neuilly-sur-Seine: AGARD, 1991, no. 319. [Cited: 3, 74, 98, and 104]

[15] Y. Ali, B. Sommer, B. P. Anderson, T. Truong, and C. Madsen, "Orion Multi-Purpose Crew Vehicle Solving and Mitigating the Two Main Parachute Pendulum Problem," in 24th AIAA Aerodynamic Decelerator Systems Technology Conference, 2017, p. 4056. [Online]. Available: https://doi.org/10.2514/6.2017-4056 [Cited: 3, 4, 9, 97, 101, and 106]

[16] S. Belknap and K. Goar, "Summary analysis report of drop tests performed during the apollo main parachute improvement," Tech. Rep. NVR-3722, 1964. [Cited: 4 and 9]

[17] D. Adams and T. Rivellini, "Mars Science Laboratory's Parachute Qualification Approach," in 20th AIAA Aerodynamic Decelerator Systems Technology Conference and Seminar. Seattle, Washington: American Institute of Aeronautics and Astronautics, May 2009. [Online]. Available: https://doi.org/10.2514/6.2009-2913 [Cited: 4 and 40]

[18] J. Greathouse and A. Schwing, "Study of Geometric Porosity on Static Stability and Drag using Computational Fluid Dynamics for Rigid Parachute Shapes," in 23rd AIAA Aerodynamic Decelerator Systems Technology Conference. Daytona Beach, FL: American Institute of Aeronautics and Astronautics, Apr. 2015, p. 2131. [Online]. Available: https://doi.org/10.2514/6.2015-2131 [Cited: 5, 7, 8, 9, 15, 35, 72, 76, 80, 81, 97, 106, 108, 115, and 117]

[19] G. L. Faurote, "Design of disk-gap-band and modified ringsail parachutes and development of ballute apex inlet for supersonic application," NASA Langley Research Center, Tech. Rep. GER-14657, 1970. [Cited: 6]

[20] V. Behr and J. Potvin, "Parachute Definitions, Nomenclature and Types," 2010. [Cited: 7]

[21] P. Delurgio, "Evolution of the Ringsail parachute," in 15th Aerodynamic Decelerator Systems Technology Conference. Toulouse,France: American Institute of Aeronautics and Astronautics, Jun. 1999. [Online]. Available: https://doi.org/10.2514/6.1999-1700 [Cited: 7 and 8]

[22] F. M. White and D. F. Wolf, "A theory of three-dimensional parachute dynamic stability," Journal of Aircraft, vol. 5, no. 1, pp. 86–92, Jan. 1968. [Online]. Available: https://doi.org/10.2514/3.43912 [Cited: 10]

[23] W. R. Graham and B. R. Moss, "Comment on "A Theory of Three-Dimensional Parachute Dynamic Stability"," Journal of Aircraft, vol. 54, no. 2, pp. 855–855, Mar. 2017. [Online]. Available: https://doi.org/10.2514/1.C033668 [Cited: 10]

[24] B. White, “Numerical solutions to the opening dynamics of a parachute,” in 10th Annual Meeting and Technical Display. Washington,DC,U.S.A.: American Institute of Aeronautics and Astronautics, Jan. 1974, p. 267. [Online]. Available: https://doi.org/10.2514/6.1974-267 [Cited: 10]

[25] J. M. Ginn, I. G. Clark, and R. D. Braun, “Parachute Dynamic Stability and the Effects of Apparent Inertia,” in AIAA Atmospheric Flight Mechanics Conference. Atlanta, GA: American Institute of Aeronautics and Astronautics, Jun. 2014, p. 2390. [Online]. Available: https://doi.org/10.2514/6.2014-2390 [Cited: 10]

[26] J. Pei, “Nonlinear Analysis of a Two-Parachute System Undergoing Pendulum Motion,” in AIAA Aviation 2019 Forum. Dallas, Texas: American Institute of Aeronautics and Astronautics, Jun. 2019. [Online]. Available: https://doi.org/10.2514/6.2019-3379 [Cited: 10 and 97]

[27] K. R. Stein, R. J. Benney, and E. C. Steeves, “A computational model that couples aerodynamic and structural dynamic behavior of parachutes during the opening process,” Army Natick Research Development and Engineering Center, MA, Tech. Rep., 1993. [Cited: 11 and 12]

[28] C. W. Peterson, J. Strickland, and H. Higuchi, “The Fluid Dynamics of Parachute Inflation,” Annual Review of Fluid Mechanics, vol. 28, no. 1, p. 27, 1996. [Online]. Available: https://doi.org/10.1146/annurev.fl.28.010196.002045 [Cited: 11]

[29] M. Pruett, M. Accorsi, and R. Charles, “Validation of Computational Structural Dynamics Models for Parachute Systems,” in 20th AIAA Aerodynamic Decelerator Systems Technology Conference and Seminar. Seattle, Washington: American Institute of Aeronautics and Astronautics, May 2009. [Online]. Available: https://doi.org/10.2514/6.2009-2934 [Cited: 11]

[30] Y. Fan and J. Xia, “Simulation of 3D parachute fluid–structure interaction based on nonlinear finite element method and preconditioning finite volume method,” Chinese Journal of Aeronautics, vol. 27, no. 6, pp. 1373–1383, Dec. 2014. [Online]. Available: https://doi.org/10.1016/j.cja.2014.10.003 [Cited: 11 and 12]

[31] Q. Shi, D. Reasor, Z. Gao, X. Li, and R. D. Charles, “On the verification and validation of a spring fabric for modeling parachute inflation,” Journal of Fluids and Structures, vol. 58, pp. 20–39, Oct. 2015. [Online]. Available: https://doi.org/10.1016/j.jfluidstructs.2015.06.014 [Cited: 12 and 13]

[32] J.-D. Kim, “Modeling of Parachute Dynamics with Front Tracking Method,” PhD Thesis, The Graduate School, Stony Brook University: Stony Brook, NY., 2012. [Cited: 12]

[33] Z. Gao, R. D. Charles, and X. Li, “Numerical Modeling of Flow Through Porous Fabric Surface in Parachute Simulation,” AIAA Journal, vol. 55, no. 2, pp. 686–690, Feb. 2017. [Online]. Available: https://doi.org/10.2514/1.J054997 [Cited: 12 and 14]

[34] K. Takizawa, C. Moorman, S. Wright, T. Spielman, and T. E. Tezduyar, “Fluid-structure interaction modeling and performance analysis of the Orion spacecraft parachutes,”

International Journal for Numerical Methods in Fluids, vol. 65, no. 1-3, pp. 271–285, Jan. 2011. [Online]. Available: https://doi.org/10.1002/fld.2348 [Cited: 12 and 13]

[35] V. Kalro and T. E. Tezduyar, "A parallel 3D computational method for fluid-structure interactions in parachute systems," Comput. Methods Appl. Mech. Engrg., p. 12, 2000. [Cited: 12]

[36] K. Karagiozis, R. Kamakoti, F. Cirak, and C. Pantano, "A computational study of supersonic disk-gap-band parachutes using Large-Eddy Simulation coupled to a structural membrane," Journal of Fluids and Structures, vol. 27, no. 2, pp. 175–192, Feb. 2011. [Online]. Available: https://doi.org/10.1016/j.jfluidstructs.2010.11.007 [Cited: 12 and 13]

[37] J. Boustani, M. F. Barad, C. C. Kiris, and C. Brehm, "Fully-Coupled Fluid-Structure Interaction Simulations of a Supersonic Parachute," in AIAA Aviation 2019 Forum. Dallas, Texas: American Institute of Aeronautics and Astronautics, Jun. 2019. [Online]. Available: https://doi.org/10.2514/6.2019-3279 [Cited: 12 and 13]

[38] D. Z. Huang, P. Avery, C. Farhat, J. Rabinovitch, A. Derkevorkian, and L. D. Peterson, "Modeling, Simulation and Validation of Supersonic Parachute Inflation Dynamics during Mars Landing," in AIAA Scitech 2020 Forum. Orlando, FL: American Institute of Aeronautics and Astronautics, Jan. 2020. [Online]. Available: https://doi.org/10.2514/6.2020-0313 [Cited: 13]

[39] M. McQuilling, L. Lobosky, and S. Sander, "Computational Investigation of the Flow Around a Parachute Model," Journal of Aircraft, vol. 48, no. 1, pp. 34–41, Jan. 2011. [Online]. Available: https://doi.org/10.2514/1.46255 [Cited: 14 and 15]

[40] D. J. Dinzl, V. M. Gidzak, and G. V. Candler, "Simulation of Drogue Parachute for the Multi-Purpose Crew Vehicle using Computational Fluid Dynamics," in AIAA Aerodynamic Decelerator Systems (ADS) Conference. Daytona Beach, Florida: American Institute of Aeronautics and Astronautics, Mar. 2013. [Online]. Available: https://doi.org/10.2514/6.2013-1322 [Cited: 14]

[41] K. Kitamura, K. Fukumoto, and K. Mori, "Numerical Study of Surface Pressure Fluctuation on Rigid Disk-Gap-Band-Type Supersonic Parachutes," AIAA Journal, vol. 58, no. 12, pp. 5347–5360, Dec. 2020. [Online]. Available: https://doi.org/10.2514/1.J059190 [Cited: 14 and 15]

[42] K. Bergeron, M. Ghoreyshi, G. Noetscher, A. Jirasek, and T. Rose, "Computational Study and Modeling of Single and Clustered Parachutes in the Wake of an Aircraft," in AIAA AVIATION 2021 FORUM. VIRTUAL EVENT: American Institute of Aeronautics and Astronautics, Aug. 2021. [Online]. Available: https://doi.org/10.2514/6.2021-2541 [Cited: 14 and 16]

[43] G. Noetscher, M. Ghoreyshi, T. M. Rose, A. Jirasek, and K. Bergeron, "Optimization of Extraction Line Distance for Ringslot Parachute Extraction of Heavy Cargo from C-17," in AIAA Scitech 2021 Forum. VIRTUAL EVENT: American Institute of Aeronautics and Astronautics, Jan. 2021. [Online]. Available: https://doi.org/10.2514/6.2021-0350 [Cited: 14]

[44] K. Bergeron, M. Ghoreyshi, E. Larsen, A. Jirasek, T. M. Rose, and G. Noetscher, "Near-Body/Cartesian Off-Body Simulations for C-17 and Extraction Parachute," in AIAA AVIATION 2020 FORUM. VIRTUAL EVENT: American Institute of Aeronautics and Astronautics, Jun. 2020. [Online]. Available: https://doi.org/10.2514/6.2020-2712 [Cited: 14]

[45] M. Serrano, E. Leigh, W. Johnson, J. Forsythe, and S. Morton, "Computational Aerodynamics of the C-130 in Airdrop Configurations," in 41st Aerospace Sciences Meeting and Exhibit. Reno, Nevada: American Institute of Aeronautics and Astronautics, Jan. 2003. [Online]. Available: https://doi.org/10.2514/6.2003-229 [Cited: 14]

[46] S. Murman, W. Chan, M. Aftosmis, and R. Meakin, "An Interface for Specifying Rigid-Body Motions for CFD Applications," in 41st Aerospace Sciences Meeting and Exhibit. Reno, Nevada: American Institute of Aeronautics and Astronautics, Jan. 2003, p. 1237. [Online]. Available: https://doi.org/10.2514/6.2003-1237 [Cited: 15 and 27]

[47] R. Meakin, "Computations of the unsteady flow about a generic wing/pylon/finned-store configuration," in Astrodynamics Conference. Hilton Head Island,SC,U.S.A.: American Institute of Aeronautics and Astronautics, Aug. 1992. [Online]. Available: https://doi.org/10.2514/6.1992-4568 [Cited: 15]

[48] L. Huyse, C. Waldhart, D. Riha, B. Thacker, C. Larsen, R. Gomez, and P. Stuart, "Probabilistic Modeling of Space Shuttle Debris Impact," in 48th AIAA/ASME/ASCE/AHS/ASC Structures, Strtral. Dynmcs., and Mtrls. Conference. Honolulu, Hawaii: American Institute of Aeronautics and Astronautics, Apr. 2007. [Online]. Available: https://doi.org/10.2514/6.2007-1954 [Cited: 15]

[49] N. Arai, T. Nakamura, and S. Takahashi, "Three-dimensional motion analysis of a free descent parachute-like body," in 21st AIAA Aerodynamic Decelerator Systems Technology Conference and Seminar. Dublin, Ireland: American Institute of Aeronautics and Astronautics, May 2011, p. 2588. [Online]. Available: https://doi.org/10.2514/6.2011-2588 [Cited: 15 and 16]

[50] N. Arai and K. O-yabu, "Unsteady Flow Field Around a Freely Oscillating Concave Body in Supersonic Flow," in 17th AIAA Aerodynamic Decelerator Systems Technology Conference and Seminar. Monterey, California: American Institute of Aeronautics and Astronautics, May 2003. [Online]. Available: https://doi.org/10.2514/6.2003-2148 [Cited: 16]

[51] J. D. Vasile, "Computational Investigation on the Wake Flow of a Hemispherical Parachute Canopy," in 24th AIAA Aerodynamic Decelerator Systems Technology Conference. Denver, Colorado: American Institute of Aeronautics and Astronautics, Jun. 2017, p. 3542. [Online]. Available: https://doi.org/10.2514/6.2017-3542 [Cited: 16]

[52] G. P. Guruswamy, "Time-Accurate Coupling of Three-Degree-of-Freedom Parachute System with Navier–Stokes Equations," Journal of Spacecraft and Rockets, vol. 54, no. 6, pp. 1278–1283, Nov. 2017. [Online]. Available: https://doi.org/10.2514/1.A33835 [Cited: 16]

[53] I. Rodriguez, R. Borell, O. Lehmkuhl, C. D. Perez Segarra, and A. Oliva, "Direct numerical simulation of the flow over a sphere at Re = 3700," Journal of Fluid Mechanics, vol. 679, pp. 263–287, Jul. 2011. [Online]. Available: https://doi.org/10.1017/jfm.2011.136 [Cited: 18]

[54] C. E. Smith, N. Beratlis, E. Balaras, K. Squires, and M. Tsunoda, "Numerical investigation of the flow over a golf ball in the subcritical and supercritical regimes," International Journal of Heat and Fluid Flow, vol. 31, no. 3, pp. 262–273, 2010. [Online]. Available: https://doi.org/10.1016/j.ijheatfluidflow.2010.01.002 [Cited: 18]

[55] P. Catalano, M. Wang, G. Iaccarino, and P. Moin, "Numerical simulation of the flow around a circular cylinder at high Reynolds numbers," International Journal of Heat and Fluid Flow, vol. 24, no. 4, pp. 463–469, Aug. 2003. [Online]. Available: https://doi.org/10.1016/S0142-727X(03)00061-4 [Cited: 18, 19, 48, and 49]

[56] P. R. Spalart, "Detached-Eddy Simulation," Annual Review of Fluid Mechanics, vol. 41, no. 1, pp. 181–202, 2009. [Online]. Available: https://doi.org/10.1146/annurev.fluid.010908.165130 [Cited: 19]

[57] K. D. Squires, "Detached-Eddy Simulation: Current Status and Perspectives," in Direct and Large-Eddy Simulation V, R. Friedrich, B. J. Geurts, and O. Métais, Eds. Dordrecht: Springer Netherlands, 2004, pp. 465–480. [Cited: 19]

[58] C. Mockett, B. Greschner, T. Knacke, R. Perrin, J. Yan, and F. Thiele, "Demonstration of Improved DES Methods for Generic and Industrial Applications," in Advances in Hybrid RANS-LES Modelling, S.-H. Peng and W. Haase, Eds. Berlin, Heidelberg: Springer Berlin Heidelberg, 2008, pp. 222–231. [Cited: 19]

[59] A. M. Schwing and G. V. Candler, "Detached-Eddy Simulation of Capsule Wake Flows and Comparison to Wind-Tunnel Test Data," Journal of Spacecraft and Rockets, vol. 52, no. 2, pp. 439–449, Mar. 2015. [Online]. Available: https://doi.org/doi:10.2514/1.A32834 [Cited: 19]

[60] J. R. Forsythe, K. D. Squires, K. E. Wurtzler, and P. R. Spalart, "Detached-Eddy Simulation of the F-15E at High Alpha," Journal of Aircraft, vol. 41, no. 9, pp. 193–200, 2004. [Online]. Available: https://doi.org/10.2514/1.2111 [Cited: 19]

[61] A. Travin, M. Shur, M. Strelets, and P. Spalart, "Detached-Eddy Simulations Past a Circular Cylinder," Flow, Turbulence and Combustion, vol. 63, no. 1, pp. 293–313, Jan. 2000. [Online]. Available: https://doi.org/10.1023/A:1009901401183 [Cited: 19 and 87]

[62] F. Menter and Y. Egorov, "A Scale Adaptive Simulation Model using Two-Equation Models," in 43rd AIAA Aerospace Sciences Meeting and Exhibit, Aerospace Sciences Meetings, Reno, NV, Jan. 2005. [Online]. Available: https://doi.org/10.2514/6.2005-1095 [Cited: 19 and 87]

[63] A. Roshko, "Experiments on the flow past a circular cylinder at very high reynolds number," vol. 10, no. 3, pp. 345–356, 1961. [Online]. Available: https://doi.org/10.1017/S0022112061000950 [Cited: 25, 36, 47, 48, and 54]

[64] P. G. Buning, D. C. Jespersen, T. H. Pulliam, W. Chan, J. P. Slotnick, S. Krist, and K. J. Renze, “Overflow user’s manual,” NASA Langley Research Center, Hampton, VA, 2002. [Cited: 27 and 38]

[65] R. Nichols, R. Tramel, and P. Buning, “Solver and turbulence model upgrades to OVERFLOW 2 for unsteady and high-speed applications,” in 24th AIAA Applied Aerodynamics Conference, 2006, p. 2824. [Online]. Available: https://doi.org/10.2514/6.2006-2824 [Cited: 27 and 38]

[66] R. H. Nichols and P. G. Buning, “User’s Manual for OVERFLOW 2.1,” University of Alabama and NASA Langley Research Center, 2008. [Cited: 27 and 38]

[67] P. Buning, “OVERFLOW 2.3a release notes,” 2019. [Cited: 29]

[68] L. D. Halstrom and S. Robinson, “Investigation of Off-Body Motion Constraints in OVERFLOW Moving Mesh CFD Simulations of an Aerodynamic Pendulum,” in AIAA AVIATION 2021 FORUM. VIRTUAL EVENT: American Institute of Aeronautics and Astronautics, Aug. 2021. [Online]. Available: https://doi.org/10.2514/6.2021-2504 [Cited: 35]

[69] S. Rogers, K. Roth, S. Nash, M. Baker, J. Slotnick, M. Whitlock, and H. Cao, “Advances in overset CFD processes applied to subsonic high-lift aircraft,” in 18th Applied Aerodynamics Conference. Denver,CO,U.S.A.: American Institute of Aeronautics and Astronautics, Aug. 2000, p. 4216. [Online]. Available: https://doi.org/10.2514/6.2000-4216 [Cited: 38]

[70] W. Chan, “The overgrid interface for computational simulations on overset grids,” in 32nd AIAA Fluid Dynamics Conference and Exhibit, 2002, p. 3188. [Online]. Available: https://doi.org/10.2514/6.2002-3188 [Cited: 38]

[71] ——, “Developments in Strategies and Software Tools for Overset Structured Grid Generation and Connectivity,” in 20th AIAA Computational Fluid Dynamics Conference, 2011, p. 3051. [Online]. Available: https://doi.org/10.2514/6.2011-3051 [Cited: 38]

[72] R. Meakin, “Object X-rays for cutting holes in composite overset structured grids,” in 15th AIAA Computational Fluid Dynamics Conference, 2001, p. 2537. [Online]. Available: https://doi.org/10.2514/6.2001-2537 [Cited: 38]

[73] N. Kim and W. Chan, “Automation of Hole-Cutting for Overset Grids Using the X-rays Approach,” in 20th AIAA Computational Fluid Dynamics Conference. Honolulu, Hawaii: American Institute of Aeronautics and Astronautics, Jun. 2011. [Online]. Available: https://doi.org/10.2514/6.2011-3052 [Cited: 38]

[74] W. M. Chan, N. Kim, and S. A. Pandya, “Advances in domain connectivity for overset grids using the x-rays approach,” 2012. [Cited: 38]

[75] P. Buning, “OVERFLOW 2.2m release notes,” 2017. [Cited: 39]

[76] N. Suhs, S. Rogers, and W. Dietz, "Pegasus 5: An automated pre-processor for overset-grid cfd," in 32nd AIAA Fluid Dynamics Conference and Exhibit, 2002, p. 3186. [Online]. Available: https://doi.org/10.2514/6.2002-3186 [Cited: 39]

[77] S. Pandya, S. Venkateswaran, and T. Pulliam, "Implementation of Preconditioned Dual-Time Procedures in OVERFLOW," in 41st Aerospace Sciences Meeting and Exhibit. Reno, Nevada: American Institute of Aeronautics and Astronautics, Jan. 2003, p. 72. [Online]. Available: https://doi.org/10.2514/6.2003-72 [Cited: 45]

[78] R. Nichols, R. Tramel, and P. Buning, "Evaluation of Two High Order WENO Schemes," in 25th AIAA Applied Aerodynamics Conference. Miami, Florida: American Institute of Aeronautics and Astronautics, Jun. 2007. [Online]. Available: https://doi.org/10.2514/6.2007-3920 [Cited: 45]

[79] P. Spalart and S. Allmaras, "A one-equation turbulence model for aerodynamic flows," in 30th Aerospace Sciences Meeting and Exhibit. Reno,NV,U.S.A.: American Institute of Aeronautics and Astronautics, Jan. 1992. [Online]. Available: https://doi.org/10.2514/6.1992-439 [Cited: 46]

[80] F. R. Menter, "Two-equation eddy-viscosity turbulence models for engineering applications," AIAA journal, vol. 32, no. 8, pp. 1598–1605, 1994. [Online]. Available: https://doi.org/10.2514/3.12149 [Cited: 46 and 77]

[81] E. Achenbach, "Distribution of local pressure and skin friction around a circular cylinder in cross-flow up to $re = 5 \times 10^6$," Journal of fluid Mechanics, vol. 34, no. 4, pp. 625–639, 1968. [Online]. Available: https://doi.org/10.1017/S0022112068002120 [Cited: 47 and 48]

[82] K. Gonyea, R. Braun, C. L. Tanner, I. G. Clark, L. K. Kushner, and E. Schairer, "Aerodynamic Stability and Performance of Next-Generation Parachutes for Mars Entry, Descent, and Landing," in AIAA Aerodynamic Decelerator Systems (ADS) Conference. Daytona Beach, Florida: American Institute of Aeronautics and Astronautics, Mar. 2013, p. 1356. [Online]. Available: https://doi.org/10.2514/6.2013-1356 [Cited: 74]

[83] E. Ray, "Test Vehicle Forebody Wake Effects on CPAS Parachutes," in 24th AIAA Aerodynamic Decelerator Systems Technology Conference. Denver, Colorado: American Institute of Aeronautics and Astronautics, Jun. 2017, p. 3227. [Online]. Available: https://doi.org/10.2514/6.2017-3227 [Cited: 74 and 110]

[84] E. T. Schairer, L. K. Kushner, J. T. Heineck, and E. Solis, "Measurements of Parachute Dynamics in the World's Largest Wind Tunnel by Stereo Photogrammetry," in 2018 Aerodynamic Measurement Technology and Ground Testing Conference. Atlanta, Georgia: American Institute of Aeronautics and Astronautics, Jun. 2018. [Online]. Available: https://doi.org/10.2514/6.2018-3802 [Cited: 75]

[85] J. M. Macha and R. J. Buffington, "Wall-interference corrections for parachutes in a closed wind tunnel," Journal of Aircraft, vol. 27, no. 4, pp. 320–325, 1990. [Online]. Available: https://doi.org/10.2514/3.25275 [Cited: 75 and 86]

[86] R. M. Beam and R. F. Warming, “An implicit finite-difference algorithm for hyperbolic systems in conservation-law form,” Journal of Computational Physics, vol. 22, no. 1, pp. 87–110, 1976. [Online]. Available: https://doi.org/10.1016/0021-9991(76)90110-8 [Cited: 77]

[87] W. D. Sundberg, “New solution method for steady-state canopy structural loads,” Journal of Aircraft, vol. 25, no. 11, pp. 1045–1051, Nov. 1988. [Online]. Available: https://doi.org/10.2514/3.45701 [Cited: 80]

[88] E. W. M. Roosenboom, A. Schröder, J. Agocs, and R. Geisler, “Coherent Wake Structures for Transport Aircraft at Cargo Airdrop Configurations Including Parachutes,” in 31st AIAA Applied Aerodynamics Conference. San Diego, CA: American Institute of Aeronautics and Astronautics, Jun. 2013. [Online]. Available: https://doi.org/10.2514/6.2013-2536 [Cited: 110]

Appendices

Appendix A

Nomenclature

Nomenclature

$()'$	**perturbation quantity**
C_A	**axial force coefficient**
C_N	**normal force coefficient**
C_P	**pressure coefficient**
C_d	**drag coefficient**
$C_{N,m}$	**missile-frame normal force coefficient**
C_{dyn}	**coefficient increment due to dynamic effects**
$C_{m,m}$	**missile-frame pitching moment coefficient**
C_m	**pitching moment coefficient**
F_A	**axial force**
F_N	**normal force**
I	**moment of inertia**
M	**Mach number**
M_m	**pitching moment**
P	**pressure**
Re	**Reynolds number**
St	**Strouhal number**
V_∞	**freestream velocity**
V_N	**tangential swing velocity**
V_{eff}	**effective velocity**
Δs_w	**wall spacing**
$\Sigma C_{M,Y_i}$	**total pendulum moment coefficient**
$\Sigma C_{M,Z}$	**total azimuthal pendulum moment coefficient**
ΣM_{Y_i}	**total pendulum moment**
α	**angle of attack**
α_T	**total angle of attack**
α_{eff}	**effective angle of attack**
β	**side-slip angle**
$\ddot{\theta}$	**angular acceleration**
$\dot{\alpha}$	**rate of angle of attack**
$\dot{\theta}$	**angular velocity**
μ	**dynamic viscosity**
μ_w	**wall viscosity**
$\overline{()}$	**mean quantity (time-averaged)**
$\overline{q}$	**dynamic pressure**
ϕ	**roll angle**

ϕ_c	**aerodynamic clocking angle**
ϕ_s	**azimuthal angle**
ψ	**yaw angle**
ρ	**density**
ρ_∞	**freestream density**
ρ_w	**wall density**
τ_w	**wall shear stress**
θ	**pitch/swing angle**
θ_s	**polar angle**
θ_0	**initial swing angle**
θ_{max}	**maximum swing angle**
$\boldsymbol{F}_{aero}$	**net aerodynamic force**
$\boldsymbol{V}$	**velocity**
∇	**gradient function**
$\boldsymbol{g}$	**gravitational constant**
$\boldsymbol{u}$	**Einstein notation velocity**
$\boldsymbol{x}$	**Einstein notation dimension**
m	**mass**
t	**time**
u_τ	**friction velocity**
$\|_P$	**parachute reference frame**

Acronyms

AMR	**Adaptive Mesh Refinement 89**
CALA	**Canopy Loads Analysis 80**
CFD	**Computational Fluid Dynamics x, xi, 4, 10, 11, 13, 21, 57, 72, 109**
CGT	**Chimera Grid Tools 38, 81**
COM	**Center of Mass 28, 29, 31**
CPAS	**Capsule Parachute Assembly System v, xii, 3, 6, 8**
DCF	**Domain Connectivity Function vii, 38, 39, 44, 82, 83**
DES	**Detached Eddy Simulation vii, 14, 16, 19, 27, 77, 87–89, 96, 115, 117**
DGB	**Disk-Gap-Band vii, 12, 14, 40, 75–79, 82, 83, 85–89, 92, 104–106**
DNS	**Direct Numerical Simulation 17, 18**
EDL	**Entry, Descent, and Landing 1, 2, 4, 5, 12–14, 104, 109, 117**
EDU	**Engineering Design Unit v, vii, viii, 6, 7, 9, 10, 17, 74–80, 86, 87, 89–95, 97, 101, 108, 112, 114, 116, 117**
FBC	**Forward Bay Cover 5**
FBCP	**Forward Bay Cover Parachute 5**
FFT	**fast Fourier transform vi, 53, 54, 58, 59, 62, 63, 78, 79**
FSI	**Fluid-structure Interaction v, x, 8, 11–14, 16, 17, 22, 96, 109, 117**
GMP	**Geometry Manipulation Protocol x, 27, 29, 33, 34, 53, 58, 59, 70, 79, 92, 95, 110**
HRVIP	**Human/Vehicle/Robotic Integration and Performance vi, xii, 50, 51**
IBM	**Immersed Boundary Method 13**
IMU	**Inertial Measurement Unit 8**
LES	**Large Eddy Simulation 12, 13, 18, 19**

MPCV	**Multi-Purpose Crew Vehicle ii, x, 1, 2, 5, 6, 8–10, 12–15, 17, 22, 72, 74–76, 107, 112**
NASA	**National Aeronautics and Space Administration 2, 8**
NFAC	**National Full-scale Aerodynamics Complex vii, xii, 6, 9, 10, 75, 76, 79, 85, 89–91, 112**
ODE	**Ordinary Differential Equation vi, 23, 24, 26, 33, 57, 58, 110, 111**
PSD	**Power Spectral Density 53, 54, 58, 62, 63**
PTV	**Parachute Test Vehicle 3, 10**
RANS	**Reynolds-averaged Navier-Stokes x, 9, 14, 17–19, 22, 47, 77**
SA	**Spalart-Allmaras 46, 47**
SGS	**Subgrid-Scale model 18, 19**
SST	**Shear Stress Transport 27, 46, 48, 77**
URANS	**Unsteady Reynolds-averaged Navier-Stokes v, vii, 18, 19, 21, 27, 35, 46, 48, 49, 69, 73, 84, 85, 87–90, 92, 95, 112, 113, 115**
WTT	**wind tunnel test vii, ix, 4, 6, 8–10, 15, 20–22, 58, 72–79, 84, 90–92, 94, 95, 99, 102, 111–115, 117, 118**
XML	**Extensible Markup Language 27**